Sea-state interaction based dynamic model of the Liquid Robotics' Wave Glider

Modelling and control of a hybrid multi-body vessel

Gevashkar Rampersadh

Department of Electrical Engineering
University of Cape Town
Rondebosch, Cape Town
South Africa

Supervisor:
Robyn Verrinder

Co-supervisor:
Prof. E. Boje

June 2018

MSc. thesis submitted in fulfilment of the requirements for the degree of Masters in Electrical Engineering in the Department of Electrical Engineering at the University of Cape Town

Keywords: Multi-body modelling; Dynamic modelling; Sea state control

"*In the beginning the Universe was created. This has made a lot of people very angry and been widely regarded as a bad move.*" - Douglas Adams

This dissertation is formatted to be read in colour and in PDF format. When read in PDF format and utilizing hyperlinks, it is suggested that the embedded function in some PDF reader which allows for the reader to return to the section of text where a hyperlink originates be used.

Declaration

I, Gevashkar Rampersadh, hereby:

1. grant the University of Cape Town free licence to reproduce the above thesis in whole or in part, for the purpose of research;
2. declare that:
   (a) this thesis is my own unaided work, both in concept and execution, and apart from the normal guidance from my supervisor, I have received no assistance except as stated below:
   (b) neither the substance nor any part of the above thesis has been submitted in the past, or is being, or is to be submitted for a degree at this University or at any other university, except as stated below.

Signed by candidate

Gevashkar Rampersadh

Department of Electrical Engineering
University of Cape Town

Saturday 16th June, 2018

Abstract

Sea-state interaction based dynamic model of the Liquid Robotics' Wave Glider

Gevashkar Rampersadh

Saturday 16th June, 2018

A new class of unmanned marine research vessels makes use of wave propulsion to minimise energy requirements during voyages. Existing models of these hybrid sea-surface and underwater craft have not considered if the platform's interaction with the immediate surrounding sea could be incorporated to allow for more accurate navigation and path planning.

To this end a detailed three-dimensional model of one such vessel, the Liquid Robotics' Wave Glider, has been developed in this study. The multi-body system is described using Denavit-Hartenberg parametrisation and a Lagrangian approach is used to generate the equations of motion for the body. Physical dimensions are derived from platform measurements and from the product specification sheet, hydrodynamic factors are derived from a SolidWorks model of the system, and added mass components are determined from empirical data. Finally, the dynamic model is verified for a given sea state and multiple sea states are tested to investigate the effect on the model's performance. The developed Wave Glider model is shown to have a realistic response when hydrodynamic factors, added mass and hydrodynamic damping forces, are included and to sea states in terms of the hydrostatic restorative response. The wave-driven propulsion provided by the hydrofoils is shown to have dependence on the sea state by running the model in an open-loop simulation.

Following the model validation, a control system is developed for the Wave Glider model to allow yaw attitude control of the glider using the controllable glider rudder input. The control system is generated making use of quantitative feedback theory (QFT) methods to provide robust control for the under-actuated system. The control scheme is shown to provide suitable performance for sea states that result in variable glider velocities.

The model's performance, in terms of the average velocity, is shown to have dependence on the direction of the sea state by running the model in an open-loop simulation for multiple sea states with sinusoidal waves approaching the Wave Glider model from different directions.

Acknowledgements

I would like to thank my parents, sister, and family. Your unconditional love and unerring confidence in me lead me to perform beyond my own expectations. You have put me in the privileged position to be able to complete this degree; for that I am truly appreciative.

I would like to thank my supervisor, Ms. Robyn Verrinder, for countless hours of consultation and boundless advice.

My co-supervisor, Prof. Boje, for always finding a path for me to follow when presented with a problem.

My girlfriend, Claire Lawrence, for putting up with me when I encountered problems and reminding me to celebrate when I overcame those problems. Your editing definitely made this dissertation slightly more readable.

My office companions kept me sane in hours when I could easily have lost my mind, and provided much needed motivation and distractions.

Max Finbow, who was employed to assist with generating the hydrodynamic factors of the Wave Glider, for being knowledgeable and, more so, willing to pass on his knowledge.

The financial assistance of the National Research Foundation (NRF) towards this research is hereby acknowledged. Opinions expressed and conclusions arrived at, are those of the author and are not necessarily to be attributed to the NRF.

This work has been supported by a Joint South African Department of Science and Technology (DST) and Council for Scientific and Industrial Research (CSIR) Robotics Strategy of South Africa (ROSSA) Grant.

Contents

List of Figures

List of Tables

List of Commonly Used Symbols and Acronyms

ϕ_f	Roll of float
ϕ_g	Roll of glider
ϕ_t	Roll of tether
ψ_f	Yaw of float
ψ_g	Yaw of glider
ψ_r	Yaw of rudder
ρ	Density
$\mathbf{R}_b^n$	The rotation from the body-frame, denoted by the subscript, $\{b\}$, into the inertial frame, denoted by the superscript, $\{n\}$
θ_a	Pitch of hydrofoil
θ_f	Pitch of float
θ_g	Pitch of glider
θ_t	Pitch of tether
C_A	Coriolis and centripetal force matrix for added mass
C_{RB}	Rigid-body Coriolis and centripetal force matrix
D_s	Skin damping
D_v	Damping due to vortex shedding
G	Restorative force vector
L	Lagrangian
M_A	Mass matrix for added mass
M_{RB}	Rigid-body mass matrix
Q	Generalised force with components in direction of generalised coordinates
q	Generalised coordinates

$Q_b(q)$	Generalised force vector for buoyancy forces, dependent on the generalised coordinates
$Q_d(q, \dot{q})$	Generalised force vector for the hydrodynamic forces, damping and lift, dependent on the generalised coordinates and rate of change of generalised coordinates
$Q_r(q, \dot{q})$	Generalised force vector for rudder forces, dependent on the generalised coordinates and the rate of change of the generalised coordinates
R^2	Coefficient of determination. Representation of the goodness of fit which characterises what proportion of the variance of a dependent variable can be predicted by an independent variable.
r_g	Vector denoting position of CG relative to CO in body-frame
T	Kinetic energy
V	Potential energy
$v^b_{b/n}$	Linear velocity of the body frame, $\{b\}$, relative to the inertial frame, $\{n\}$, defined in the subscript, expressed in the body frame, defined in the superscript, where the inertial frame is assumed if not stated.
x_f	Position of float along inertial x-axis
y_f	Position of float along inertial y-axis
z_f	Position of float along inertial z-axis
CFD	Computational fluid dynamics
CG	Centre of mass
CO	Origin of frame
DH	Denavit-Hartenberg
DOF	Degree of freedom
NED	North-East-Down
PDE	Partial differential equation
QFT	quantitative feedback theory
ROV	Remotely operated underwater vehicles
SNAME	The Society of Naval Architects and Marine Engineers
USV	Unmanned surface vehicle
UUV	Unmanned underwater vehicle

Chapter 1

Introduction

As understanding the ocean will always be of critical importance, research in this environment is conducted using sensor buoys, satellite imaging and altimetry, and deployment of large research vessels such as the S.A. Agulhas II. However, these conventional research avenues can be expensive. Lower cost unmanned underwater (UUV) and unmanned surface vehicles (USV) have been used to complement or provide alternatives to some of these existing approaches. However, power restrictions have deleterious effects on the endurance of these vessels. The Wave Glider (Liquid Robotics Inc.), a hybrid USV and UUV [1–3], makes use of a novel wave propulsion mechanism to limit onboard power consumption and greatly extend mission endurance. The wave propulsion system makes the Wave Glider an excellent marine research platform and the vehicle has already seen wide application, including: climate studies, oceanographic surveys, and fishery management [4–6]. Wave Glider platforms must operate and function over extended periods of time in highly dynamic marine environments that are affected by strong currents, winds and a range of sea states.

1.1 Subject of investigation

The Wave Glider is a hybrid unmanned surface and underwater vessel used for marine research. The platform, shown in Fig. 1.1, is composed of three main components, namely: a surface float that acts as a storage vessel for the core electronics modules (instrumentation payload, solar panels, batteries) and as a buoyant vessel to harness wave energy; a submersible glider with six hinged hydrofoil fins which pivot near the leading edge; and an umbilical tether that physically couples the float and the underwater glider submersible and allows for electrical power transmission for actuation of the glider rudder and thruster. The steering of the system is based upon a rudder on the glider, and an electric propeller allows for deterministic propulsion.

The Wave Glider converts wave energy into forward thrust by utilizing the relative positioning of the float and glider in a high and low wave energy zone, respectively. As a wave crest passes under the float, the highly buoyant structure moves upwards, transferring force through the tether and creating vertical relative motion between the glider and the water. The hydrofoil fins on the glider are attached to springs such that rotation of the fins is resisted. As the vertical motion of the glider deflects the fins (up or down), an equilibrium angle of attack is reached whereby the spring force is balanced by the force of the water deflecting the hydrofoil or the maximum angle is reached and the hydrofoil is stopped by mechanical stops. The relative motion of the glider and the water, and angle of the hydrofoil, generates a hydrodynamic force

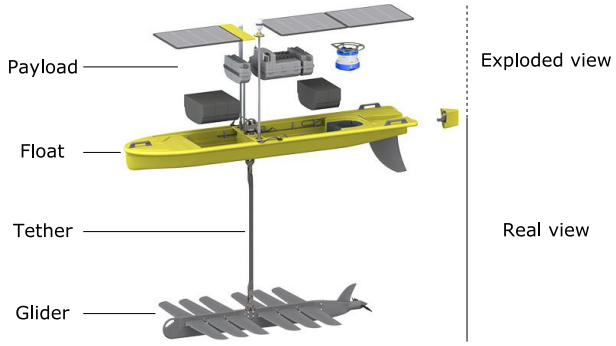

Figure 1.1: Wave Glider SV3 showing different components. The parts are labelled from top to bottom as: payload, float, tether, and glider. Adapted from [3].

which has a forward component and thus thrust is generated [1, 7]. This process occurs as the glider is ascending and descending, due to the range of motion of the fins, and is shown in Fig. 1.2.

The Wave Glider platform can be run in semi-autonomous or manual control mode. However, in both cases, the operator or pilot has limited or delayed information about the present sea state and environmental factors, such as current, wind, and chop. Thus the pilot cannot use this information to control the platform or compensate for any path error when navigating. Dynamic analysis of these hybrid vessels is still incomplete, especially when incorporating the present sea conditions with the wave-driven propulsion on which the platform relies. This lack of model fidelity limits platform autonomy as realistic interaction models are needed to improve platform control.

1.2 Problem statement and goals

Because of the limited dynamic analysis of hybrid vessels, this research project centres on the development of a three dimensional dynamic model for the Wave Glider, with a focus on the platform's interaction with the sea state. The dynamic model simulates the characteristics of the real-life system and has its basis in Lagrangian modelling. Other than the rigid body motion, which is characterised by the Lagrangian modelling, this research characterises the hydrostatic, buoyancy, and hydrodynamic, damping and added mass, effects which provide a dynamic model with sufficient fidelity. To improve the platform autonomy, a suitable platform heading controller is necessary for the underwater glider heading angle, which depends on both the rudder angle and the glider velocity, which itself is dependent on the sea state.

Thus the goals of this research project are to:

1. investigate and understand marine modelling conventions,
2. generate a 3D dynamic model of the wave glider platform including buoyancy and hydrodynamic characteristics,
3. validate the performance of the model,
4. design and simulate a heading controller for the glider rudder, taking into account the platform's response to a given sea state,
5. investigate the interaction of the model with sea states and steering optimisation based on the sea state.

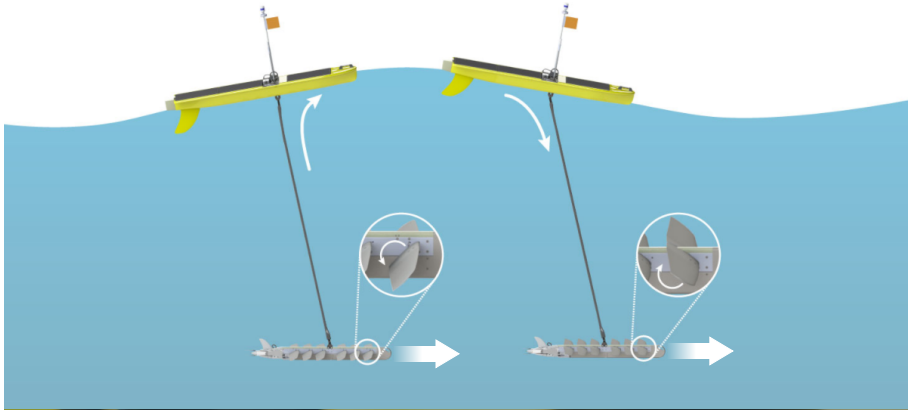

Figure 1.2: Operation of the Wave Glider. The rotation of the hydrofoils as the float moves up and down on the sea surface is shown, and the relative motion between the glider and the surrounding water generates thrust. Adapted from [3].

1.3 Scope and limitations

The scope of this project includes, but is not be limited to: generating a dynamic model of the Wave Glider platform, validating the performance of the model, implementing a control system that utilises the wave-powered propulsion system to increase speed providing better navigational capabilities.

This project did not investigate estimating the sea state from the information gathered by the Wave Glider, but rather use a pre-defined sea state on which the Wave Glider model will be tested. The operating area of the Wave Glider will be considered small and thus flat Earth navigation is assumed. Damping factors pertaining to wave-drift damping and potential damping are not included in this dissertation as initially more major contributing factors for the Wave Glider, specifically skin damping and damping due to vortex shedding, must be characterised. When considering the dynamics of the Wave Glider, the tether was assumed to be rigid, as during the operation of the Wave Glider the tether will generally remain taut: when the float is cresting on a wave the glider is also pulled up via the tether, while when the float is dipping into a trough the glider will be pulling down due to the mass of the glider, and in both situations the glider will be propelled forward, leading to the tether remaining taut. This will be the general case as the glider has significant weight, however in rough sea states the vertical oscillation of the float may have a high frequency and in that situation the tether may go slack regardless of the horizontal motion of the glider.

1.4 Plan of development

This dissertation begins by describing the necessary theory used to characterise the dynamics of the Wave Glider in Chapter 2. Initially marine modelling conventions are investigated followed by Lagrangian modelling and reference frame conventions. Chapter 2 also summarises previous work pertaining to the Wave Glider and concludes with a short investigation into computational fluid dynamic (CFD) and added mass methods.

The modelling methodology used to the characterise the rigid-body motion, buoyancy force, hydrodynamic forces, added mass, rudder forces, and hydrofoil motion and forces, are presented

in Chapter 3. This chapter provides sufficient detail for the dynamic modelling of the Wave Glider by presenting the different characteristics and including these characteristics into the equations of motion.

The control scheme is developed in Chapter 4 where the controller design takes the form of a cascaded feedback loop. This chapter explains how the controllers are developed, what form the controllers and the plants take, and how the saturation of the controllers is managed.

Chapter 5 shows the results attained when including the hydrodynamic factors and added mass. The results are validated by showing the incremental impact the hydrodynamic factors and added mass have on the rigid-body Wave Glider model.

The controller for the Wave Glider model is developed in Chapter 6. The controller design makes use of Quantitative Feedback Theory (QFT) methods that allows for robust control of the glider heading angle. The developed control scheme is evaluated for a specified sea state to determine if it is suitable with regards to the desired navigation and the consideration of the sea state.

The effect of the sea state is investigated in Chapter 7. The average velocity is determined for incident waves approaching the Wave Glider model from different directions. A proposed sinusoidal navigation strategy is tested for a sinusoidal sea state.

The discussion pertaining to the results shown in Chapters 5, 6, and 7, and their relevance is presented in Chapter 8.

Finally the conclusions for this dissertation are presented in Chapter 9 along with suggestions for future work resulting from this study.

Chapter 2

Background and related work

2.1 Modelling of marine vehicles

Nautical modelling provides a well-defined foundation on which to base the modelling of the Wave Glider platform. However, the majority of marine vessels (ships, buoys, remotely operated underwater vehicles (ROVs), etc.) are modelled as single bodies [8]. Although, single body modelling is currently insufficient for the multi-body Wave Glider system, it has been extended for this application as many aspects will be similar, including the required reference frames and corrective forces like buoyancy.

Much of the nomenclature used in kinetics for marine vessels is that recommended by "The Society of Naval Architects and Marine Engineers" (SNAME) [9], however some further nomenclature will be defined throughout the report to encapsulate the Wave Glider system and the methods used suitably.

2.1.1 Reference frames

Reference frames allow for the description of properties of a body or bodies, such as position and velocity, relative to other bodies or an inertial frame with a known position and orientation. This is an incredibly powerful tool as it allows a generalised method to relate properties between different frames as well as allowing for the definition of properties in frames that simplify equations, such as the definition of a body-fixed velocity with regards to defining the drag on a body.

The six degrees of freedom (DOF) for a marine vessel in the body-frame are defined as *surge, sway, heave, roll, pitch* and *yaw*. These terms describe the translational motions along the x-, y- and z-axes and the rotational motion about the x-, y- and z-axes, respectively [9], where these axes are fixed on the body frame, $\{b\} = [x_b, y_b, z_b]$, as shown in Fig. 2.1. The nomenclature is such that $\{b\}$ refers to the specific frame, in this case the body frame and $[x_b, y_b, z_b]$ are the axis that define that frame. The definitions for the respective forces and moments, linear and angular velocities, and position and Euler angles can be seen in Table 2.1.

The body-fixed frame can be related to the North-East-Down (NED) frame, $\{n\} = [x_n, y_n, z_n]$, which is defined relative to the Earth's reference ellipsoid [10]. The NED frame is tangential to the Earth's surface, where the axes are such that the x-axis always points to true North, the y-axis points towards East and finally the z-axis points down towards the centre of the Earth.

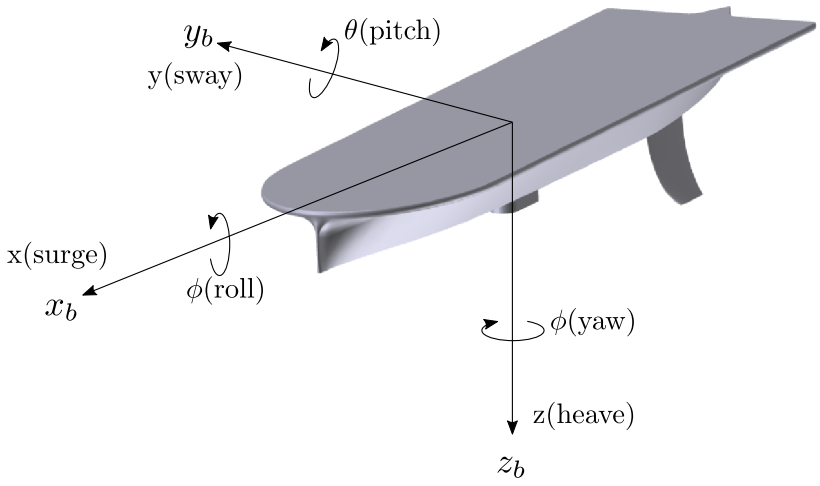

Figure 2.1: Six degrees of freedom for a single body expressed in the body frame, $\{b\}$, using the SNAME notation for marine vessels. Translational motion (surge, sway, heave) in and rotational motion (roll, pitch, yaw) about the x-, y-, and z-axes are indicated.

Table 2.1: SNAME notation for single body marine vessels [9].

Degrees of Freedom (DOF)		Forces and Moments	Linear and Angular Velocities	Positions and Euler Angles
1	linear motion in x-direction - surge	X	u	x
2	linear motion in y-direction - sway	Y	v	y
3	linear motion in z-direction - heave	Z	w	z
4	rotation about x-axis - roll	K	p	ϕ
5	rotation about y-axis - pitch	M	q	θ
6	rotation about z-axis - yaw	N	r	ψ

The NED frame can be related to the Earth-centred-Earth-fixed (ECEF) frame, $\{e\}$, by two angles which denote the longitude and latitude, shown in Fig. 2.2, where the ECEF frame rotates about the Earth-centered inertial (ECI) frame, $\{i\}$, at a fixed rate. The ECI frame has a fixed orientation and is located at the centre of the Earth.

The ECEF axis frame can be considered inertial for marine craft moving at slow speeds, and for craft operating in a local area with fixed latitude and longitude the NED frame can be considered inertial such that Newton's laws still apply [8]. Thus when referencing the coordinates in the NED frame, $\{n\} = [x_n, y_n, z_n]$, the frame can be considered inertial and globally defined.

The positions, velocities, forces and moments that are needed to express the dynamic model, are summarised into the vector notation below:

Inertial position: $p = \begin{bmatrix} x \\ y \\ z \end{bmatrix}$ Attitude(Euler angles): $\Theta_{b/n} = \begin{bmatrix} \psi \\ \theta \\ \phi \end{bmatrix}$

Body-fixed linear velocity: $v^b_{b/n} = \begin{bmatrix} u \\ v \\ w \end{bmatrix}$ Body-fixed angular velocity: $\omega^b_{b/n} = \begin{bmatrix} p \\ q \\ r \end{bmatrix}$

Body-fixed force: $f^b = \begin{bmatrix} X \\ Y \\ Z \end{bmatrix}$ Body-fixed moment: $m^b = \begin{bmatrix} K \\ M \\ N \end{bmatrix}$.

The superscript in the vector notation shows in which frame the vector is expressed, with inertial being assumed if not stated. The subscript in the vector notation shows which frames are being compared, such that $v^b_{b/n}$ is the linear velocity v of the body frame, $\{b\}$, relative to the inertial frame, $\{n\}$, expressed in the body frame.

This leads to fully locating and defining the motion of a single body with 6 degrees of freedom with an inertial position, body-fixed velocity and external force and moments being expressed respectively as [8]:

$$\eta = \begin{bmatrix} p \\ \Theta_{b/n} \end{bmatrix}, \quad \nu = \begin{bmatrix} v^b_{b/n} \\ \omega^b_{b/n} \end{bmatrix}, \quad \tau = \begin{bmatrix} f^b \\ m^b \end{bmatrix}. \tag{2.1}$$

When decomposing the body velocity into the NED frame, an Euler angle transformation is needed. The transform makes use of three principal rotation matrices to rotate the body frame onto the NED frame. Each of the rotation matrices based on the Euler angles is denoted respectively for: roll(ϕ), pitch(θ), and yaw(ψ) in Eq. 2.2, 2.2, and 2.4.

$$\mathbf{R}_{x,\phi} = \begin{bmatrix} 1 & 0 & 0 \\ 0 & \cos(\phi) & -\sin(\phi) \\ 0 & \sin(\phi) & \cos(\phi) \end{bmatrix} \tag{2.2}$$

$$\mathbf{R}_{y,\theta} = \begin{bmatrix} \cos(\theta) & 0 & \sin(\theta) \\ 0 & 1 & 0 \\ -\sin(\theta) & 0 & \cos(\theta) \end{bmatrix} \tag{2.3}$$

$$\mathbf{R}_{z,\psi} = \begin{bmatrix} \cos(\psi) & -\sin(\psi) & 0 \\ \sin(\psi) & \cos(\psi) & 0 \\ 0 & 0 & 1 \end{bmatrix} \tag{2.4}$$

For the linear velocities this transformation is simple and the required rotation matrices for roll, pitch, and yaw are given in Eq. 2.5 such that the NED velocity vector is given in Eq. 2.6.

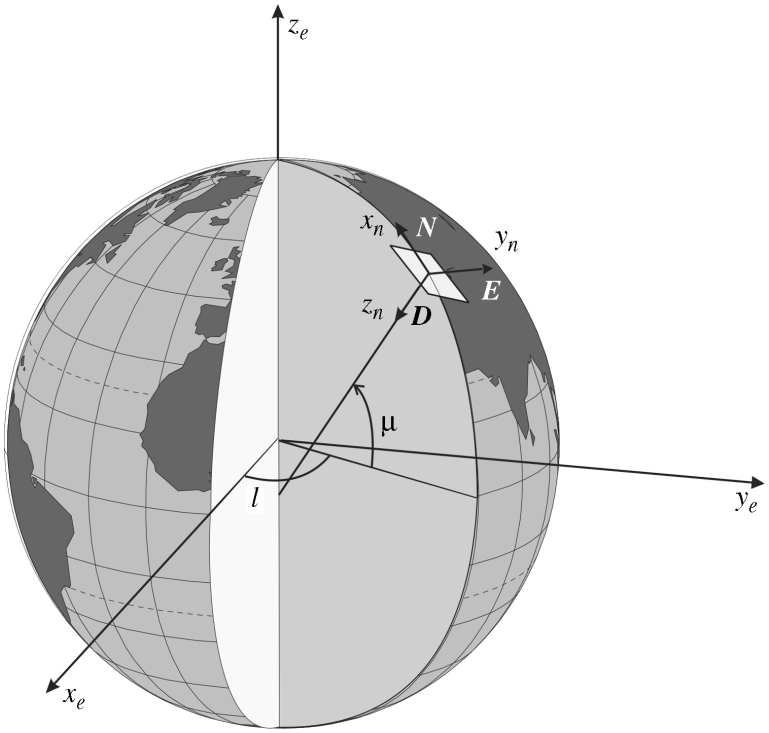

Figure 2.2: NED frame, $\{n\}$, being positioned at longitude l and latitude μ with reference to ECEF frame, $\{e\}$. Taken from [8].

It is convention to describe the rotation in terms of rotations about the z, y, and x axes (zyx convention). The transform $\mathbf{R}_b^n$ represents the transformation from frame $\{b\}$ to frame $\{n\}$, and the transform $\mathbf{R}_{x,\phi}$ represent the rotation of the current frame about the x-axis for an angle of ϕ.

$$\begin{aligned}\mathbf{R}_b^n(\Theta_{b/n}) &= \mathbf{R}_{z,\psi}\mathbf{R}_{y,\theta}\mathbf{R}_{x,\phi} \\ &= \begin{bmatrix} \cos(\psi)\cos(\theta) & -\sin(\psi)\cos(\phi)+\cos(\psi)\sin(\theta)\sin(\phi) & \sin(\psi)\sin(\phi)+\cos(\psi)\cos(\phi)\sin(\theta) \\ \sin(\psi)\cos(\theta) & \cos(\psi)\cos(\phi)+\sin(\phi)\sin(\theta)\sin(\psi) & -\cos(\psi)\sin(\phi)+\sin(\theta)\sin(\phi)\cos(\psi) \\ -\sin(\theta) & \cos(\theta)\sin(\phi) & \cos(\theta)\cos(\phi) \end{bmatrix}\end{aligned} \tag{2.5}$$

$$\dot{p}_n = \mathbf{R}_b^n(\Theta_{b/n})v_{b/n}^b. \tag{2.6}$$

However, for the angular velocities, the integral of the body-fixed angular velocity has no direct physical interpretation as the angular rate may contribute to multiple angles differently to the ordering of the Euler rotation. Thus the transform is slightly more complex. The transform, $\mathbf{T}_\Theta(\Theta_{b/n})$, is defined in Eq. 2.8 and the relation between the body-fixed angular velocity, $\omega_{b/n}^b$, and the Euler rate vector, $\dot{\Theta}_{nb}$, in Eq. 2.9.

$$\omega_{b/n}^b = \begin{bmatrix}\dot{\phi}\\0\\0\end{bmatrix} + \mathbf{R}_{x,\phi}^T\begin{bmatrix}0\\\dot{\theta}\\0\end{bmatrix} + \mathbf{R}_{x,\phi}^T\mathbf{R}_{y,\theta}^T\begin{bmatrix}0\\0\\\dot{\psi}\end{bmatrix} = \mathbf{T}_\Theta^{-1}(\Theta_{b/n})\dot{\Theta}_{nb}. \tag{2.7}$$

$$\mathbf{T}_{\Theta}^{-1}(\Theta_{b/n}) = \begin{bmatrix} 1 & 0 & -\sin(\theta) \\ 0 & \cos(\phi) & \cos(\theta)\sin(\phi) \\ 0 & -\sin(\phi) & \cos(\theta)\cos(\phi) \end{bmatrix} \Rightarrow \mathbf{T}_{\Theta}(\Theta_{b/n}) = \begin{bmatrix} 1 & \sin(\phi)\tan(\theta) & \cos(\phi)\tan(\theta) \\ 0 & \cos(\phi) & -\sin(\phi) \\ 0 & \sin(\phi)/\cos(\theta) & \cos(\phi)/\cos(\theta) \end{bmatrix}. \tag{2.8}$$

$$\dot{\Theta} = \mathbf{T}_{\Theta}(\Theta_{b/n})\omega_{b/n}^{b}. \tag{2.9}$$

It can be seen that the transform, $\mathbf{T}_{\Theta}(\Theta_{b/n})$, is undefined for a pitch of $\theta = \pm\frac{\pi}{2}$ radians because of the division by $\cos(\theta)$. This can play an important role in underwater unconstrained vessels, like ROVs, and should operation near this singularity be needed, the kinetics should be described by two Euler angle representations with different singularities such that switching between the two kinetic equations could avoid either singularity. Another alternative is a quaternion representation. However, surface vessels are unlikely to operate close to a pitch angle of $\pm\frac{\pi}{2}$ radians and therefore the transform $\mathbf{T}_{\Theta}(\Theta_{b/n})$ is valid [8].

2.1.2 Six degree of freedom rigid-body model

The rigid-body kinetics of a single body can be expressed in the form of Eq. 2.10 [8]:

$$\mathbf{M}_{RB}\dot{v} + \mathbf{C}_{RB}(v)v = \tau_{RB}, \tag{2.10}$$

where $\mathbf{M}_{RB}$ is the rigid-body mass matrix and $\mathbf{C}_{RB}(v)$ is the velocity-dependent Coriolis and centripetal force matrix caused by the rotation of the body frame about the inertial NED frame. The body-fixed velocity vector, $v = [u, v, w, p, q, r]^T$, and the generalised force and moment vector, $\tau_{RB} = [X, Y, Z, K, M, N]^T$, are expressed in the body frame.

To generalise the equation of motion, two body-fixed reference points will be used: the origin of the body frame, CO, and the centre of mass of the body, CG. The relationship between these points and the inertial frame is shown in Fig. 2.3. Two assumptions are made: the first is that the body is rigid, and the second is that the NED frame is inertial.

The equations for the linear motion of the centre of gravity can now be developed based on Euler's first axiom, defined in Eq. 2.11 and 2.12. Euler's first axiom states that the rate of change of the linear momentum, p_{cg}, in the inertial frame is proportional to the force, f_{cg}, acting on the body, where m is the mass of the body and $v_{cg/n}$ is the velocity of the CG of the body in the inertial frame. This axiom is an expression of Newton's second law in terms of conservation of linear momentum.

$$\frac{d}{dt}p_{cg} = f_{cg} \tag{2.11}$$

$$p_{cg} = mv_{cg/n} \tag{2.12}$$

The definition of the equations of motion through the body's CG can be extended to define the translational motion of the body through the origin of the body reference frame, where the CG is a vector r_g^b from the frame's origin. This more generalised case is shown in Eq. 2.13, where m

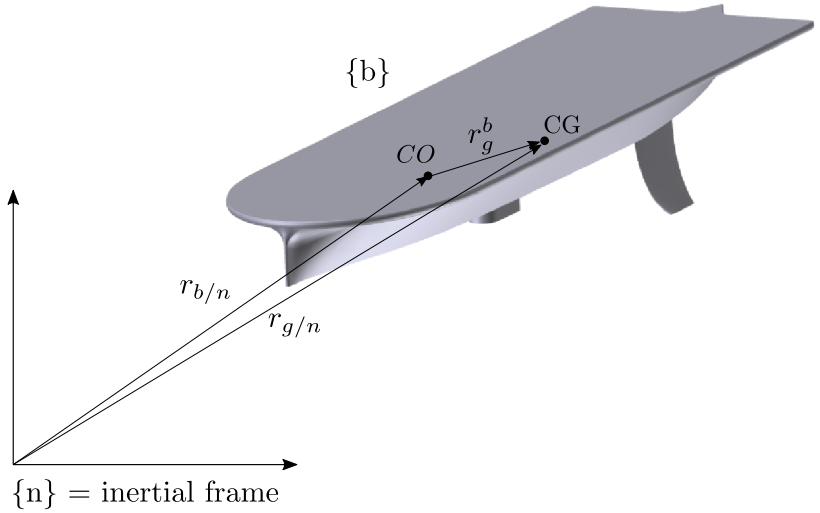

Figure 2.3: Definition of the centre of origin, CO, and centre of gravity, CG. The CG of the float is given as a position vector $r_{g/n}$ away from the origin of the inertial frame as well as a vector r_g^b away from the CO, defined in the body-fixed frame.

is the rigid body mass, $v_{b/n}^b$ is the translational velocity of the body frame, $\omega_{b/n}^b$ is the angular velocity of the body frame and $f^b = [X, Y, Z]^T$ is the force on CO.

$$m[\dot{v}_{b/n}^b + \dot{\omega}_{b/n}^b \times r_g^b + \omega_{b/n}^b \times v_{b/n}^b + \omega_{b/n}^b \times (\omega_{b/n}^b \times r_g)] = f^b \tag{2.13}$$

For the rotational motion of the body, Euler's second axiom, shown in Eq. 2.14 defines that for a body the moments about the CG are equal to the derivative of the angular momentum:

$$\frac{d}{dt} h_{cg} = m_{cg}, \tag{2.14}$$

where the angular momentum about the CG is the product of the inertial tensor about the CG, I_{cg}, and the angular velocity, shown in Eq. 2.16.

$$h_{cg} = I_{cg} \omega_{b/i}. \tag{2.15}$$

The angular momentum can be defined with respect to the origin of the body frame, CO, by integrating over the volume of the body and determining the angular momentum at each point, shown in Eq. 2.17. [11].

$$h_{co} = \int_V (r \times v_e) \rho dV, \tag{2.16}$$

where r is the position for a volume element dV with density ρ travelling with velocity v_e.

The equation of motion for rotational motion can thus be defined, in Eq. 2.17:

$$I_{co}\dot{\omega}_{b/n}^b + \omega_{b/n}^b \times I_{co}\omega_{b/n}^b + m r_g \times (\dot{v}_{b/n}^b + \omega_{b/n}^b \times v_{b/n}^b) = m^b, \tag{2.17}$$

where I_{co} is the inertial tensor for the body about CO and $m^b = [K, M, N]^T$ is the moment about CO.

The inertial tensor for the body about the origin, CO, is defined in Eq. 2.18.

$$I_{co} = \begin{bmatrix} I_x & -I_{xy} & -I_{xz} \\ -I_{yx} & I_y & -I_{yz} \\ -I_{zx} & -I_{zy} & I_z \end{bmatrix} \tag{2.18}$$

Thus from Eq. 2.13 and Eq. 2.17 the equations of motion in each of the degrees of freedom making use of the SNAME definitions in Table 2.1 are defined in Eq. 2.19 – 2.24.

$$m[\dot{u} - vr + wq - x_g(q^2 + r^2) + y_g(pq - \dot{r}) + z_g(pr + \dot{q}))] = X \tag{2.19}$$

$$m[\dot{v} - wp + ur - y_g(r^2 + p^2) + z_g(qr - \dot{p}) + x_g(qp + \dot{r})] = Y \tag{2.20}$$

$$m[\dot{w} - uq + vp - z_g(p^2 + q^2) + x_g(rp + \dot{q}) + y_g(rq + \dot{p})] = Z \tag{2.21}$$

$$\begin{aligned} I_x\dot{p} + (I_z - I_y)qr - (\dot{r} + pq)I_{xz} + (r^2 - q^2)I_{yz} + (pr - \dot{q})I_{xy} \\ +m[y_g(\dot{w} - uq + vp) - z_g(\dot{v} - wp + ur)] = K \end{aligned} \tag{2.22}$$

$$\begin{aligned} I_y\dot{q} + (I_x - I_z)rp - (\dot{p} + qr)I_{xy} + (p^2 - r^2)I_{zx} + (qp - \dot{r})I_{yz} \\ +m[z_g(\dot{u} - vr + wq) - x_g(\dot{w} - uq + vp)] = M \end{aligned} \tag{2.23}$$

$$\begin{aligned} I_z\dot{r} + (I_y - I_x)pq - (\dot{q} + rp)I_{yz} + (q^2 - p^2)I_{xy} + (rp - \dot{p})I_{zx} \\ +m[x_g(\dot{v} - wp + ur) - y_g(\dot{u} - vr + wq)] = N \end{aligned} \tag{2.24}$$

The rigid-body equations of motion can be expressed in vectorial form [8]:

$$\mathbf{M}_{RB}\dot{v} + \mathbf{C}_{RB}(v)v = \tau_{RB}, \text{ where} \tag{2.25}$$

$$\mathbf{M}_{RB} = \begin{bmatrix} m & 0 & 0 & 0 & mz_g & -my_g \\ 0 & m & 0 & -mz_g & 0 & mx_g \\ 0 & 0 & m & my_g & -mx_g & 0 \\ 0 & -mz_g & my_g & I_x & -I_{xy} & -I_{xz} \\ mz_g & 0 & -mx_g & -I_{yx} & I_y & -I_{yz} \\ -my_g & mx_g & 0 & -I_{zx} & -I_{zy} & I_z \end{bmatrix}, \tag{2.26}$$

$$\mathbf{C}_{RB} = \begin{bmatrix} 0 & 0 & 0 \\ 0 & 0 & 0 \\ 0 & 0 & 0 \\ -m(y_gq + z_gr) & m(y_gp + w) & m(z_gp - v) \\ m(x_gq - w) & -m(z_gr + x_gp) & m(z_gq + u) \\ -m(x_gr + v) & m(y_gr - u) & -m(x_gp + y_gq) \end{bmatrix}$$

$$\begin{bmatrix} m(y_gq + z_gr) & -m(x_gq - w) & -m(x_gr + v) \\ -m(y_gp + w) & m(z_gr + x_gp) & -m(y_gr - u) \\ -m(z_gp - v) & -m(z_gq + u) & m(x_gp + y_gq) \\ 0 & -I_{yz}q - I_{xz}p + I_zr & I_{yz}r + I_{xy}p - I_yq \\ I_{yz}q + I_{xz}p - I_zr & 0 & -I_{xz}r - I_{xy}q + I_xp \\ -I_{yz}r - I_{xy}p + I_yq & I_{xz}r + I_{xy}q + I_xp & 0 \end{bmatrix}. \tag{2.27}$$

2.1.3 Hydrostatic and hydrodynamic factors

A body moving through a viscous medium will have several dispersive forces acting on it due to the relative velocity between the body and the medium. These can be classified into restorative hydrostatic forces, environmental forces, and hydrodynamic forces which consist of radiation-induced forces and damping [8].

The hydrostatic restorative forces are based on Archimedes' principle for buoyancy, Eq. 2.28, as well as the gravitational force, Eq. 2.29, acting on the body. These forces act along the vertical

axis of the inertial NED frame, where m is the mass of the body, g is the gravitational constant, ρ is the density of the displaced medium, and V is the volume of the displaced medium. The restorative buoyancy force on the body, which acts due to the pressure differential across the body, is thus given in Eq. 2.30, where $r_b^b = [x_b, y_b, z_b]$ is the vector from the CO to the centre of buoyancy, f_g^b is the force of gravity in the body frame, and f_b^b is the buoyancy force in the body frame. The centre of buoyancy is the centroid of the submerged portion of the body, which may change due to the orientation and submersion level of the body.

$$B = \rho g V, \qquad f_b^n = -\begin{bmatrix} 0 \\ 0 \\ B \end{bmatrix}, \qquad f_b^b = R_b^n(\Theta_{b/n})^{-1} f_b^n. \tag{2.28}$$

$$W = mg, \qquad f_g^n = \begin{bmatrix} 0 \\ 0 \\ W \end{bmatrix}, \qquad f_g^b = R_b^n(\Theta_{b/n})^{-1} f_g^n. \tag{2.29}$$

$$G(\eta) = \begin{bmatrix} f_g^b + f_b^b \\ r_g^b \times f_g^b + r_b^b \times f_b^g \end{bmatrix}. \tag{2.30}$$

The hydrodynamic forces consist of the radiation-induced forces and viscous damping [8]. The radiation-induced forces are composed of two components: added mass and potential damping, and characterise the conservation of momentum effects from motion through a viscous medium. The added mass is represented by a mass matrix, $\mathbf{M}_A$, and a Coriolis and centripetal matrix, $\mathbf{C}_A$, and is due to the kinetic energy needed to overcome the inertia of the surrounding medium. The potential damping, $\mathbf{D}_P$, is the energy lost to generating surface waves.

$$\tau_R = -\mathbf{M}_A \dot{v}_r - \mathbf{C}_A v_r - \mathbf{D}_P v_r. \tag{2.31}$$

The viscous damping forces are composed of three components: skin damping, wave drift damping, and damping due to vortex shedding. The skin damping is caused by friction and other effects at the contact surface between the body and the medium. Wave drift damping is caused by the induced oscillation from incident waves. Finally, damping due to vortex shedding is explained by the motion of the body through a medium causing areas of low pressure behind the body, taking the form of vortices, and the tendency of a body to move into these areas of low pressure.

$$\tau_D = -\mathbf{D}_S v_r - \mathbf{D}_W v_r - \mathbf{D}_V v_r. \tag{2.32}$$

The environmental forces are specifically the forces of waves and the wind acting on the body. These effects are superimposed linearly and defined in Eq. 2.33.

$$w = \tau_{wind} + \tau_{wave}. \tag{2.33}$$

The equation of motion that incorporates the dispersive forces is shown in Eq. 2.34.

$$\mathbf{M}_{RB}\dot{v} + \mathbf{C}_{RB}(v)v + \mathbf{M}_A \dot{v}_r + \mathbf{C}_A(v_r)v_r + \mathbf{D}_P v_r + G(\eta) = \tau_{RB} + \tau_D + w. \tag{2.34}$$

2.2 Lagrangian modelling

Lagrangian modelling is used extensively in robotic applications and provides a convenient method to model multi-body systems [12]. The technique is based on energy balance and eliminates the need to solve for constraint forces between rigid-body elements in the system. The Lagrangian describes the system by comparing the kinetic energy, T, and potential energy, V, of the system. These energies are dependent on a set of independent, generalised coordinates, q, where the number of generalised coordinates and the number of constraints on the system determine the degrees of freedom. If the position of the k^{th} element or body in the system, p_k, is defined in terms of the generalised coordinates by making use of the transform from the body-frame to the inertial frame, $\mathrm{T}(q)$, applied to the centre of mass of the element in the body-frame, r_k, then the velocity can also be defined in terms of the generalised coordinates, Eq. 2.35 and 2.36 respectively. Thus the kinetic energy, potential energy, and Lagrangian for the system can be defined in Eq. 2.37, 2.38, and 2.39 respectively, where m_k is the scalar mass of the element, v_k is the linear velocity vector of the body in the inertial frame, J_k is the moment of inertia matrix about the CO, ω_k is the angular velocity vector of the body in the inertial frame, and h_k is the height of the centre of mass of the body in the inertial frame. The kinetic energy, T, is the sum of the kinetic energy of each element in the system and similarly the potential energy, V, is the sum of the potential energy of each element in the system [12].

$$p_k(q) = \mathrm{T}(q) r_k \tag{2.35}$$

$$v_k = \frac{dp_k}{dq}\dot{q} \tag{2.36}$$

$$T = \sum^{k} \frac{1}{2} m_k v_k^T v_k + \frac{1}{2} \omega_k^T J_k \omega_k \tag{2.37}$$

$$V = \sum^{k} m_k g h_k \tag{2.38}$$

$$L = T - V \tag{2.39}$$

Making use of the principle of virtual work, δw expressed in Eq. 2.40, a force, f, in i directions, r, can be treated as a generalised force, Q, acting through j generalised coordinates, q. As the work done by the force f and the generalised force Q are equivalent, the j^{th} component of the generalised force, Q_j, can be written in a general form given in Eq. 2.41, where f_i is a force with components in the directions of r_i, and r_i is defined in terms of the generalised coordinates, q.

$$\delta w = \sum_i f_i \cdot \delta r_i = \sum_j Q_j \delta q_j, \tag{2.40}$$

$$Q_j = \sum_i f_i \cdot \frac{\partial r_i}{\partial q_j}. \tag{2.41}$$

Thus the Lagrangian equations of motion for each generalised coordinate can be calculated as shown in Eq. 2.42.

$$\frac{d}{dt}\left(\frac{\partial L}{\partial \dot{q}_j}\right) - \frac{\partial L}{\partial q_j} = Q_j. \tag{2.42}$$

2.3 Denavit-Hartenberg reference frames

When considering a multi-body system, the reference frames for a single body vessel expressed in Subsection 2.1.1 can form the basis of the referencing system, however this referencing must be extended. The Denavit-Hartenberg (DH) convention is commonly used in robotic kinematic chains and parametrises the transform between elements, known as links, through joints, where the links are connected. A modified DH convention [12] is expressed below and will be used in this application.

The convention fixes frames onto each link at the joint and adheres to certain rules that allows the transform between frames to be defined by four parameters rather than six. This frugal parametrisation is achieved by ensuring that the x-axis of a frame both intersects and is perpendicular to the preceding frame's z-axis. The four parameters for the transform from a previous frame $(i-1)$ to frame i are link length, a_i, link twist, α_i, joint offset, d_i, and joint angle, θ_i, shown in Fig. 2.4.

To assign the frames onto the system, the links in the chain are labelled from 1 to N with the 0^{th} frame assigned to the base or the inertial frame. The joints are then labelled from 1 to N such that the i^{th} joint lies between the previous link $(i-1)$ and link i. The z_i axis is then assigned along the axis of joint i. The expected motion at the joint defines the axis of the joint, such that for translational motion the axis is in the direction of the translation and for rotational motion the axis is the axis about which the rotation occurs. Finally, in reverse order for convenience, the x_{i-1} axis is defined normal to the z_i and z_{i-1} axis. An example of the frame assignment is shown in Fig. 2.5. The y-axes can be assigned to conform to the right-hand rule. The transform parameters are defined such that: a_i is the distance from z_{i-1} to z_i along the x_{i-1} axis, α_i is the angle from z_{i-1} to z_i about the x_{i-1} axis, d_i is the distance from x_{i-1} to x_i along the z_i axis, and θ_i is the angle from x_{i-1} to x_i about the z_i axis. This allows for the definition of the transform from a previous frame $(i-1)$ to frame i in Eq. 2.43, where $Rot(x_{i-1}, \alpha_i)$ defines a rotation of α_i about the x-axis of frame $(i-1)$, and $Tran(x_{i-1}, a_i)$ defines a translation of a_i along the x-axis of frame $(i-1)$.

$$
\begin{aligned}
\mathrm{T}_i^{i-1} &= Rot(x_{i-1}, \alpha_i) Tran(x_{i-1}, a_i) Rot(z_i, \theta_i) Tran(z_i, d_i) \\
&= \begin{pmatrix}
\cos(\theta_i) & -\sin(\theta_i) & 0 & a_i \\
\sin(\theta_i)\cos(\alpha_i) & \cos(\theta_i)\cos(\alpha_i) & -\sin(\alpha_i) & -\sin(\alpha_i) d_i \\
\sin(\theta_i)\sin(\alpha_i) & \cos(\theta_i)\sin(\alpha_i) & \cos(\alpha_i) & \cos(\alpha_i) d_i \\
0 & 0 & 0 & 1
\end{pmatrix}
\end{aligned}
\tag{2.43}
$$

2.4 Platform modelling

Little dynamic modelling has been published for the Wave Glider as it is a relatively new class of marine research vessel and previous work has focused on the modelling of single body USVs and UUVs. A brief review of similar multi-body marine platform modelling will now be presented.

When looking at previous modelling of hybrid marine systems, some of the earlier work by Caiti [13] centred around a modified underwater model of the Wave Glider, Fig. 2.6. The inertial frame is defined by $\{b\} = [x_b, y_b, z_b]$, with frames 1 and 2 representing the translation along the inertial x and z axes, respectively. Frame 3 characterises the pitch of the upper

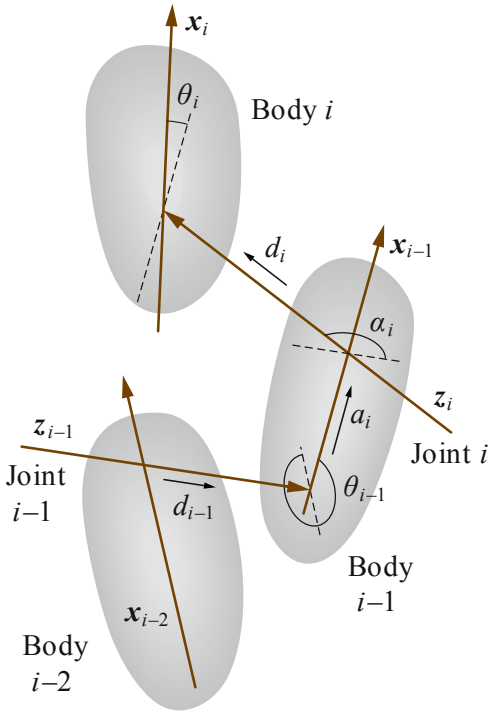

Figure 2.4: Example of DH parameters for three arbitrary bodies. Joint offset d_{i-1} defines the distance from x_{i-2} to x_{i-1} along z_{i-1}. Joint angle θ_{i-1} defines the angle from x_{i-2} to x_{i-1} about z_{i-1}. Link length a_i defines the distance from z_{i-1} to z_i along x_{i-1}. Link angle α_i defines the angle from z_{i-1} to z_i about x_{i-1} and joint offset d_i defines the distance from x_{i-1} to x_i along z_i. Taken from [12].

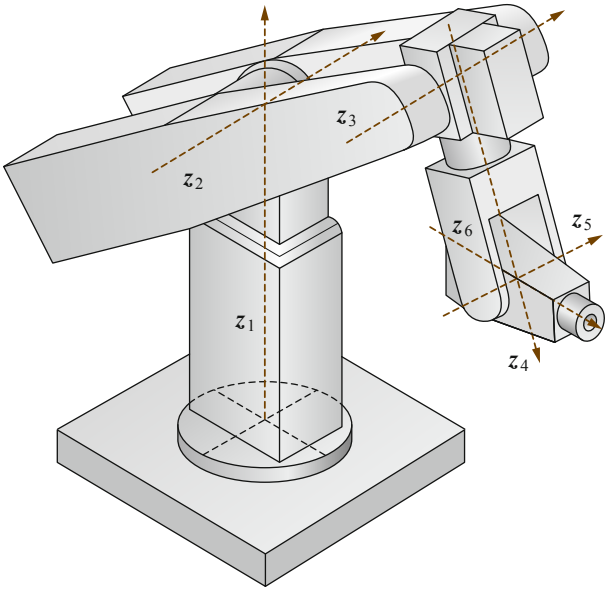

Figure 2.5: Example of frame definition for a serial chain manipulator. The articulated robotic arm has six degrees of freedom defined by six reference frames with a spherical wrist. There is no joint offset between the frames. Taken from [12].

body, and frame 4 characterises the angle of the tether linking the upper body to the lower body, which has a link length of a_1. Finally frame 5 defines the pitch of the lower body, with e defining the position of the end effector. The work consisted of a longitudinal planar model developed using DH reference frames and Lagrangian modelling. The drag on the system was considered element-wise and in the local frame of the element and then transformed into the inertial frame. The limitation of this model is the fact that it only considers a two dimensional simulation of the system. The modelling did not consider hydrodynamic factors other than skin friction or the interaction of the model with a sea state.

Kraus [7] created a model for the Wave Glider, representing the system as a single body attached by the tether with two weights on either end, relating to the glider and the float. Reference frames for the float, (F_X, F_Y, F_Z), the system's CG, (O_X, O_Y, O_Z), and the glider, (G_X, G_Y, G_Z) are defined, as well as the transform from frames F and G to the system CG frame and from the system CG frame to the NED frame. This simplified model had 6 DOF with reference to Fig. 2.7: translation in the O_X and O_Y directions for the system, roll about the O_X axis for the system, pitch about the O_Y axis for the system, yaw about the F_Z axis for the float, and yaw about the G_Z axis for the glider. Although Kraus's model was considered in three dimensions the z motion (motion in the heave direction) was not included in the modelling as it was considered to be sinusoidal and periodic.

Tian [14] developed a full three dimensional model of the Wave Glider which allowed for translation along the x-, y- and z-axes of the inertial base frame, roll and yaw of the float, pitch of the tether, pitch and yaw of the glider, pitch of the hydrofoils, and an angle of attack of the water flow relative to the hydrofoils. The referencing made use of DH parametrisation and is shown in Fig. 2.8. Tian used Lagrangian mechanics to define the dynamic model of the Wave Glider, but did not consider how this model could interact with the sea state in terms of navigation.

One possible limitation of generating a dynamic model of the Wave Glider is that each element must be characterised properly otherwise the model will be inaccurate. As such, regressive modelling for the purposes of generating an estimate of the Wave Glider velocity provides another avenue to allow for more autonomous path planning. This kind of modelling can be used in off-line trajectory planning and initially Smith [15] made use of linear regressive modelling based on six sea parameters. The parameters used were: significant wave height, wave peak period, wave direction offset from the Wave Glider course, wind speed along the Wave Glider body-frame surge axis, subsurface current speed along the Wave Glider body-frame, and an estimate of the surface current speed. Making use of a 80%/20% split between training and test datasets, Smith was able to make an estimate of the Wave Glider speed with a correlation of 0.6176 and 0.5953 between the true and predicted velocities when compared to the training and test datasets.

Smith's work was extended by Ngo [16] using non-linear regression methods, specifically Gaussian process regression. A 70%/30% segmentation of training to test data was used with various covariance functions that used a zero mean function for the regression. It was found that little improvement could be made when using the same sea parameters, and thus sparse environment data were used: power spectral density, ellipticity, direction, spread, kurtosis, and skewness. It was found that making use of the power spectral density and ellipticity to generate multiple Gaussian process models with bootstrap aggregating resulted in a correlation of 0.9728, however noting that the bootstrap aggregating provided significantly more accurate predictions using smaller training datasets. This may have allowed more of the variability of the data to be captured and thus further investigation into different sampling and segmentation may be warranted. Ngo [17] extended the non-linear Gaussian process regression by incorporating forecasting strategies. Predictions from a wave model, specifically WAVEWATCH III [18], were

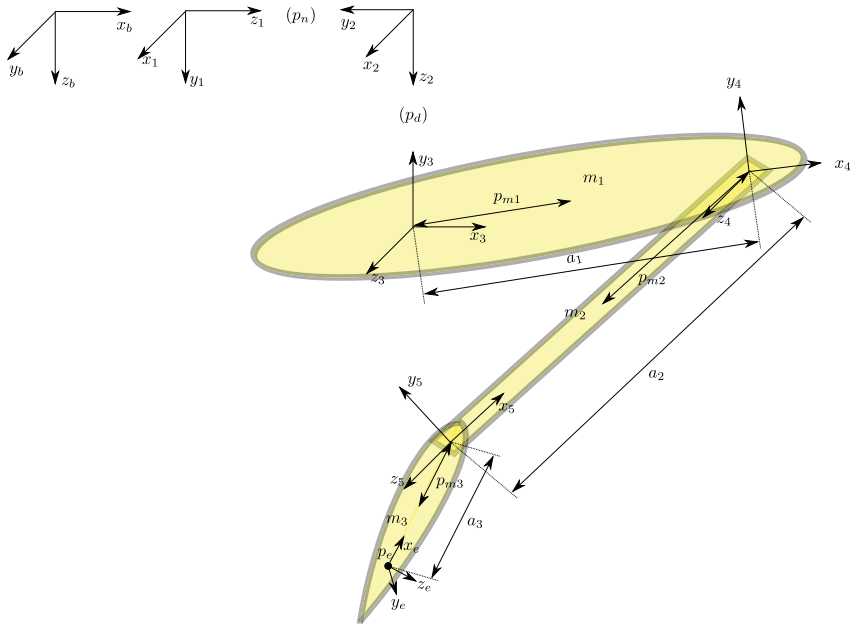

Figure 2.6: Specification of DH-reference frames for modelling done by Caiti. Taken from [13].

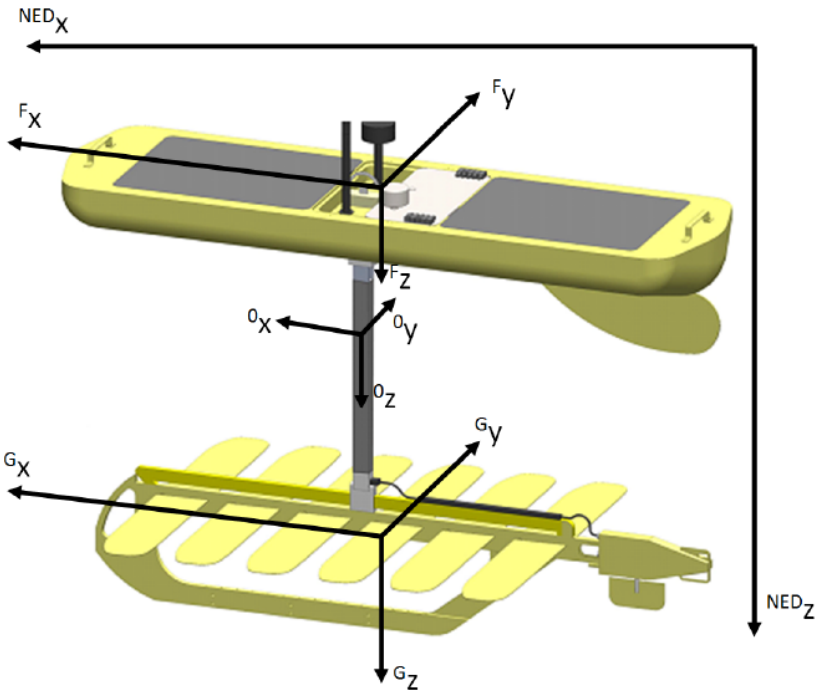

Figure 2.7: Relationship between float reference frame, (F_X, F_Y, F_Z), glider reference frame, (G_X, G_Y, G_Z), system centre of gravity frame, (O_X, O_Y, O_Z), and NED reference frame. Taken from [7].

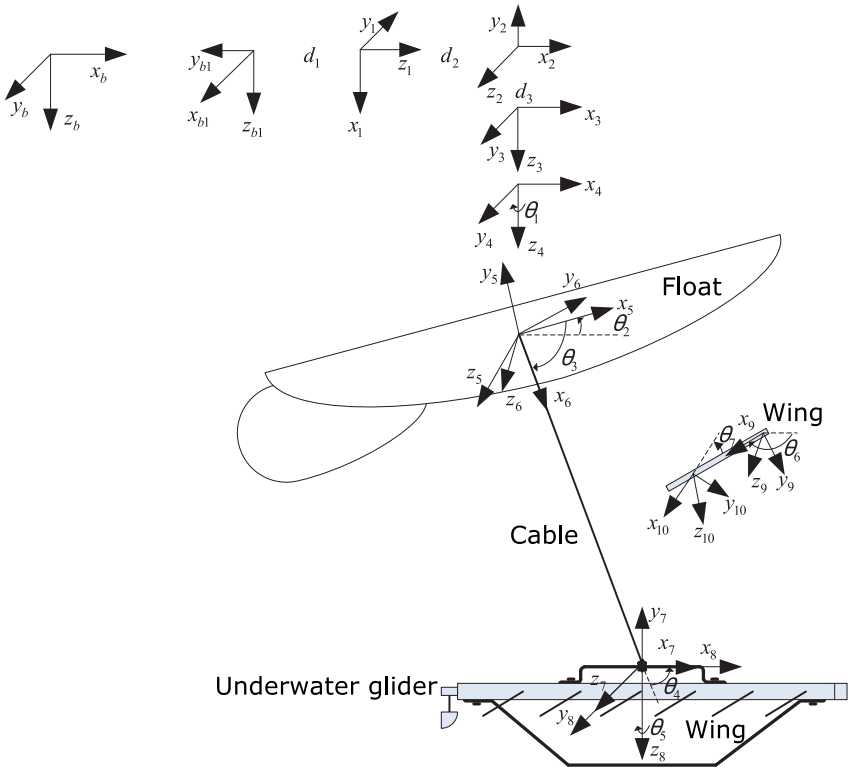

Figure 2.8: Model for Wave Glider platform as generated by Tian. Taken from [14]. The DH reference frames are given with the frame $b = [x_b, y_b, z_b]$ showing the inertial frame. The generalised coordinates are shown on the figure, $q = (d_1, d_2, d_3, \theta_1, \theta_2, \theta_3, \theta_4, \theta_5, \theta_6, \theta_7)$.

used and this resulted in a good estimate of the Wave Glider speed.

The possible limitation of the above-mentioned estimation approaches is that they use averaged and forecasted sea state parameters, such as: significant wave height, peak period and power spectral density, rather than the instantaneous sea state used in this dissertation. As a result, the use of these estimation approaches in on-board path planning is likely limited as their focus is off-board planning.

2.5 Computational fluid dynamics

This section aims to provide an introduction to computational fluid dynamics (CFD), its usefulness, and its relevance in this dissertation, particularly pertaining to the use of SolidWorks 2015 Flow Simulator. It should be noted that this introduction is made from an electrical engineering context and CFD is not generally a speciality of the field.

CFD is the methodology of providing discrete solutions, in space and time, for continuous fluid flow scenarios. This is done by discretising the fluid domain into a grid or mesh, which contains the model through or in which the fluid flow is to be examined. The governing equations are then solved iteratively at discrete points on the mesh. The flow variable between these points is interpolated based on the values at the discrete mesh points. CFD provides a reliable and suitably accurate alternative to determining flow parameters, such as drag and lift, as compared to the time- and resource-intensive procedure of physical experimentation [19]. Additionally, CFD packages such as SolidWorks Flow Simulator can be utilised very easily and with little

risk allowing for rapid engineering analysis and design.

When building an understanding of CFD it is helpful to examine the governing equations. The Reynolds-averaged Navier-Stokes (RANS) equations, which govern the motion of fluids, are solved iteratively together with the continuity equation to simulate certain fluid flow scenarios. The RANS equation is presented in Eq. 2.44 [20]:

$$\begin{aligned}\rho\left(\mathbf{U}\cdot\nabla\mathbf{U}\right)+\nabla\cdot\left(\mu_T\left(\nabla\mathbf{U}+\left(\nabla\mathbf{U}\right)^T\right)-\frac{2}{3}\mu_T\left(\nabla\cdot\mathbf{U}\right)\mathbf{I}\right)=\\ -\nabla\mathbf{P}+\nabla\cdot\left(\mu\left(\nabla\mathbf{U}+\left(\nabla\mathbf{U}\right)^T\right)-\frac{2}{3}\mu\left(\nabla\cdot\mathbf{U}\right)\mathbf{I}\right)+\mathbf{F},\end{aligned} \tag{2.44}$$

where $\mathbf{U}$ is the time-averaged fluid velocity, ρ is the fluid density, $\mathbf{P}$ is the time-averaged fluid pressure, μ is the fluid viscosity, μ_T represents the turbulent viscosity, and $\mathbf{F}$ is the external force on the fluid. The continuity equation is presented in Eq. 2.45, where $\mathbf{u}$ is the fluid velocity. The RANS equation and the continuity equation are solved together as the RANS equation represents the conservation of momentum while the continuity equation represents the conservation of mass.

$$\frac{\partial\rho}{\partial t}+\nabla\cdot\left(\rho\mathbf{u}\right)=0 \tag{2.45}$$

Some of the important properties that determine how accurate a CFD simulation is are discussed briefly below, making note particularly on how they affect this dissertation.

Mesh

The mesh used in the flow scenario defines how refined the discretisation of the continuous scenario is. The mesh must be sufficiently fine to resolve the flow, which is particularly important for turbulent flows, however a finer mesh requires more computation and time to solve, and a mesh that is not fine enough can lead to inaccurate results. SolidWorks has the benefit of automatically generating the mesh for a particular flow scenario based on the model that is being tested. The main drawback of this feature is the limited control in being able to define the mesh.

Computational domain

The computational domain in a CFD analysis defines the size of the domain through which the flows are calculated. The computational domain must be large enough that it sufficiently characterises the slowly decaying flow effects which occur far from the model, however is limited in size as a larger computational domain requires more time to solve. A method is proposed in [21] where the computational domain for a complex shaped ROV is increased until the variation in the results for the hydrodynamic damping parameter is negligible. This paper shows that the deviations in the results are negligible for a computational size that is 20 times larger than the characteristic dimension in each dimension. This approach is recommended, however due to time constraints and to reduce the solving time to be within a suitable margin, a smaller computational domain was used.

Turbulent flow

For very simple flow conditions, the flow scenario will likely consist strictly of laminar flow, however when considering a flow scenario with obstructions, such as those used in the CFD analysis of the drag coefficients for an ROV, there may also be turbulent flow conditions. Simple scenarios, which exhibit laminar flow, will often have definite solutions for the RANS equation. However when including turbulent flow, numerical methods are required to solve the flow scenario.

The Reynolds number is a good indicator of whether the flow will be laminar or turbulent for a given flow scenario, and is shown in Eq. 2.46 where Re denotes the Reynolds number, ρ is the density of the fluid, v is the relative velocity of the fluid and the body, L is the characteristic dimension of the surface: for a flat plate the characteristic dimension is the distance from the leading edge, and μ is the dynamic viscosity of the fluid.

$$Re = \frac{\rho v L}{\mu} \tag{2.46}$$

The Reynolds number represents the ratio of the inertial forces to the viscous forces. Low Reynolds numbers indicate laminar flow as the inertial forces are small relative to the viscous forces, as such any disturbances are dissipated. High Reynolds numbers indicate turbulent flow as the inertial forces are adequate to amplify triggering mechanisms, however when considering the complex geometry of ROVs there is the possibility that there could be local areas of turbulence for low Reynolds numbers. When considering the critical value at which the transition from laminar to turbulent flow begins, a representative value of 5×10^5 is often assumed for calculations involving a flat plate [20, 22].

Turbulent flow is a chaotic state of motion where the three dimensional velocity and pressures change continuously in time within a substantial region of the flow, resulting in intense mixing and vortices. The turbulent viscosity is represented in the RANS equation as μ_T, and is modelled in CFD programs most commonly for industrial applications using the k-ϵ turbulence because the model is robust and computationally inexpensive. The k-ϵ model describes the turbulent flow through two transport equations, partial differential equations (PDEs). The first transport variable defines the energy in the turbulence given by the turbulent kinetic energy, k, and the second transport variable represents the rate of dissipation of the turbulent energy given by the turbulent dissipation, ϵ. Other models such as the Shear-Stress-Transport (SST) model have been shown to yield good results when considering the damping on ROVs [21], however only the k-ϵ turbulence model is available in SolidWorks Flow Simulator and thus the k-ϵ turbulence model is used in this dissertation.

Boundary conditions

The boundary conditions for a flow scenario are made up of, but not limited to: inlets, outlets and wall conditions (no-slip or free-slip). The boundary conditions for a flow simulation are a major contributing factor to the accuracy of the results as they define the operating region of the modelled system and determine how similar the simulated flow environment is to the actual operational environment. As the use of CFD analysis for ROVs is largely for external flow scenarios the inlets and outlets are defined by the boundaries of the computational domain. The wall conditions are defined as free-slip boundary conditions as this represents an unbound body of water such that the fluid would experience zero shear stress at the boundary.

2.6 Empirical estimates for added mass

This section gives a brief explanation of the empirical estimates used in the calculation of added mass.

Strip theory

Strip theory [23] allows for the calculation of the added mass components using the assumption that added mass components of a 3D body can be represented as the sum of the components of the 2D strips that make up the body. Fig. 2.9 shows how a 3D parallelepiped body can be characterised by a set of 2D rectangular strips, such that added mass contribution in the direction of the y-axis of the 3D body, $A_{22}^{(3D)}$, can be represented as the sum of the added masses of the rectangular strips with added mass $A_{22}^{(2D)}$. This model assumes that the variation in the flow in the cross-sectional plane is much greater than the variation in the flow in the longitudinal plane for a defined motion, which does not hold at the ends of a body, resulting in some error in the calculation of the added mass components. Thus strip theory provides the best results when the length of the body is much greater than the width of the body, implying that the end effects would be insignificant. Strip theory is commonly used because it provides an easier alternative to more complex methods which often do not provide substantially more accurate results [24].

3D empirical data

An alternative to using 2D reference geometry and strip theory is to make use of 3D shapes that have empirical or analytical solutions. Because shapes like rectangular prisms are very common and can be related to ROVs there exists very accurate empirical data, such as that provided by Det Norske Veritas (DNV) [25]. However, when relating bodies like ROVs to the 3D shapes that have empirical data some consideration need to be made. One such fact to be considered is that many ROVs are not solid bodies and thus the added mass components acquired from empirical data need to be scaled according to the ratio of the volume of the ROV to the volume of the 3D shape.

When considering the use of empirical data for initially characterising the added mass of the Wave Glider it can be seen that empirical data have been used to give a good estimate of the added mass of other ROVs. When compared to a WADAM-analysis (wave analysis by diffraction and Morisen theory) the empirical data have been shown to have a general accuracy within about $\pm 10\%$ [24].

This chapter introduced the nautical modelling theory pertaining to single body motion which forms the basis of the Wave Glider model. The nautical theory was extended to multi-body systems using Lagrangian modelling techniques and a DH referencing parametrisation. Previous work on the Wave Glider was considered and shows the limited dynamic modelling for this hybrid system. Finally a brief introduction to CFD and empirical data for the calculation of added mass was shown to be useful to improve the fidelity of the Wave Glider model by allowing for calculation of the hydrodynamic factors.

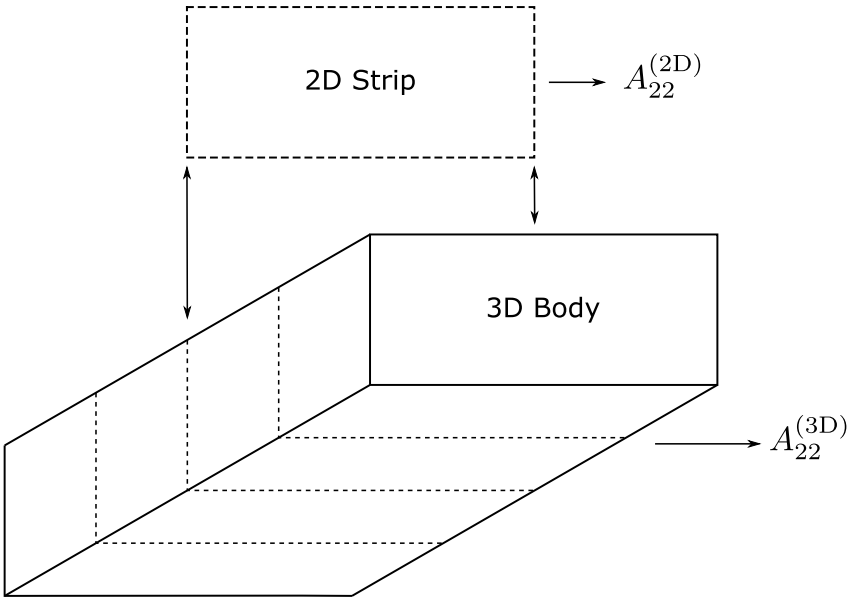

Figure 2.9: 2D rectangular strips that can be used to make a 3D parallelepiped body. Added mass component for 3D body in y-axis, $A_{22}^{(3D)}$, can be represented as sum of added mass components for rectangular strips, $A_{22}^{(2D)}$. Adapted from [24].

2.7 Summary

This concludes the review of the literature pertaining to the generation of the Wave Glider model. The referencing convention and single body model investigated in the marine modelling context are extended using the DH convention and Lagrangian techniques. Considering previous work on the Wave Glider presents an opportunity for a full dynamic model that focuses on the interaction of the model with the sea state. Finally, CFD analysis for the calculation of hydrodynamic forces and empirical methods for the calculation of added mass were investigated.

Chapter 3

Modelling of the Wave Glider Platform

The three dimensional model of the Wave Glider that was generated as the focus of this dissertation made use of 12 degrees of freedom. The model's degrees of freedom comprise: translational displacement (x_f, y_f, z_f) and angular rotation $(\phi_f, \theta_f, \psi_f)$ for the float, rolling and pitching for the tether (ϕ_t, θ_t), angular rotation for the glider $(\phi_g, \theta_g, \psi_g)$, and pitching of the glider's hydrofoil fins (θ_a). The yaw of the glider's rudder (ψ_r) is the controllable input into the system. These degrees were defined by making use of a DH parametrisation. When defining the body-fixed frame for a body, the NED referencing convention is maintained.

Along with the rigid body motion defined by the Lagrangian, the three-dimensional model includes: buoyancy acting on the float which is dependent on the sea state, buoyancy forces on the glider, added mass effects, and hydrodynamic forces for drag and generating propulsion based on flow simulation data.

Please note that in the modelling methodology below there are several simplifications used to make the text easier to read. The "Wave Glider system" refers to the 12 degree of freedom system characterised by the Lagrangian equations of motion. Hydrodynamic forces refer to the forces and moments generated by the drag and lift characteristics of a body moving through water with a density, $\rho = 1000$ kg·m^{-3}.

3.1 DH parametrisation

The DH parameters for the three dimensional model of the Wave Glider are shown in Table 3.1 and the resulting reference frames are shown in Figure 3.1. It is taken that the NED frame is inertial because of the low speed and local vicinity application of the Wave Glider in this dissertation. Frames 1 to 3 allow for the translation of the system with the origin of frame 3 fixed onto the centre of the body of the float. Frame 1 will always be a distance y_f displaced from the inertial frame along the z_1-axis, frame 2 will be displaced a distance x_f along the z_2-axis away from frame 1, and frame 3 will similarly be displaced a distance z_f. The origins of frames 4 and 5 are fixed on the centre of the body of the float while frame 6 is fixed on the float body. Frames 4, 5 and 6 allow for the angular rotation of the float. The origins of frames 7 and 8 are fixed at the connection between the float and the tether and allow for rolling and pitching of the tether. The origins of frames 9, 10 and 11 are fixed onto the centre of the body of the

glider with frame 11 fixed to the body of the glider. Frames 9, 10 and 11 allow for angular rotation of the glider. Finally frame 12 is fixed to the first set of hydrofoil fins and allow for the pitching of the fins. Thus the complete transform from the inertial frame to the hydrofoil frame is given by Eq. 3.1, where $\mathbf{T}_1^0(y_f)$ defines that the DH transform from frame 1 to frame 0 for the characteristic variable y_f. If the characteristic variable is a length then it defines a translational joint offset transform while if the variable is an angle is defines a rotational joint angle transform.

$$\mathbf{T}_{12}^0 = \mathbf{T}_1^0(y_f)\mathbf{T}_2^1(x_f)\mathbf{T}_3^2(z_f)\mathbf{T}_4^3(\psi_f)\mathbf{T}_5^4(\theta_f)\mathbf{T}_6^5(\phi_f)\mathbf{T}_7^6(\phi_t)\mathbf{T}_8^7(\theta_t)\mathbf{T}_9^8(\phi_g)\mathbf{T}_{10}^9(\theta_g)\mathbf{T}_{11}^{10}(\psi_g)\mathbf{T}_{12}^{11}(\theta_a) \tag{3.1}$$

The centres of mass of the float, tether and glider bodies are specified with a DH transformation, Eq. 3.2, 3.3, and 3.4, respectively. The centre of mass of one of the hydrofoils is specified in Eq. 3.5. The vector r denotes the vector from the centre of the reference frame to the centre of mass of the body, where the subscript defines the body. The vector d denotes the vector from the centre of the reference frame to the connection of the tether, where the subscript defines the order as well as the reference frame.

$$p_f = \mathbf{T}_6^0 r_f^b \tag{3.2}$$

$$p_t = \mathbf{T}_6^0(d_{ft}^b + \mathbf{T}_8^6 r_t^b) \tag{3.3}$$

$$p_g = \mathbf{T}_6^0(d_{ft}^b + \mathbf{T}_8^6(d_{tg}^b + \mathbf{T}_{11}^8 r_f^b)) \tag{3.4}$$

$$p_a = \mathbf{T}_6^0(d_{ft}^b + \mathbf{T}_8^6(d_{tg}^b + \mathbf{T}_{12}^8 r_a^b)) \tag{3.5}$$

3.2 Lagrangian classification

The Lagrangian equations of motion are characterised by the generalised coordinate vector q in Eq. 3.6, where: x_f, y_f and z_f represent the translational displacement of the float, ϕ_f, θ_f and ψ_f represent the angular rotation of the float, ϕ_t and θ_t represents the rolling and pitching of the tether, ϕ_g, θ_g and ψ_g represent the angular rotation of the glider, and θ_a represents the pitching of the hydrofoils.

$$q^T = \begin{bmatrix} x_f, y_f, z_f, \phi_f, \theta_f, \psi_f, \phi_t, \theta_t, \phi_g, \theta_g, \psi_g, \theta_a \end{bmatrix}^T \tag{3.6}$$

The positions of the centres of mass for the float, tether, glider and hydrofoil are represented as three dimensional spatial vectors, Eq. 3.2, 3.3, 3.4, and 3.5 respectively, which can be differentiated to get the velocities in the inertial frame, Eq. 2.36.

Rather than simply generating the equations of motion in terms of the Lagrangian, the equations of motion can be generated in the same form as the nautical modelling of a single body, and similar robotic applications. The equations of motion are given in terms of the mass, Coriolis and centripetal, and restorative force matrices for convenience and to make these equations more understandable [26]. For a system of n generalised coordinates the mass matrix is defined in Eq. 3.7, the Coriolis and centripetal force matrix in Eq. 3.8, and the restorative force matrix

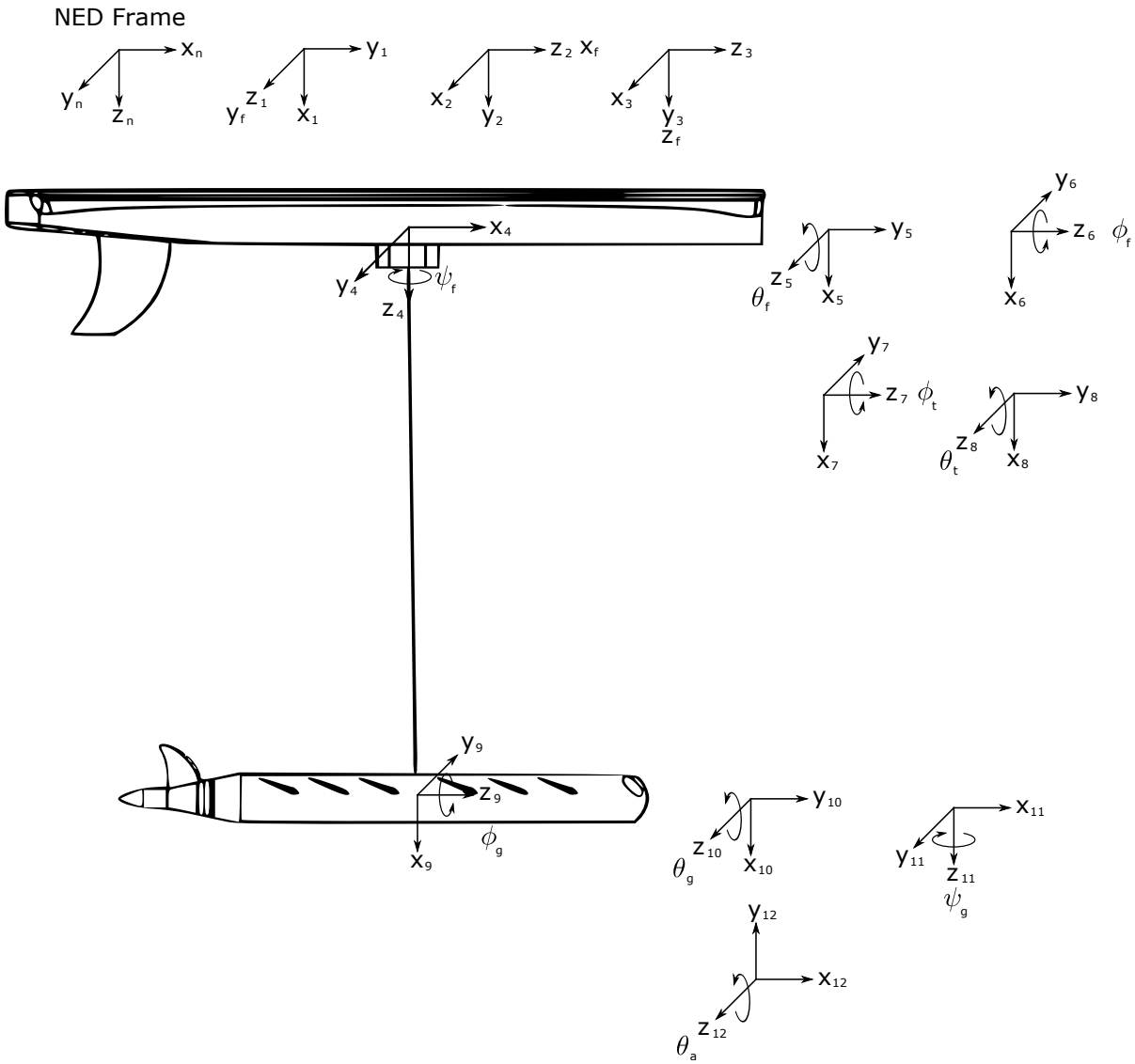

Figure 3.1: Definition of the DH reference frames for each of the generalised coordinates. Frames 1, 2 and 3 allow for the translation of the system along the y , x , and z axes, respectfully, such that the origin of frame 3 is fixed onto the body of the float. The origins of frames 4, 5 and 6 are fixed onto the centre of the body of the float and allow for yawing, pitching, and rolling of the float, respectfully, such that frame 6 is fixed onto the body of the float. The origins of frames 7 and 8 are located at the connection of the float and the tether and allows for rolling and pitching of the tether, respectfully. The origins of frames 9, 10, and 11 are fixed onto the centre of the body of the glider and allow for rolling, pitching, and yawing of the glider, respectfully, such that frame 11 is fixed onto the body of the glider. Frame 12 is fixed onto the connection between the glider and the first set of hydrofoil fins and allows for pitching of the hydrofoils.

Table 3.1: DH parameters for the three dimensional model of the Wave Glider characterised by 12 generalised coordinates and subsequently 12 reference frames.

Frame	a	α	d	θ	Joint variable
1	0	$-\frac{\pi}{2}$	y_f	$-\frac{\pi}{2}$	y_f
2	0	$-\frac{\pi}{2}$	x_f	$-\frac{\pi}{2}$	x_f
3	0	$-\frac{\pi}{2}$	z_f	$-\frac{\pi}{2}$	z_f
4	0	0	0	ψ_f	ψ_f
5	0	$-\frac{\pi}{2}$	0	$-\frac{\pi}{2}+\theta_f$	θ_f
6	0	$\frac{\pi}{2}$	0	ϕ_f	ϕ_f
7	0	0	0	$-\phi_f+\phi_t$	ϕ_t
8	0	$\frac{\pi}{2}$	0	$-\theta_f+\theta_t$	θ_t
9	l_t	$-\frac{\pi}{2}$	0	$-\phi_t+\phi_g$	ϕ_g
10	0	$\frac{\pi}{2}$	0	$\frac{\pi}{2}-\theta_t+\theta_g$	θ_gr
11	0	$\frac{\pi}{2}$	0	$-\psi_f+\psi_g$	ψ_g
12	0	$-\frac{\pi}{2}$	0	$-\theta_g+\theta_a$	θ_a

in Eq. 3.9. For Eq. 3.8, C_{ij} is the element of matrix $\mathbf{C}_{RB}$ in the i^{th} row and j^{th} column, and similarly for M_{ij}, whereas q_i is the i^{th} element of the generalised coordinates vector.

$$\mathbf{M}_{RB} = \frac{d}{d\dot{q}}\left(\left(\frac{dT}{d\dot{q}}\right)^T\right), \tag{3.7}$$

$$C_{ij} = \frac{1}{2}\sum_{k=1}^{n}\left(\frac{\partial M_{ij}}{\partial q_k} + \frac{\partial M_{ik}}{\partial q_j} + \frac{\partial M_{jk}}{\partial q_i}\right)\dot{q}_i, \qquad \mathbf{C}_{RB} \in \mathbb{R}^{n\times n}, \tag{3.8}$$

$$G = \left(\frac{dV}{dq}\right)^T. \tag{3.9}$$

The equations of motion for the model with generalised coordinates that includes only rigid-body motion is expressed in Eq. 3.10, where τ_{RB} represents the external forces and moments on the system, $\tau_{RB} \in \mathbb{R}^n$.

$$\mathbf{M}_{RB}(q)\ddot{q} + \mathbf{C}_{RB}(q,\dot{q})\dot{q} + G(q) = \tau_{RB} \tag{3.10}$$

3.3 Buoyancy

The calculation of the displaced volume of the float, the surface vessel, for the buoyancy force was handled outside of the Lagrangian equations of motion, and the buoyancy force treated as an external force. This was done as the buoyancy force on and CB of the float would change due to the float's submersion level and orientation. A Denaulay triangulation making use of Qhull [27] methods was used to determine the submerged volume of the float and the centre of buoyancy for the submerged region.

The body of the float was characterised by points chosen on the SolidWorks model such that the volume of the body generated from the triangulation of the chosen points was at least 99% similar to the volume of the SolidWorks model. The comparison of the reconstructed model and the SolidWorks model is shown in Fig. 3.2.

The limitation in using a Denaulay triangulation and Qhull is that the method could only be utilised for convex bodies. This was solved by resolving the float into bodies that were each convex.

The volume and centre of buoyancy for the submerged regions of the float were calculated making use of Algorithm 1 below. For each body making up the reconstructed float, the hull k is generated from the points P, which define that body, making use of the *convhull* method in MATLAB. The transform based on the generalised coordinates, $\mathbf{T}(q)$, is used to rotate the points of P such that the body has the correct orientation as defined by the generalised coordinates and stored as $P2$. The points of $P2$ that are below the sea surface based on the sea surface parameters are added to the matrix, N. For each of the points in N, the connected points are found. If the connected point are above the sea surface the intercept between the points and the sea surface are found. Each of these intercepts are added to the matrix $N2$, which are merged with N to generate $N3$, which defines the submerged region. The convex hull $k2$ is generated based off the points in $N3$. The Delaunay Triangulation, D, is generated from the connectivity map, $k2$, and the submerged points, $N3$. For each of the triangulations the volume, V_t, and centre of buoyancy, CB_t, is calculated. The total volume, V, is the summation of the volumes,

(a) MATLAB reconstruction **(b)** SolidWorks Model

Figure 3.2: Comparison between MATLAB reconstruction and SolidWorks model.

V_t; the final centre of buoyancy, CB, is the summation of the weighed centres of buoyancy, $V_t \times CB_t$.

To show the effect of Algorithm 1, Fig. 3.3 shows a comparison for the submerged regions of the float when the vessel is fully submerged with water level at -0.2 m as compared to when the water level is at 0 m for the centre of the float located at the origin. It is easy to see that when the float is fully submerged, Fig. 3.3a, that the entire float makes up the submerged region. When compared to a partially submerged float, Fig. 3.3b, it can be seen that the partially submerged region is far smaller and that the centre of buoyancy, shown by the blue marker, is lower.

Once the volume and centre of buoyancy of the submerged regions of the float were calculated the appropriate forces and moments needed to be applied to the system. The buoyancy force was calculated for the displaced volume, Eq. 3.11, where ρ is the density of the medium, g is the gravitational constant, and V is the displaced volume. The buoyancy force was treated as a generalised force acting at the centre of buoyancy.

$$f_b = \rho g V \tag{3.11}$$

The buoyancy force and centre of buoyancy for the glider were considered constant, as this vessel is always fully submerged such that there is no change in the buoyancy force or CB dependent on the glider's submersion level or orientation. Thus making use of the generalised force definition, given in Eq. 2.41, the buoyancy forces acting on the float and the glider were treated as generalised forces, $Q_b(q)$. The equations of motion for the rigid body system with buoyancy forces is given by Eq. 3.12.

$$\mathbf{M}_{RB}(q)\ddot{q} + \mathbf{C}_{RB}(q,\dot{q})\dot{q} + G(q) = \tau + Q_b(q) \tag{3.12}$$

Algorithm 1 Calculate Buoyancy

Require: Set of points on convex body, P. Generalised Coordinates, q. Sea surface parameters.

$k = convhull(P)$ ▷ Generates connectivity map for points P
$P2 = \mathbf{T}(q) \times P$ ▷ Transforms the points P into the inertial frame
for $P_i = P2$ **do** ▷ Determining submerged points
  if $P_i(3) < surface(P_i(1), P_i(2))$ **then**
    $N \leftarrow P_i$
for $N_i = N$ **do**
  $C = connections(N_i, k)$
  for $C_i = C$ **do**
    if $C_i(3) > surface(C_i(1), C_i(2))$ **then**
      $N2 \leftarrow intersection(N_i, C_i)$
$N3 = [N; N2]$
$k2 = convhull(N3)$ ▷ Generating connectivity map for submerged points
$D = delaunay(N3)$ ▷ Generate triangulation for submerged points
$V = 0, CB = 0$
for $D_i = D$ **do** ▷ Summing variables for triangulations
  $V_t = volume(D_i)$
  $CB_t = centre(D_i)$
  $V = V + V_t$
  $CB = CB + V_t \times CB_t$
return CB, V

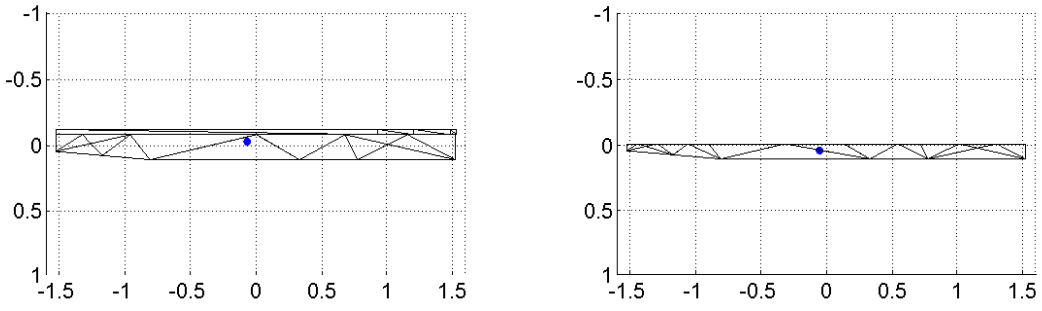

(a) Fully submerged vessel **(b)** Water level at 0 m

Figure 3.3: Change in submerged region and centre of buoyancy for fully submerged vessel, (a), compared to partially submerged vessel, (b). The centre of buoyancy is represented by the blue marker for each image.

3.4 Hydrodynamic force and added mass

Hydrodynamic forces (drag and lift) and added mass are often neglected in robotic modelling applications as the effect of these forces is negligible for operation in air and at low speed. However, the hydrodynamic forces and added mass for vehicles operating in water can be considerable and thus it is important to calculate reasonable estimates for these forces to ensure an accurate model.

3.4.1 Hydrodynamic force characterisation

The assumptions that were made to simplify the drag characterisation are specified in this section. The initial assumption was that the hydrofoils on the glider would assume a fixed angle depending on the vertical motion of the glider. This simplification reduces the number of simulations needed, where the maximum angle allowed by the glider because of mechanical constraints is $-20°$ and $40°$ with respect to the body-fixed frame, shown in Fig. 3.4. This was later extended upon when considering the hydrodynamic forces acting strictly on the hydrofoils and allows for the comparison of the full set of hydrofoils to the single set considered in the following sections. The glider should provide a forward propulsive force in terms of the body-fixed frame such that the glider will only be stationary or move forward, which again reduces the number of simulations needed.

SolidWorks 2015 Flow Simulator was selected to determine the hydrodynamic force due to its ease of use, the time limitation of the project and that it has been shown to provide a reasonable degree of accuracy [24]. Goals were used in Solidworks to track parameters that were key objectives for the simulation. Global goals calculate physical parameters in the entire computational domain, such as force in a specific direction, whereas surface goals calculate parameters on a specific surface. The modelling approach of the hydrodynamic forces made use of the fact that these forces could be superimposed linearly [28]. As such, the SolidWorks models for the float and glider were tested separately for different flow velocities and the resultant forces and moments in the body-fixed frame were stored. Six simulation velocities, $[0.1, 0.3, 0.5, 0.8, 1.1, 1.5]$ $\text{m}\cdot\text{s}^{-1}$, per fluid velocity direction were chosen to encompass the 1.5 $\text{m}\cdot\text{s}^{-1}$ maximum speed that was defined in the product specifications [29].

The forces and moments along the body-fixed axis were set as global goals acting through the CG of the body for the linear flow velocity tests, and in the case of the float, the computational domain was set to cover the relevant surfaces. For the rotational fluid velocity tests, global goals were used for the glider. Surface goals were used for the float testing as this allowed only the submerged surfaces to be specified. Thereafter the forces and moments were fitted to third order polynomials, such that they were dependent on the corresponding body-fixed velocity,

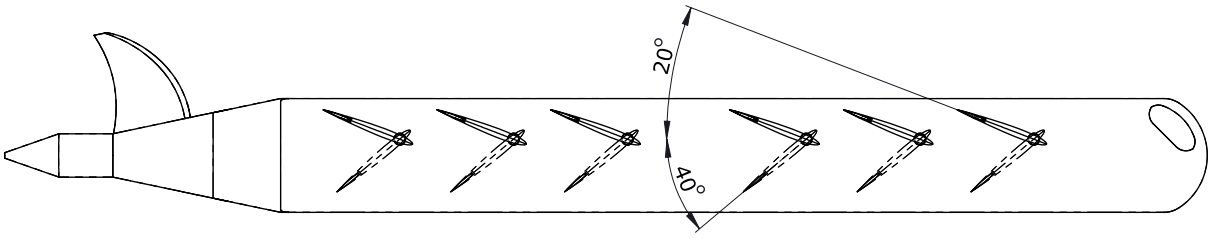

Figure 3.4: Assumed angles of glider for flow simulations. The hydrofoils are limited to an angle of $40°$ for positive rotation and $-20°$ for negative rotation with the y-axis coming out of the page.

captured the linear and quadratic damping coefficients, and characterised the non-symmetric geometry. The functions could then be implemented in the dynamic simulation to determine the hydrodynamic force acting on the system.

The simulation configuration is listed in Table 3.2 making note that: to reduce computation time some of the computational domains were adjusted to less than the recommended 20 times the characteristic length, and that the x-axis simulation domain was defined as symmetric.

The computational domain for the flow simulation of the glider body where the fluid velocity in the global coordinate system x-direction was set to 1.1 m·s^{-1} is shown in Fig. 3.5. This relates to a body-fixed x velocity of the glider of 1.1 m·s^{-1}. The flow velocities for the simulation are shown in Fig. 3.6

The results from the simulation run in Fig. 3.6 and the corresponding simulation for the x-direction fluid velocity simulations were then fitted to a third order polynomial as shown in Fig. 3.7. Third order polynomials were chosen to capture the possibly non-symmetric behaviour of the hydrodynamic forces due to the non-symmetric geometry of the bodies.

Thus the hydrodynamic force matrix for each body takes the form of Eq. 3.13, where $X_y(q, \dot{q})$ represents the hydrodynamic force fitted to a third-order polynomial in the body-fixed x-direction because of the body-fixed y-direction motion. The linear body-fixed velocities are calculated from the linear inertial velocities in terms of the generalised coordinates and velocities, q and $\dot{q}$. The polynomials for forces and moments due to glider motion in the x-direction, $(X_x, Y_x, Z_x, \Phi_x, \Theta_x, \Psi_x)$, are shown in Fig. 3.7.

$$D(q,\dot{q}) = \begin{bmatrix} X_x(q,\dot{q}) & X_y(q,\dot{q}) & X_z(q,\dot{q}) & X_\phi(q,\dot{q}) & X_\theta(q,\dot{q}) & X_\psi(q,\dot{q}) \\ Y_x(q,\dot{q}) & Y_y(q,\dot{q}) & Y_z(q,\dot{q}) & Y_\phi(q,\dot{q}) & Y_\theta(q,\dot{q}) & Y_\psi(q,\dot{q}) \\ Z_x(q,\dot{q}) & Z_y(q,\dot{q}) & Z_z(q,\dot{q}) & Z_\phi(q,\dot{q}) & Z_\theta(q,\dot{q}) & Z_\psi(q,\dot{q}) \\ \Phi_x(q,\dot{q}) & \Phi_y(q,\dot{q}) & \Phi_z(q,\dot{q}) & \Phi_\phi(q,\dot{q}) & \Phi_\theta(q,\dot{q}) & \Phi_\psi(q,\dot{q}) \\ \Theta_x(q,\dot{q}) & \Theta_y(q,\dot{q}) & \Theta_z(q,\dot{q}) & \Theta_\phi(q,\dot{q}) & \Theta_\theta(q,\dot{q}) & \Theta_\psi(q,\dot{q}) \\ \Psi_x(q,\dot{q}) & \Psi_y(q,\dot{q}) & \Psi_z(q,\dot{q}) & \Psi_\phi(q,\dot{q}) & \Psi_\theta(q,\dot{q}) & \Psi_\psi(q,\dot{q}) \end{bmatrix} \tag{3.13}$$

As the hydrodynamic forces are calculated for the float and glider bodies separately and in their respective body frames, the forces and moments from the hydrodynamic forces need to be correctly applied to the system. The resultant hydrodynamic forces and moments for a body are calculated first in the body frame, then the elements of the matrix are summed along the first dimension of the matrix, resulting in a 6×1 vector of three dimensional forces and three dimensional moments per body in the body-fixed axis, Eq. 3.14. The forces are rotated from the body frame into the inertial frame by the rotation matrix, R_b^i, in Eq. 3.15.

$$D_b = \begin{bmatrix} F_{bx} \\ F_{by} \\ F_{bz} \\ M_{bk} \\ M_{bm} \\ M_{bn} \end{bmatrix} = D(q,\dot{q}) \begin{bmatrix} 1 \\ 1 \\ 1 \\ 1 \\ 1 \\ 1 \end{bmatrix} \tag{3.14}$$

$$\begin{bmatrix} F_{ix} \\ F_{iy} \\ F_{iz} \end{bmatrix} = R_b^n \begin{bmatrix} F_{bx} \\ F_{by} \\ F_{by} \end{bmatrix} \tag{3.15}$$

Table 3.2: Flow Simulator settings for characterisation of hydrodynamic forces. *Automated computational domain was adjusted to only appropriate submerged float surfaces with the nominal water-level situated halfway up the lip of the float.

Subsystem	Body-fixed axis of motion	Comp. Domain Size (m^3)	Fin Angle (°)
Glider	+ve x-direction	$12 \times 4 \times 2.6$	-20
	+ve x-direction	$12 \times 4 \times 2.6$	40
	+ve y-direction	$4.5 \times 2.5 \times 5$	-20
	+ve y-direction	$4.5 \times 2.5 \times 5$	40
	+ve z-direction	$7.8 \times 17.4 \times 10$	-20
	-ve z-direction	$7.8 \times 17.4 \times 10$	40
	+ve x-rotation	Auto	0
	+ve y-rotation	Auto	0
	-ve y-rotation	Auto	0
	+ve z-rotation	Auto	0
Float	+ve x-direction	Auto*	
	-ve x-direction	Auto*	
	+ve y-direction	Auto*	
	+ve z-direction	Auto*	
	+ve x-rotation	Auto	
	+ve y-rotation	Auto	
	-ve y-rotation	Auto	
	+ve z-rotation	Auto	

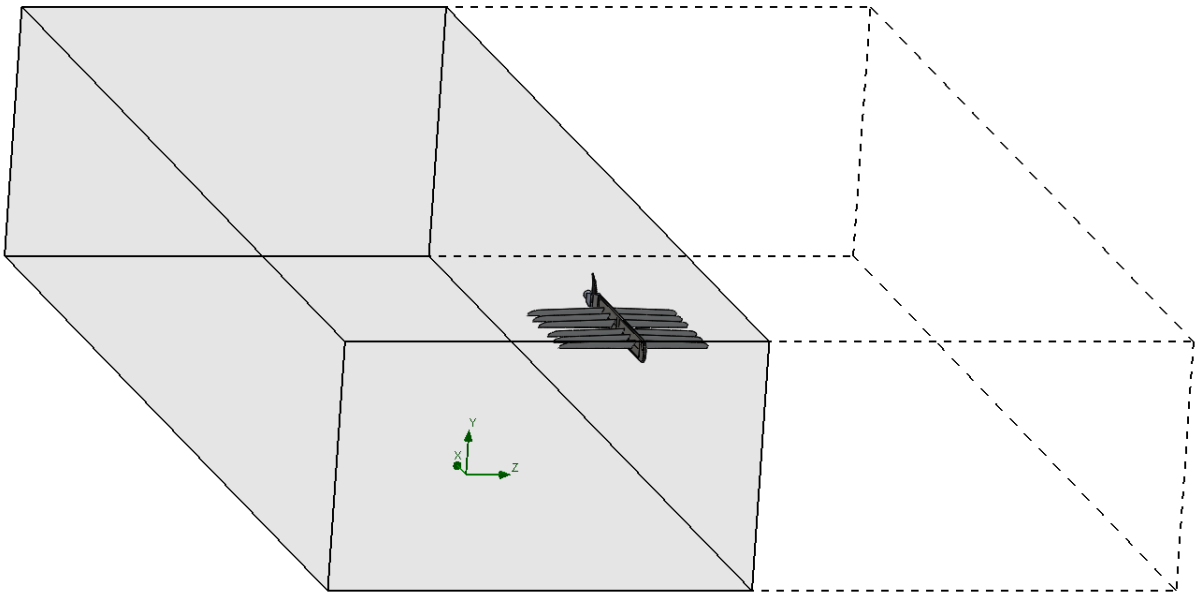

Figure 3.5: Example of computational domain for the glider body for fluid velocity of 1.1 $m \cdot s^{-1}$ in global coordinate system x-direction, where symmetry is defined about the x-y plane.

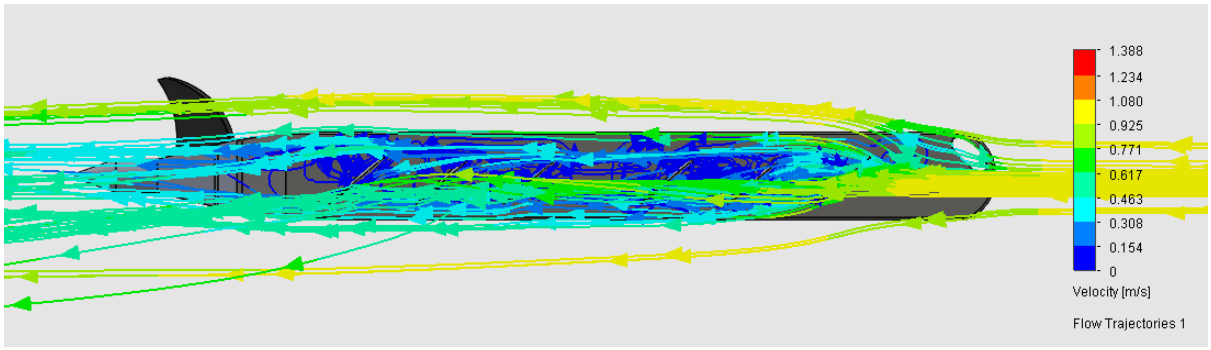

Figure 3.6: Flow velocity representation for 1.1 $\mathrm{m{\cdot}s^{-1}}$ fluid velocity in global coordinate system x-direction simulation.

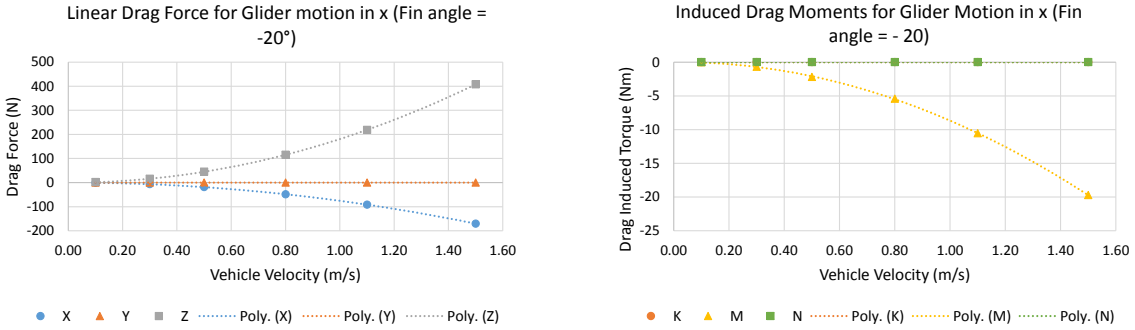

(a) Linear hydrodynamic force **(b)** Rotational hydrodynamic moment

Figure 3.7: Example of third order fitted polynomial for hydrodynamic force from velocity in the x-direction.

$$\begin{bmatrix} M_{ik} \\ M_{im} \\ M_{in} \end{bmatrix} = \begin{bmatrix} M_{bk} \\ M_{bm} \\ M_{bn} \end{bmatrix} \tag{3.16}$$

Finally the forces are treated as generalised forces in the system acting on the relevant body and the moments are treated as inertial, such that the hydrodynamic forces acting in the generalised coordinate domain are $Q_d(q, \dot{q})$. Thus the equations of motion for the rigid body system that includes buoyancy and hydrodynamic forces is given by Eq. 3.17.

$$\mathbf{M}_{RB}(q)\ddot{q} + \mathbf{C}_{RB}(q, \dot{q})\dot{q} + G(q) = \tau + Q_b(q) + Q_d(q, \dot{q}) \tag{3.17}$$

3.4.2 Added mass characterisation

Added mass is a representation of the pressure-induced forces on a body, which are proportional to the acceleration of the body as it moves through a medium [8]. As the added mass forces in water can be significant, an estimate of the added mass terms relating to the float and glider bodies are needed. Although advanced computational tools (e.g. WAMIT, WADAM) were not available to calculate these added mass terms, empirical methods can be used to provide an estimate for the added mass of the float and glider bodies.

The added mass for a single body can be represented using the SNAME representation of the added mass derivatives [9] shown in Eq. 3.18. The SNAME notation for body-fixed velocities, forces and moments will be used, such that the added mass force, Z, along the z-axis that is caused by the acceleration $\dot{v}$ in the y-direction can be written as in Eq. 3.19, where the force acts to oppose the acceleration.

$$M_A = -\begin{bmatrix} X_{\dot{u}} & X_{\dot{v}} & X_{\dot{w}} & X_{\dot{p}} & X_{\dot{q}} & X_{\dot{r}} \\ Y_{\dot{u}} & Y_{\dot{v}} & Y_{\dot{w}} & Y_{\dot{p}} & Y_{\dot{q}} & Y_{\dot{r}} \\ Z_{\dot{u}} & Z_{\dot{v}} & Z_{\dot{w}} & Z_{\dot{p}} & Z_{\dot{q}} & Z_{\dot{r}} \\ K_{\dot{u}} & K_{\dot{v}} & K_{\dot{w}} & K_{\dot{p}} & K_{\dot{q}} & K_{\dot{r}} \\ M_{\dot{u}} & M_{\dot{v}} & M_{\dot{w}} & M_{\dot{p}} & M_{\dot{q}} & M_{\dot{r}} \\ N_{\dot{u}} & N_{\dot{v}} & N_{\dot{w}} & N_{\dot{p}} & N_{\dot{q}} & N_{\dot{r}} \end{bmatrix} \tag{3.18}$$

$$Z = -Z_{\dot{v}}\dot{v} \qquad\qquad Z_{\dot{v}} = \frac{\partial Z}{\partial \dot{v}} \tag{3.19}$$

The resulting Coriolis and centripetal matrix for the added mass matrix presented in Eq. 3.18 is shown in Eq. 3.20 with the relevant substitutions given in Eq. 3.21

$$C_A(v) = -\begin{bmatrix} 0 & 0 & 0 & 0 & -a_3 & a_2 \\ 0 & 0 & 0 & a_3 & 0 & -a_1 \\ 0 & 0 & 0 & -a_2 & a_1 & 0 \\ 0 & -a_3 & a_2 & 0 & -b_3 & b_2 \\ a_3 & 0 & -a_1 & b_3 & 0 & -b_1 \\ -a_2 & a_1 & 0 & -b_2 & b_1 & 0 \end{bmatrix} \tag{3.20}$$

$$
\begin{aligned}
a_1 &= X_{\dot{u}}\dot{u} + X_{\dot{v}}\dot{v} + X_{\dot{w}}\dot{w} + X_{\dot{p}}\dot{p} + X_{\dot{q}}\dot{q} + X_{\dot{r}}\dot{r} \\
a_2 &= Y_{\dot{v}}\dot{v} + Y_{\dot{v}}\dot{v} + Y_{\dot{w}}\dot{w} + Y_{\dot{p}}\dot{p} + Y_{\dot{q}}\dot{q} + Y_{\dot{r}}\dot{r} \\
a_3 &= Z_{\dot{w}}\dot{w} + Z_{\dot{v}}\dot{v} + Z_{\dot{w}}\dot{w} + Z_{\dot{p}}\dot{p} + Z_{\dot{q}}\dot{q} + Z_{\dot{r}}\dot{r} \\
b_1 &= K_{\dot{p}}\dot{p} + K_{\dot{v}}\dot{v} + K_{\dot{w}}\dot{w} + K_{\dot{p}}\dot{p} + K_{\dot{q}}\dot{q} + K_{\dot{r}}\dot{r} \\
b_2 &= M_{\dot{q}}\dot{q} + M_{\dot{v}}\dot{v} + M_{\dot{w}}\dot{w} + M_{\dot{p}}\dot{p} + M_{\dot{q}}\dot{q} + M_{\dot{r}}\dot{r} \\
b_3 &= N_{\dot{r}}\dot{r} + N_{\dot{v}}\dot{v} + N_{\dot{w}}\dot{w} + N_{\dot{p}}\dot{p} + N_{\dot{q}}\dot{q} + N_{\dot{r}}\dot{r}
\end{aligned}
\tag{3.21}
$$

The assumption of three-axis symmetry was enforced for the calculation of the added mass terms. This symmetry assumption eliminates the need to calculate the off-diagonal added mass terms, which for most practical purposes are small compared to the diagonal added mass terms, $(X_{\dot{u}}, Y_{\dot{v}}, Z_{\dot{w}}, K_{\dot{p}}, M_{\dot{q}}, N_{\dot{r}})$ [8]. The symmetry assumption results in the added mass derivative matrix shown in Eq. 3.22, although reduces the accuracy of the calculation.

$$
M_A = -\begin{bmatrix}
X_{\dot{u}} & 0 & 0 & 0 & 0 & 0 \\
0 & Y_{\dot{v}} & 0 & 0 & 0 & 0 \\
0 & 0 & Z_{\dot{w}} & 0 & 0 & 0 \\
0 & 0 & 0 & K_{\dot{p}} & 0 & 0 \\
0 & 0 & 0 & 0 & M_{\dot{q}} & 0 \\
0 & 0 & 0 & 0 & 0 & N_{\dot{r}}
\end{bmatrix}
\tag{3.22}
$$

The resulting Coriolis and centripetal matrix for the reduced added mass matrix presented in Eq. 3.22 can be written in the same form as Eq. 3.20, where the substitutions will now take the form given in Eq. 3.23.

$$
\begin{aligned}
a_1 = X_{\dot{u}}\dot{u} \quad &\Rightarrow \quad X_{\dot{v}}, X_{\dot{w}}, X_{\dot{p}}, X_{\dot{q}}, X_{\dot{r}} = 0 \\
a_2 = Y_{\dot{v}}\dot{v} \quad &\Rightarrow \quad Y_{\dot{u}}, Y_{\dot{w}}, Y_{\dot{p}}, Y_{\dot{q}}, Y_{\dot{r}} = 0 \\
a_3 = Z_{\dot{w}}\dot{w} \quad &\Rightarrow \quad Z_{\dot{u}}, Z_{\dot{v}}, Z_{\dot{p}}, Z_{\dot{q}}, Z_{\dot{r}} = 0 \\
b_1 = K_{\dot{p}}\dot{p} \quad &\Rightarrow \quad K_{\dot{u}}, K_{\dot{v}}, K_{\dot{w}}, K_{\dot{q}}, K_{\dot{r}} = 0 \\
b_2 = M_{\dot{q}}\dot{q} \quad &\Rightarrow \quad M_{\dot{u}}, M_{\dot{v}}, M_{\dot{w}}, M_{\dot{p}}, M_{\dot{r}} = 0 \\
b_3 = N_{\dot{r}}\dot{r} \quad &\Rightarrow \quad N_{\dot{u}}, N_{\dot{v}}, N_{\dot{w}}, N_{\dot{p}}, N_{\dot{q}} = 0
\end{aligned}
\tag{3.23}
$$

Although this derivation gives insight to how added mass affects a single body given body-fixed velocities, the Lagrangian formation can be used to get the added mass in terms of generalised coordinates for the multi-body Wave Glider system. For each body a kinetic energy formation that is dependent on the velocity of the body in the inertial frame and the added mass component in each of the six directions of the body can be used, Eq. 3.24. Making use of this kinetic energy formation the mass and Coriolis and centripetal force matrices for the added mass can be calculated making use of Eq. 3.7 and 3.8.

$$
K_{addedmass} = \frac{1}{2}\left(X_{\dot{u}}v_x^2 + Y_{\dot{v}}v_y^2 + Z_{\dot{v}}v_z^2 + K_{\dot{v}}\dot{\phi}^2 + M_{\dot{v}}\dot{\theta}^2 + N_{\dot{v}}\dot{\psi}^2\right) \tag{3.24}
$$

For the estimation of the added mass components, several methods were used to capture the different scenarios for the float and glider. These methods were chosen as they could be used to best approximate the bodies of the float and glider from the empirical data available. The methods are listed in Table 3.3 and 3.4, for the float and the glider respectively, and each method will be briefly explained below. A useful result for slender bodies making use of strip theory is

also given. Strip theory is used where two dimensional cross-sectional shapes are analysed. As previously discussed in Section 2.6, strip theory makes the assumption that the effects on a 3D body can be represented by the sum of the effects on the 2D cross-sectional strips that compose the 3D body. The added mass derivatives of the 2D strips are defined as M_a as the derivative is that of an area and must be scaled by the appropriate length to represent the added mass of the body, while the methods that make use of 3D bodies have added mass derivatives M_v. It should be noted that as with the hydrodynamic force calculations, the density of water, ρ, was taken to be 1000 kg·m^{-3}.

Added mass methods for float

The methods for the calculation of the added mass components for the float are presented in Table 3.3. Method 1 is a two-dimensional strip characterisation of the added mass for a square cross-section where the ratio of the lengths is one, $\frac{a}{b} = 1$, the direction of motion is normal to the surface, the body is submerged to a depth b, and the added mass derivative per unit length is given by M_a. Method 2 is a similar two-dimensional characterisation as in method 1 however, the direction of motion is parallel to the surface. Method 3 approximates the hull of a submerged vessel as a half cylinder with a draft, D, taken as the cylinder radius, for motion parallel to the surface, with the added mass derivative given by M_v.

Added mass methods for glider

The methods for the calculation of the added mass components for the glider are presented in Table 3.4. Method 1 is the two-dimensional strip characterisation for vertical motion with respect to the lengths of a submerged cross-section with lengths $2a$ and $2b$. The ratio of a to b gives the coefficient used for the calculation of the added mass. The added mass derivative per unit length is given by M_a. Method 2 characterises the added mass for vertical motion of a submerged three-dimensional parallelepiped with respect to the square face with length a and the height b. The added mass coefficient is dependent on the ratio $\frac{b}{a}$ and the added mass derivative is given by M_v. Method 3 characterises the added mass for vertical motion of a rectangular plate. The added mass coefficient is dependent on the ratio $\frac{b}{a}$ and the added mass derivative is given by M_v. Method 4 gives the added mass coefficient for a plane lamina rotating about its central axis. The added mass derivative per unit length is given by M_a.

For a slender body the rotational added mass components can be related to the linear added mass components. The relationship between the rotational added mass about the x-axis for motion about the x-axis, $K_{\dot{p}}$, and the linear added mass components along the y-axis, $Y_{\dot{v}}$, and z-axis, $Z_{\dot{w}}$, for motion along their respective directions is defined in Eq. 3.25 [31], where L is the length of the body along the x-axis, B is the breadth of the body along the y-axis, and H is the height of the body along the z-axis. Although a slender body is characterised by a length much larger that its width, which is not exactly the case in this application, the result is still useful to get an approximation of the rotational added mass.

$$K_{\dot{p}} = \int_{-L/2}^{L/2} K_{\dot{p}}^{(2D)} \triangleq \int_{-B/2}^{B/2} y^2 Z_{\dot{w}}^{(2D)} dy + \int_{-H/2}^{H/2} z^2 Y_{\dot{v}}^{(2D)} dz \tag{3.25}$$

Table 3.3: Added mass methods for float. Adapted from [8, 30].

Method	
1	Vertical (normal to surface) 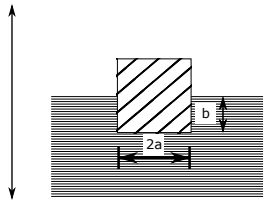 $a/b = 1 \quad M_a = 0.75\pi\rho a^2$
2	Horizontal (parallel to surface) 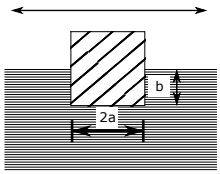 $a/b = 1 \qquad M_a = 0.25\pi\rho a^2$
3	Horizontal (parallel to surface) 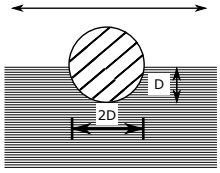 $M_v = \frac{1}{2}\rho\pi D^2 L$

Table 3.4: Added mass methods for glider. Adapted from [25, 30].

Method	Diagram	Direction of motion	Ratios		Coefficient	Added mass derivative
			a/b	b/a	k	
1	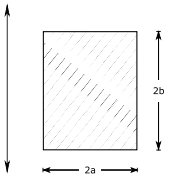	Vertical	inf		1	$M_a = k\pi\rho a^2$
			10		1.14	
			5		1.21	
			2		1.36	
			1		1.51	
			1/2		1.70	
			1/5		1.98	
			1/10		2.23	
2	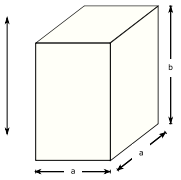	Vertical		1	2.32	$M_v = k\rho a^2 b$
				2	0.86	
				3	0.62	
				4	0.47	
				5	0.37	
				6	0.29	
				7	0.22	
				10	0.1	
3	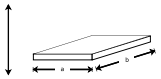	Vertical		1	0.478	$M_v = k\pi\rho\frac{a^2}{4}b$
				1.5	0.680	
				2	0.840	
				2.5	0.953	
				3	1	
				3.5	1	
				4	1	
				inf	1	
4	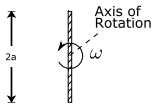	Rotation about central axis			$\frac{1}{8}$	$M_a = k\pi\rho a^4$

Where Eq. 3.25 can be simplified to Eq. 3.26:

$$K_{\dot{p}} = \frac{1}{12}\left(Z_{\dot{w}}^{(2D)} B^3 + Y_{\dot{v}}^{(2D)} H^3\right), \tag{3.26}$$

with the rotational added mass derivatives about the y-axis, $M_{\dot{q}}$, and z-axis, $N_{\dot{r}}$, for motion in their respective directions given in Eq. 3.27 and 3.28, respectively.

$$M_{\dot{q}} = \frac{1}{12}\left(Z_{\dot{w}}^{(2D)} L^3 + X_{\dot{u}}^{(2D)} H^3\right) \tag{3.27}$$

$$N_{\dot{r}} = \frac{1}{12}\left(X_{\dot{u}}^{(2D)} B^3 + Y_{\dot{v}}^{(2D)} L^3\right) \tag{3.28}$$

Since the added mass was characterised for the float and glider bodies separately in their respective body frames, there is a necessary transform to allow application to the 12 degree of freedom Lagrangian system. The treatment of the float added mass will be explained first followed by that of the glider.

Because of the DH-parametrisation of the system the application of the float added mass is relatively trivial as the linear added mass terms need only to be rotated from the body frame into the inertial frame. The added mass matrix for the float is presented in Eq. 3.29, where the float body-frame has the same orientation as the inertial frame, m_{afx} is the added mass component in the inertial x-direction and for the float, and J_{afx} is the rotational added mass component about the float x-axis.

$$\mathbf{M}_{Af} = diag[m_{afx}, m_{afy}, m_{afz}, J_{afx}, J_{afy}, J_{afz}, 0, 0, 0, 0, 0, 0] \tag{3.29}$$

The treatment of the glider added mass is slightly more complex because of the dependency on the attitude of the float, the tether fixation position on both the float and the glider, the attitude of the tether, and the attitude of the glider. Similarly to the float added mass, the linear glider added mass components must be transformed from the body frame into the inertial frame. A simplified version of the glider added mass matrix is presented in Eq. 3.30, where the attitude of the float, the attitude of the tether, and the attitude of the glider were assumed to be in the initial state shown in Fig. 3.1, i.e. $[\phi_f, \theta_f, \psi_f, \phi_t, \theta_t, \phi_g, \theta_g, \psi_g] = 0$, m_{agx} is the added mass component for the glider in the inertial x-direction, and J_{agx} is the rotational added mass component about the glider x-axis.

$$M_{Ag} = \begin{bmatrix}
m_{agx} & 0 & 0 & -4.21m_{agx} & 4m_{agx} & 0 & 4.11m_{agx} & 0 & 0.11m_{agx} & 0 & 0 & 0 \\
0 & m_{agy} & 0 & -4m_{agy} & -4.11m_{agy} & 0 & 0 & 4.11m_{agy} & 0 & 0.11m_{agy} & 0 & 0 \\
0 & 0 & m_{agz} & 0 & 0 & 0 & 0 & 0 & 0 & 0 & 0 & 0 \\
-4.21m_{agx} & -4m_{agy} & 0 & 17.72m_{agx}{+}16m_{agy} & 16.42m_{agy}{-}16.84m_{agx} & 0 & -17.28m_{agx} & -16.42m_{agy} & 0 & -0.42m_{agy} & 0 & 0 \\
4m_{agx} & -4.11m_{agy} & 0 & 16.42m_{agy}{-}16.84m_{agx} & 16m_{agx}{+}16.85m_{agy} & 0 & 4.11m_{agx} & -16.85m_{agy} & 0 & -0.43m_{agy} & 0 & 0 \\
0 & 0 & 0 & 0 & 0 & 0 & 0 & 0 & 0 & 0 & 0 & 0 \\
4.11m_{agx} & 0 & 0 & -17.28m_{agx} & 16.42m_{agx} & 0 & 16.85m_{agx} & 0 & 0 & 0 & 0 & 0 \\
0 & 4.11m_{agy} & 0 & -16.42m_{agy} & -16.84m_{agy} & 0 & 0 & 16.84m_{agy} & 0 & 0.43m_{agy} & 0 & 0 \\
0 & 0 & 0 & 0 & 0 & 0 & 0 & & 0J_{agx} & 0 & 0 & 0 \\
0 & 0.11m_{agy} & 0 & -0.42m_{agy} & -0.43m_{agy} & 0 & 0 & 0.43m_{agy} & 0 & J_{agy}{+}0.01m_{agy} & 0 & 0 \\
0 & 0 & 0 & 0 & 0 & 0 & 0 & 0 & 0 & 0 & J_{agz} & 0 \\
0 & 0 & 0 & 0 & 0 & 0 & 0 & 0 & 0 & 0 & 0 & 0
\end{bmatrix} \tag{3.30}$$

As Eq. 3.29 and Eq. 3.30 represent the added mass contributions of the float and the glider in the inertial frame, respectively, they can be summed to provide the complete added mass matrix, $\mathbf{M}_A(q)$. The added mass Coriolis and centripetal matrix, $\mathbf{C}_A(q, \dot{q})$, can be calculated

from the added mass matrix making use of Eq. 3.8, which given a mass matrix in terms of generalised coordinates will calculate the associated Coriolis and centripetal force matrix. Thus the equation of motion for the rigid-body model that includes buoyancy, hydrodynamic forces and added mass is presented in Eq. 3.31.

$$(\mathbf{M}_{RB}(q) + \mathbf{M}_A(q))\ddot{q} + (\mathbf{C}_{RB}(q,\dot{q}) + \mathbf{C}_A(q,\dot{q}))\dot{q} + G(q) = \tau + Q_b(q) + Q_d(q,\dot{q}) \tag{3.31}$$

3.5 Rudder modelling

As the only controllable input to the system, the modelling of the rudder effects is crucial. Flow simulations were again used to determine the hydrodynamic forces acting on the glider body because of the rudder. The forces and moments in the body-fixed axis of the glider through the glider centre of mass were set as global goals. The rudder simulations were run for the range of rudder angles, $[0°, 5°, 10°, 20°, 30°, 40°, 50°]$, and for flow velocities in the body-fixed glider x-axis of $[0.1, 0.3, 0.5, 0.8, 1.1, 1.5]$ m·s^{-1}. The effects of the zero degree simulations were subtracted from that of the other angles to remove any effects of the glider body. The observation was made that the glider response to the rudder input is symmetric, and this reduces the required number of simulations. The reduced model of the glider that did not include the hydrofoil fins was used in the rudder simulations, shown in Fig. 3.8. When implementing the rudder forces onto the Wave Glider system, the linear components of the rudder force needed to be rotated into the inertial frame as the rudder forces were calculated in the glider body frame. Following this the rudder forces could be treated as generalised forces and the moments could be treated as inertial, such that the hydrodynamic forces acting on the glider due to the rudder in the inertial frame are $Q_r(q,\dot{q})$. The equation of motion for the Wave Glider system that included the rudder forces, is shown in Eq. 3.32.

$$(\mathbf{M}_{RB}(q) + \mathbf{M}_A(q))\ddot{q} + (\mathbf{C}_{RB}(q,\dot{q}) + \mathbf{C}_A(q,\dot{q}))\dot{q} + G(q) = \tau + Q_b(q) + Q_d(q,\dot{q}) + Q_r(q,\dot{q}) \tag{3.32}$$

3.6 Hydrofoil - simplification and modelling

The hydrofoils that generate the wave-driven propulsion force make up a complex mechanical system. The hydrofoils are hinged near the leading edge, with mechanical stops allowing for a

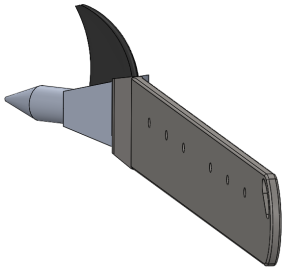

Figure 3.8: Glider model for flow simulations used in rudder modelling. The fins were removed for the simulations and the deflection angle of the rudder was varied.

limited range of motion. The limits of the rotational range of motion are $-20°$ and $40°$ about the body-fixed y-axis of the glider where the frame follows the NED convention. A restorative spring is connected to each hydrofoil. A schematic of the system is shown in Fig. 3.9.

Initially the system was simplified to a quasi-steady state system meaning that the hydrofoils would instantaneously assume the maximum angle of $-20°$ when the glider had a positive body-fixed z velocity and $40°$ when the glider had a negative body-fixed z velocity. This assumption was made as the transient period between these states would be suitably short and thus the effect of these transient states would be small. Another reason for this simplification to a quasi-steady state was to avoid the non-Lipschitz condition when considering the instantaneous force that a mechanical stop requires. Similarly the constraint force could be modelled making use of constrained modelling techniques within Lagrangian modelling, however for a system with 12 degrees of freedom the inversion of the mass matrix to solve for the constraints would require more computational power than available. As such the hydrofoil angle was not used as a generalised coordinate and rather determined by the motion of the glider. The hydrodynamic modelling of the hydrofoils was included in the hydrodynamics of the glider.

To increase the fidelity of the model and attempt to capture the wave-propulsion mechanism better it was decided that the hydrofoil angle should be treated as a generalised coordinate and be determined based on the dynamics of the entire system. This was resolved by extending the functionality of the spring shown in Fig. 3.9 to have a variable spring constant which increased exponentially as the hydrofoil angle increased past the limiting angles.

To this end, the hydrodynamic forces on the hydrofoils were modelled separately to that of the glider. CFD analysis making use of SolidWorks Flow Simulator was again used to characterise the forces and moments acting on the hydrofoils for a set of hydrofoil angles, $[-20, -10, 0, 10, 20, 30, 40]$ degrees, for 4 different flow velocities, $[0.1, 0.5, 1, 1.5]$ $\mathrm{m{\cdot}s^{-1}}$ per direction. A similar assumption to the overall glider hydrodynamic modelling was made where for the x-direction motion only the positive glider motion had to be considered. The modelling of a single pair of hydrofoils would be sufficient to characterise the hydrodynamic forces applied to the six pairs by applying a suitable scaling factor as this would decrease the computation domain and hence the solution time. Furthermore because of the shape of the hydrofoils, the effects due to motion in the glider body-fixed y-direction are negligible and thus only the velocities in the glider body-fixed x- and z-directions and pitching of the hydrofoil were considered. The hydrodynamic forces in these directions replaced the forces for the glider in the appropriate directions as the hydrofoils will account for the vast majority of the hydrodynamic effects.

3.7 Current inclusion

Sea currents can have an impact on the operation of the Wave Glider, but as this interaction is not a focus of this dissertation, there is only a brief investigation into how to include sea currents. The inclusion of current would take inspiration from the modelling proposed by Fossen [8], where the seakeeping frame has velocities relative to the sea state and currents, v_r, and the model velocities are relative to the inertial plane, v. This allows certain effects on the model to be dependent on the relative velocity to the currents while the rigid body motion could still be relative to the inertial frame.

The effects that are relative to the sea frame are the hydrodynamic forces and added mass effects. The equation of motion for the model that includes currents is shown in Eq. 3.33, where $\dot{q}_r$ represents the generalised velocity vector and $\ddot{q}_r$ represents the generalised acceleration vector, relative to the seakeeping frame. Such that the hydrodynamic forces will be dependent on the

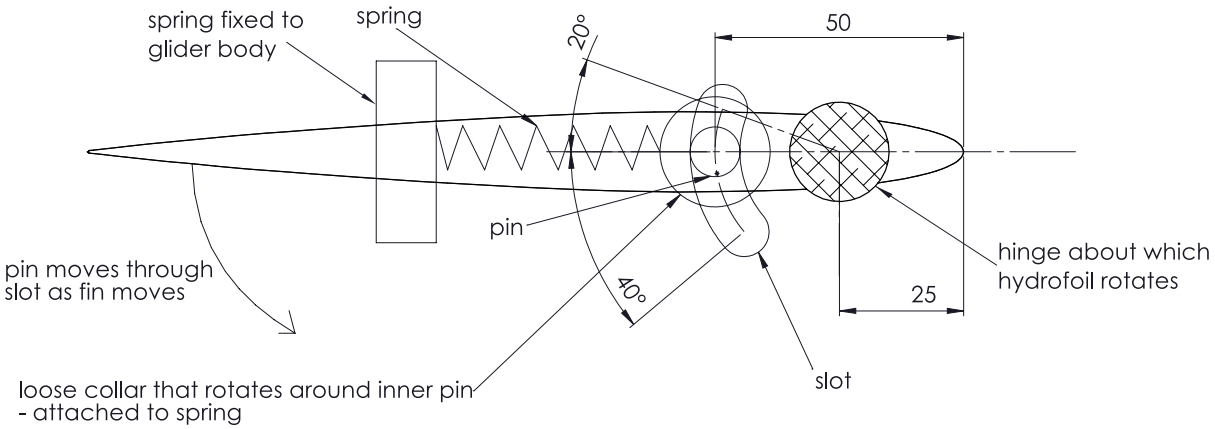

Figure 3.9: Schematic of hydrofoil mechanical mechanism with glider body-fixed y-axis coming out of the page. The schematic was generated based on the SolidWorks model that was made of the Wave Glider. The hydrofoil is hinged to the glider near the leading edge, with the pin on the hydrofoil moving within a slot on the glider to restrict the hydrofoil angle. A restorative spring is attached to the pin on the hydrofoil by a loose collar and rigidly to the glider.

velocities and accelerations relative to the seakeeping frame.

$$\mathbf{M}_{RB}(q)\ddot{q}+\mathbf{C}_{RB}(q,\dot{q})\dot{q}+G(q)+\mathbf{M}_{A}(q)\ddot{q}_{r}+C_{A}(q,\dot{q}_{r})\dot{q}_{r}=\tau+Q_{b}(q)+Q_{d}(q,\dot{q}_{r})+Q_{r}(q,\dot{q}_{r}) \quad (3.33)$$

3.8 Summary

This concludes the presentation of the modelling techniques used in the generation of the Wave Glider model. The referencing frames and Lagrangian equations of motion for the twelve DOF model were presented. The methodology for the calculation of the buoyancy force, the hydrodynamic forces, and the added mass was explained; such that the generated model would include rigid-body motion, restorative forces, and hydrodynamic forces, drag and added mass, and will have sufficient fidelity for dynamic analysis.

Chapter 4

Control design approach and architecture

The control design for this dissertation required generating a stable controller for the heading direction of the glider, which is controlled by the rudder. The system has a single output (heading direction of the glider) and a single input (rudder angle), however the response also depends on the glider velocity, which itself is dependent on the sea state. This chapter formulates the design approach for the control implementation presented in Chapter 6.

Control theory covers a wide range of different approaches that allow for powerful mathematical techniques to be used to provide engineering solutions to practical problems. These approaches can typically be separated depending on whether the control design is conducted in the time or frequency domain. Typical types of control methods are: adaptive, optimal, robust, and intelligent control. Adaptive control involves the automated adjustment of controller gains dependent on the real-time parameters of a system, monitored using a sensors. Optimal control focuses on the optimization of a cost function such that certain optimality criteria are met. Robust control designs controllers such that a certain level of performance is ensured provided that uncertain parameters are within a defined set. Intelligent control is a branch of control design that makes use of artificial intelligence methods such as fuzzy logic, machine learning, and Bayesian probability for control. These control methods have well-defined algorithms associated with them to allow for methodical design approaches; some common control algorithms are: pole placement, model predictive control (MPC), quantitative feedback control (QFT), and H_∞.

For this single-input single-output (SISO) system a cascaded design approach allows for a simple and well-defined control structure that is well documented, and QFT methods provide robust control where uncertainty, such as the glider velocity, is present. The cascaded design approach requires an inner controller, designed for glider yaw rate control, and an outer controller, designed for glider yaw orientation control. A top-down view of the control scheme is shown in Fig. 4.1, where for a given glider yaw set point the Glider Yaw Orientation Controller determines a desired glider yaw rate based on feedback from the model; this yaw rate feeds into the Glider Yaw Rate Controller to determine the necessary rudder angle which is then fed into the model. Both the controllers must take saturation effects into account to eliminate wind-up and thus ensure reliable control. The controllers must also have zero steady state error. The bottom-up view of this control scheme is given in Fig. 4.2.

To eliminate integrator wind-up the controllers must enter and exit a variable saturation condition properly. Integrator wind-up occurs when the integral terms of a controller accumulate

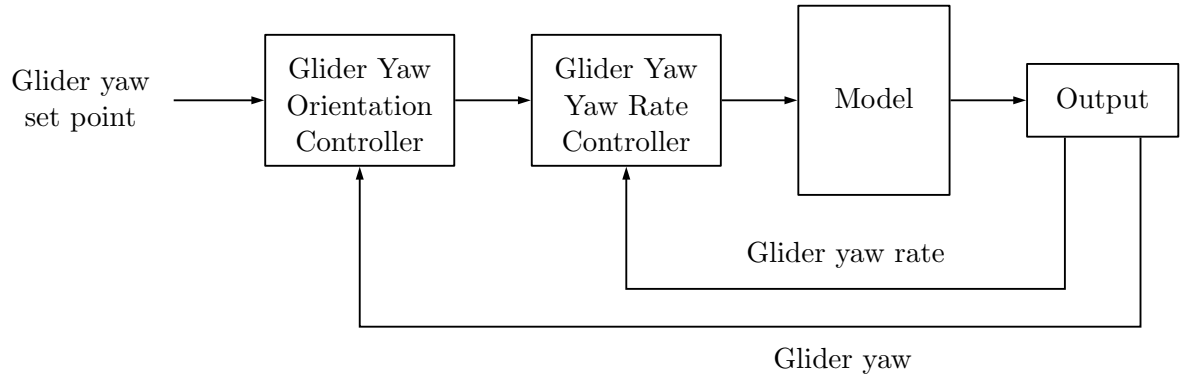

Figure 4.1: Top down control design

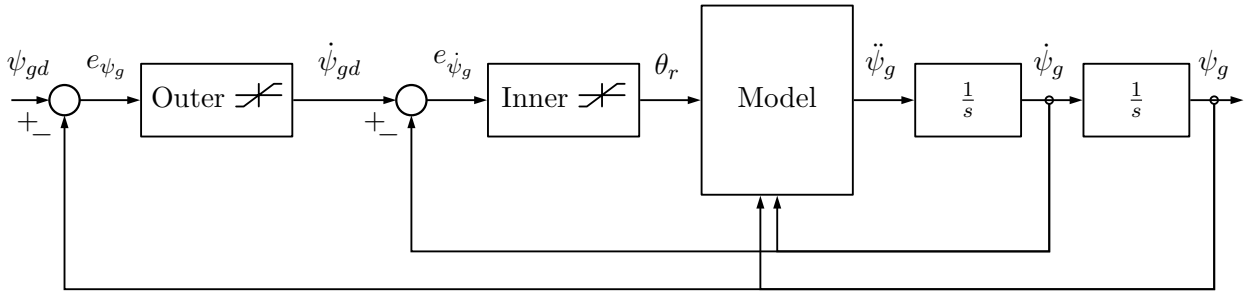

Figure 4.2: Bottom up control design

a significant error, such as after the output of the controller saturates. Two differing saturation schemes are explained below for scenarios that either allow for or do not allow for separable integrators. The first, shown in Fig. 4.3, involves initialising the integrator to a desired value when saturation occurs while the second, shown in Fig. 4.4, makes use of positive feedback [32].

For a strictly proper controller, where the degree of the numerator of the transfer function is less than the degree of the denominator, the integrator can be treated separately. The saturation condition can be used to initialise the integrator to a desired value, Fig. 4.3. The output of the integrator for a given signal is compared to a given upper and lower saturation limit making use of the state output of the integrator. If the output is greater than the upper limit or less than the lower limit, the integrator is reset to a desired value making use of the initial condition input. The desired value for the integrator block is set by feeding the state output of the integrator into a dynamic saturation block along with the upper and lower saturation limits. For an output within the saturation limits, the integrator is not reset and acts normally. When the output reaches the saturation limit the integrator is held at the saturation limit until the output of the integrator falls within the saturation limits.

For a proper controller, where the degree of the numerator of the transfer function is not more than the degree of the denominator, the integrator cannot be treated separately and must be accompanied by a zero. A positive feedback scheme can be used, as shown in Fig. 4.4, where T is defined by a necessary zero in the transfer function. When the output, Out, is within the saturation limits, the transfer function is shown in Eq. 4.2 making use of block diagram algebra, where the r is the input Signal, u is the input to the Dynamic Saturation, and y is the output Out. When the output saturates, it is held at the saturation limit by the Dynamic Saturation block until the input, Signal, pulls the output back within the saturation limits at which point normal unsaturated operation continues.

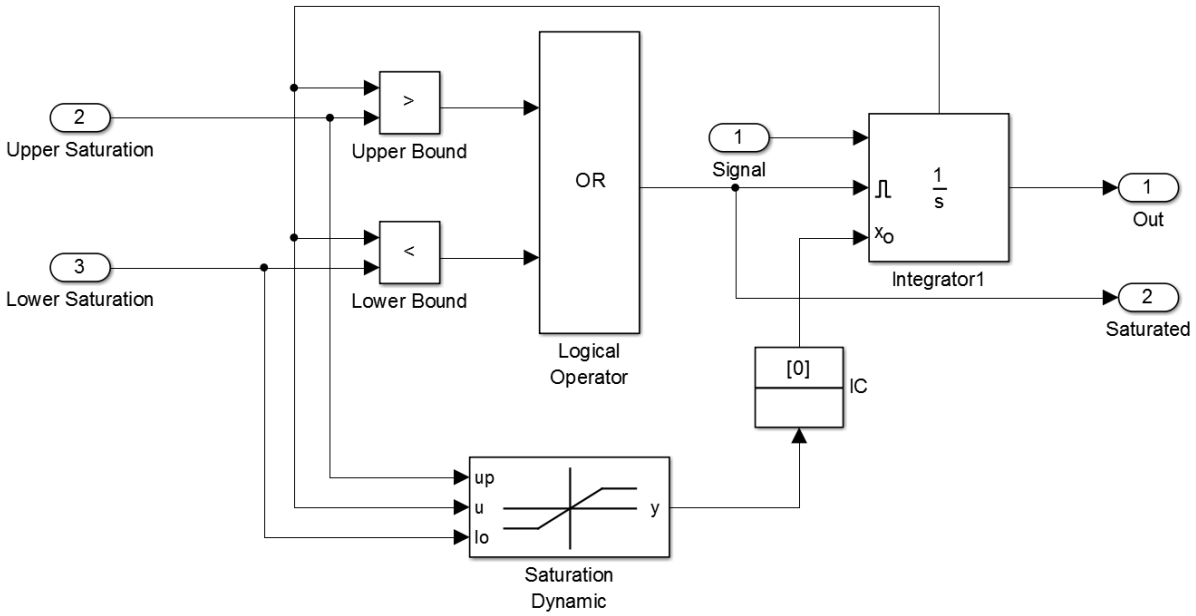

Figure 4.3: Schematic for single integrator with variable saturation. The output of the integrator is constantly compared to the saturation limits that are taken as inputs. If the integrated signal reaches one of the limit, the integrator is reset to hold the saturation limit until the integrated signal returns to within the saturation limits.

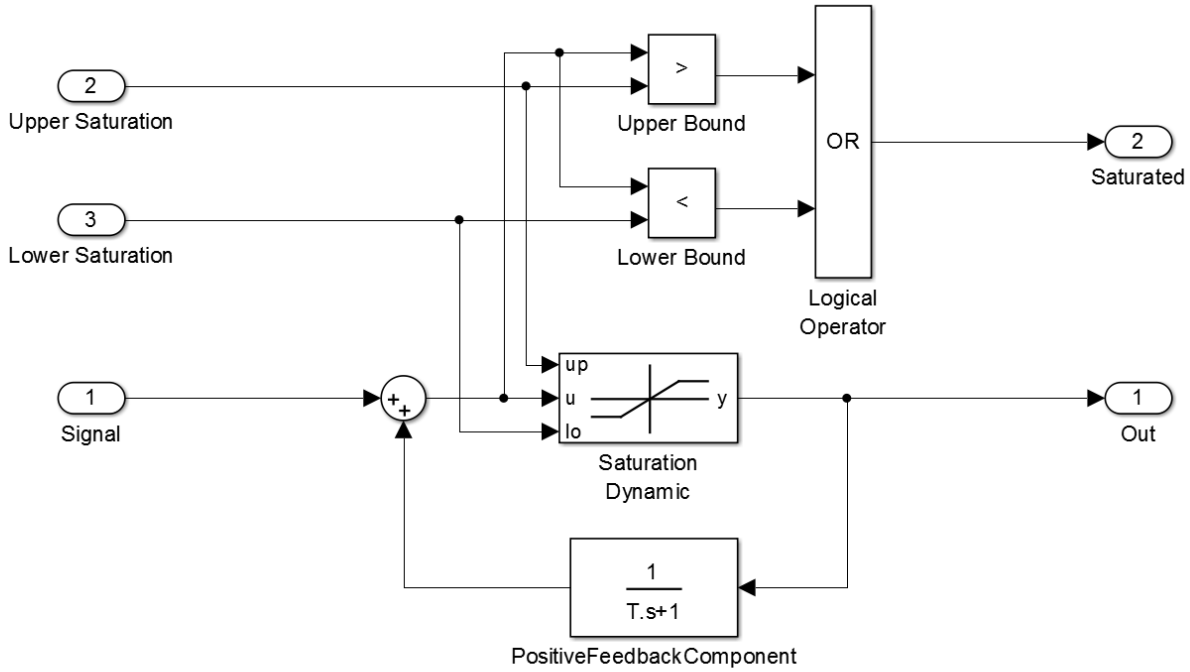

Figure 4.4: Schematic for Shinskey integrator [32]. The positive feedback loop takes the form of Eq. 4.2 during normal operation. When the signal, u, reaches the saturation limit, it is bounded by the dynamic saturation block. The signal remains saturated until the output of the dynamic saturation blocks returns to within the saturation limits.

$$\begin{aligned} y &= u \\ &= r + y\frac{1}{sT+1} \end{aligned} \tag{4.1}$$

$$\begin{aligned} \frac{y}{r} &= \frac{1}{1-\frac{1}{sT+1}} \\ &= \frac{sT+1}{sT} \end{aligned} \tag{4.2}$$

The glider yaw rate response is expected to have a non-linear nature due to the dependence on the rudder angle and the glider velocity, as such it is necessary to develop a reasonable estimate of the glider yaw rate response when determining the yaw rate plant. Thus the system was simplified to have no sea state input and for the glider to travel at a constant velocity in the glider body-fixed x-direction, v_{gbx}. For this section the glider velocity is only the glider body-fixed x-direction velocity as this component has the greatest effect on the yaw response.

Although the steady-state yaw rate for the glider for a constant rudder angle could be expected to be constant, characterised by a gain with a higher-frequency pole, this steady state would rarely be achieved due to the varying velocity of the glider according to the sea state input. As such it was decided that the transient behaviour of the yaw rate response would be characterised for the yaw rate plant ,which would be expected to take the form of a kinematic integrator from yaw acceleration (induced by force from the rudder angle) to yaw rate (i.e. ignoring the effect of the yaw rate on the velocity vector) with a specified gain. The gain is calculated from the simplified Wave Glider model for specific glider velocities and rudder angle inputs, where the gradient of the yaw rate after the defined rudder angle input could be measured and defines the gain. This gain will be proportional to the rudder angle and to the square of the glider velocity. The gain was determined for 6 glider velocities, $[0.23, 0.345, 0.88, 1.2, 1.35, 1.5]$ $\text{m}\cdot\text{s}^{-1}$, with each velocity being tested for 7 rudder angles, $[0°, 5°, 10°, 15°, 30°, 40°, 50°]$, as this adequately covered the range of expected velocities and allowed rudder angles. As the yaw rate plant gain is proportional to the square of the glider velocity, it can be seen that the rudder will have little to no effectiveness at low glider velocities as it provides little torque, as such it is assumed that the propeller will be used for orientation at low velocities. The response is assumed to be symmetric for the rudder angles.

Thus the glider yaw rate control scheme is given by Fig. 4.5, where the Yaw Rate Model determines the gain based on the input rudder angle and glider velocity and includes the integrator for the modelled response. The yaw rate controller initially took the form of a PI controller, as this is a fairly standard controller when considering cascaded control schemes, and was supplemented with an additional low pass filter component. It can be seen for this controller that the single integrator can be treated separately, with the form shown in Fig. 4.3, and has a saturation based on the glider velocity. The glider velocity has a saturation limit which forces it to be non-zero, and the glider velocity is always considered positive due to the propulsion mechanism, allowing for the controller output, $\theta_r v^2$, to be scaled appropriately based on the glider velocity. The saturation of the glider velocity has minimal affect on the response as the gain of the Yaw Rate Model will tend to zero as the square of the glider velocity tends to zero and thus a suitably small lower bound can be used.

Once a suitable controller is designed, the glider yaw rate control scheme can be expected to take the form of a first order low pass filter response with a gain of 1 and a variable time constant depending on the glider velocity, as the input to the glider yaw rate controller is a desired glider yaw rate and the output of the model is the glider yaw rate. Thus a first order low pass filter

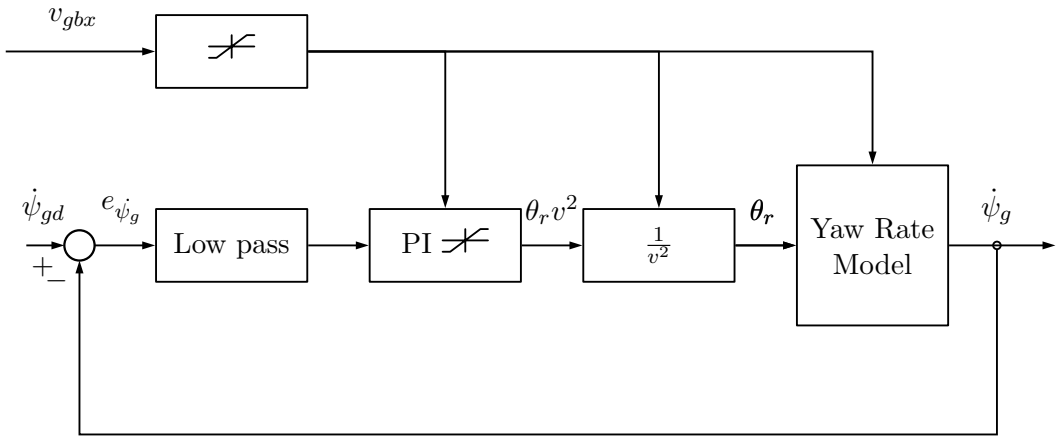

Figure 4.5: Glider yaw rate control scheme. For a given desired glider yaw rate, $\dot{\psi}_{gd}$, the error signal is passed into the glider yaw rate controller. The saturation limits for the glider yaw rate controller are determined based on the glider velocity. The output from the glider yaw rate controller is scaled by the glider velocity before the rudder command is passed into the yaw rate model.

with a variable time constant and an integrator can be used as the plant model for the glider yaw orientation and a suitable controller can be designed. The glider yaw orientation scheme will take the form of Fig. 4.6, initially taking the form of a PI controller, and supplemented by a lead controller to ensure appropriate dynamics. The PI block takes the form of the Shinskey integrator shown in Fig. 4.4.

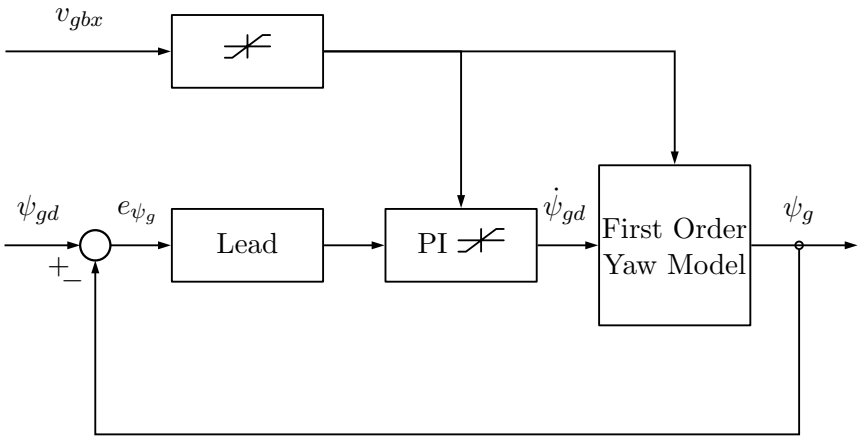

Figure 4.6: First order yaw control scheme. For a desired glider yaw, ψ_{gd}, the error signal is passed into the glider yaw controller. The saturation limits of the glider yaw controller are determined by the glider velocity. The output of the glider yaw controller is a desired yaw rate, $\dot{\psi}_{gd}$, which is fed into the first order yaw model.

Once a controller is designed for the First Order Yaw Model, this controller and the glider yaw rate controller can be implemented for the Yaw Rate Model to verify the first order assumption and performance, shown in Fig. 4.7, and following this can be implemented on the model of the system.

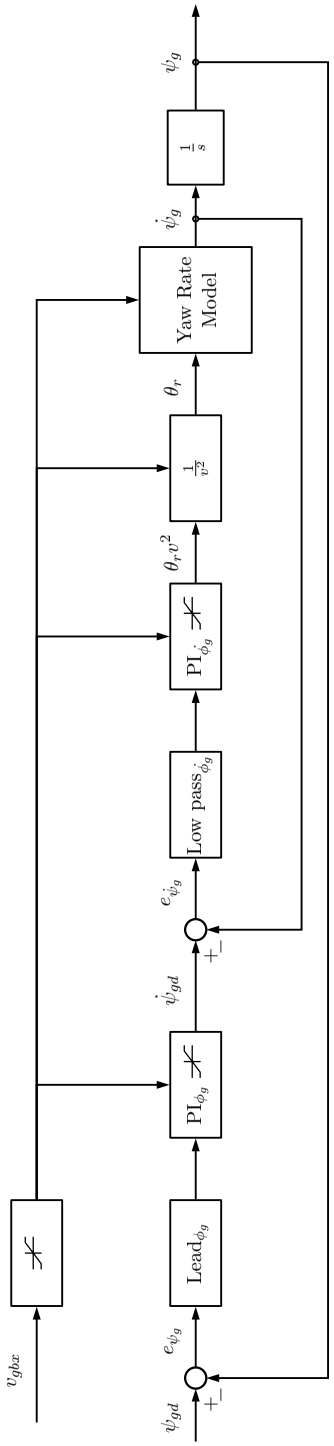

Figure 4.7: Glider yaw cascaded control scheme. The error between the desired glider yaw, ψ_{gd}, and the glider yaw, ψ_g, is fed into a glider yaw controller to determine the desired glider yaw rate, $\dot{\psi}_{gd}$. From the desired glider yaw rate, the error is fed into a glider yaw rate controller and scaled based on the glider velocity to determine the necessary rudder angle. The designed control accommodates the effects of a sea state which leads to variable glider velocities by allowing for variable saturation limits.

Chapter 5

Model characterisation and validation

The results presented in this chapter are based on the Wave Glider model described in Chapter 3, where the code for the Wave Glider model is presented in Appendix A. The Wave Glider model was simulated in MATLAB R2013a, making use of a combination of Simulink and MATLAB functions. For each simulation a specified sea state was generated. This chapter will first cover the results from the flow simulations for the hydrodynamic forces, followed by the added mass calculations. The system model was then validated by comparing the system response for the rigid-body model to the added effects of drag, added mass and to both these effects simultaneously.

MATLAB was used to generate surface fits where there was more than one input variable while Excel 2016 was used for the polynomial fits that were limited to a single input variable. The coefficient of determination, R^2, was used as a measure of the goodness of fit, and can be interpreted as the proportion of the variance of a dependent variable that can be predicted by an independent variable. The flow simulations were conducted in SolidWorks 2015 and were performed on a quad-core i5-3570 running at 3.4 GHz.

5.1 Hydrodynamic force results

The hydrodynamic force results for the float, the glider, the rudder, and the hydrofoils are presented below and follow the methodology listed in Subsection 3.4.1. The results for each body will be accompanied by a brief explanation. Third order polynomials were used for the float and glider hydrodynamic forces such that where both directions of motions were tested, the possible anti-symmetric forces and moments would be captured. The polynomial coefficient for all the hydrodynamic force results are listed in Appendix B.

The results for the flow simulations for the float are shown in Fig. 5.1 – 5.6. It can be seen that for each of the directional simulations there is a significant force or moment that opposes the direction of motion for the float. It can also be seen that there are forces and moments, which arise from the geometry of the float, that are significant but are not in the direction of motion; one such moment is the induced yaw moment, N, from motion in the y-direction which will be necessary to allow the float to be orientated in the same direction as the glider. And finally it can be seen that there are forces and moments that are not in the direction of motion and are insignificantly small such that they can be ignored that arise from the symmetry of the float;

an example of is the force Y for motion in the x-direction.

The coefficients of determination for the third order polynomial fitted curves for the hydrodynamic forces on the float are presented in Table 5.1. The coefficients are generally over 0.9, which indicates that the polynomials fitted to the hydrodynamic forces reasonably represent the data. The smallest coefficient is for the hydrodynamic moment N for pitching motion, θ, at 0.88. The coefficient for the pitching moment may indicate that the curve does not accurately represent the flow simulation data. The magnitude of the corresponding induced torque must also be taken into account and this component of the response is small, so the induced torque will have minimal impact.

Table 5.1: Coefficients of determination, R^2, for third order polynomial fitted curves for hydrodynamic forces on float. The polynomial curves for the float hydrodynamic forces are shown in Fig. 5.1 – 5.6.

Direction of float motion	Coefficient of determination for induced drag					
	X	Y	Z	K	M	N
x	1.00	0.90	1.00	1.00	1.00	0.98
y	1.00	1.00	1.00	1.00	1.00	1.00
z	1.00	1.00	1.00	1.00	1.00	1.00
ϕ	0.91	0.93	0.92	0.93	0.92	0.95
θ	1.00	0.95	1.00	0.96	1.00	**0.88**
ψ	1.00	1.00	1.00	0.97	0.89	1.00

The results from the flow simulation for the glider are shown in Fig. 5.7 – 5.14. Similarly to the float, it can be seen that there is a significant force or moment that opposes the direction of motion of the glider. It can also be seen that there are significant forces and moments that are not in the direction of motion; the propulsive force, X, from motion in the z-direction is one such force. There are also forces and moments that are not in the direction of motion that are suitably small and can be ignored.

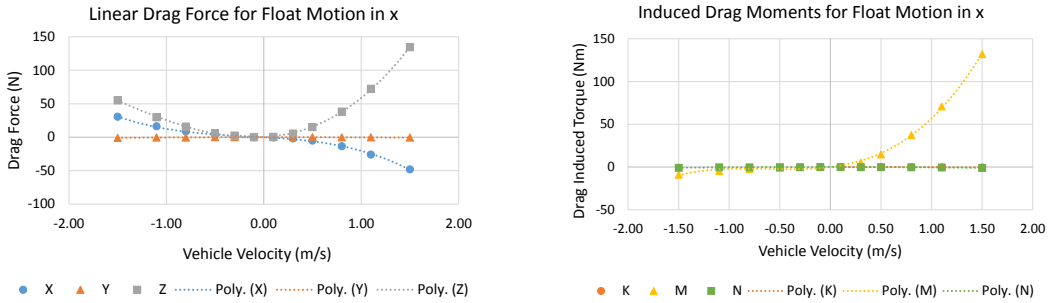

(a) Linear hydrodynamic force **(b)** Rotational hydrodynamic moment

Figure 5.1: Third order polynomial fitted curves for float velocity in the x-direction. Markers show measurements from flow simulations while dotted lines show polynomial fitted curves.

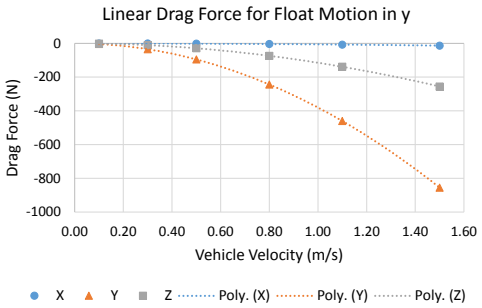

(a) Linear hydrodynamic force

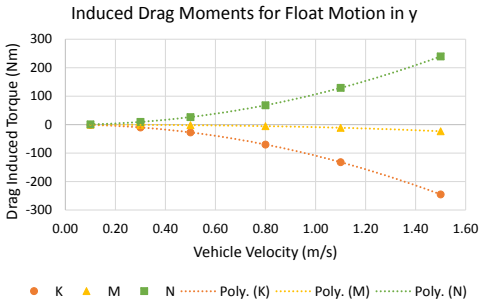

(b) Rotational hydrodynamic moment

Figure 5.2: Third order polynomial fitted curves for float velocity in the y-direction. Markers show measurements from flow simulations while dotted lines show polynomial fitted curves.

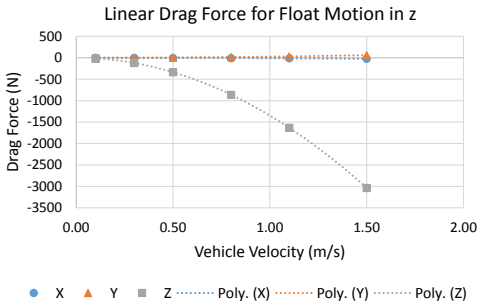

(a) Linear hydrodynamic force

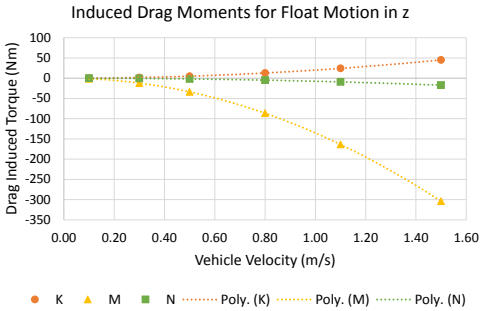

(b) Rotational hydrodynamic moment

Figure 5.3: Third order polynomial fitted curves for float velocity in the z-direction. Markers show measurements from flow simulations while dotted lines show polynomial fitted curves.

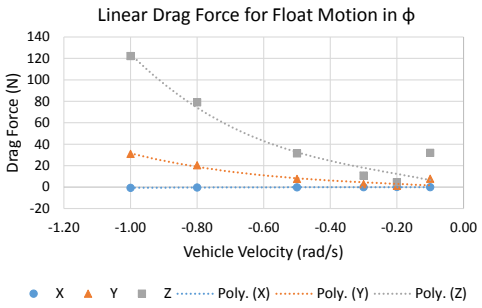

(a) Linear hydrodynamic force

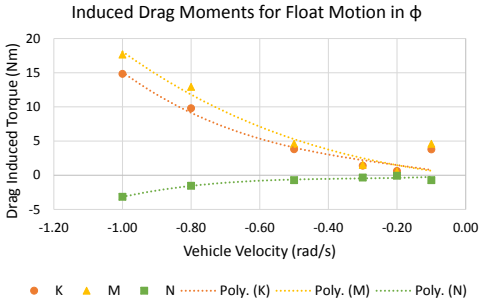

(b) Rotational hydrodynamic moment

Figure 5.4: Third order polynomial fitted curves for float roll about the x-axis. Markers show measurements from flow simulations while dotted lines show polynomial fitted curves.

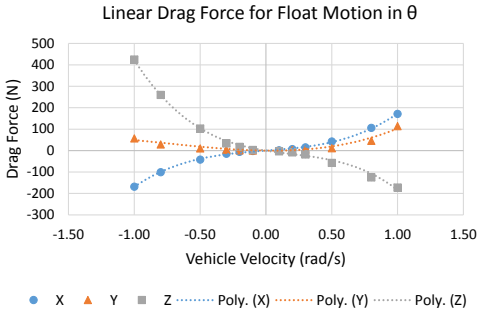

(a) Linear hydrodynamic force

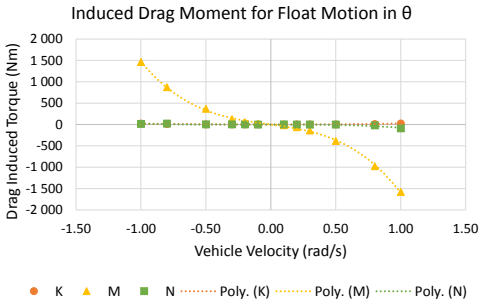

(b) Rotational hydrodynamic moment

Figure 5.5: Third order polynomial fitted curves for float pitch about the y-axis. Markers show measurements from flow simulations while dotted lines show polynomial fitted curves.

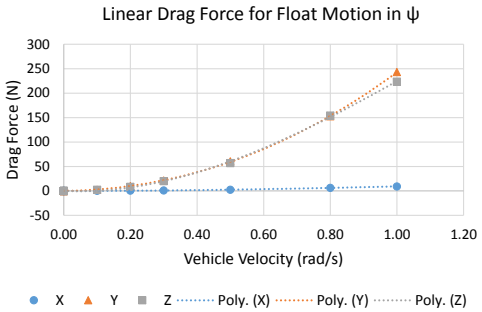

(a) Linear hydrodynamic force

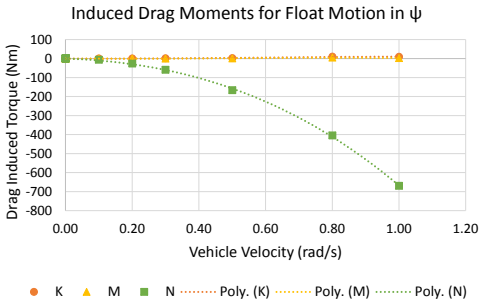

(b) Rotational hydrodynamic moment

Figure 5.6: Third order polynomial fitted curves for float yaw about the z-axis. Markers show measurements from flow simulations while dotted lines show polynomial fitted curves.

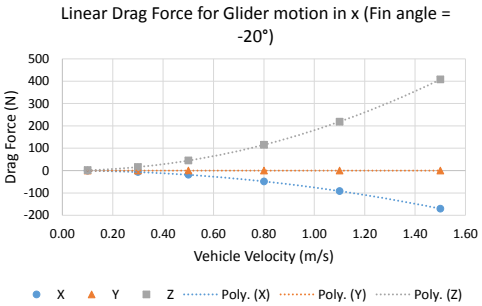

(a) Linear hydrodynamic force

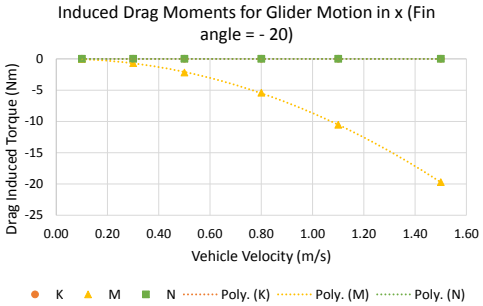

(b) Rotational hydrodynamic moment

Figure 5.7: Third order polynomial fitted curves for glider motion in the x-direction for fin angle of $-20°$. Markers show measurements from flow simulations while dotted lines show polynomial fitted curves.

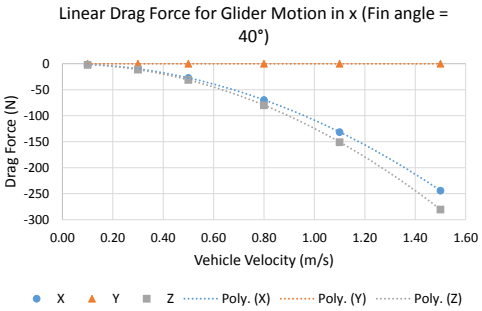

(a) Linear hydrodynamic force

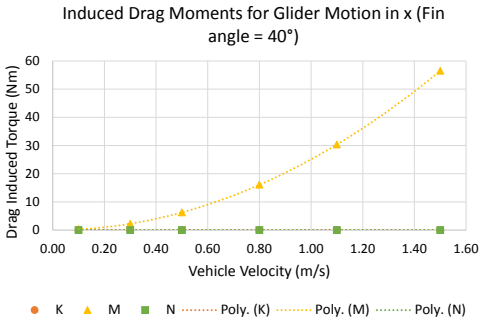

(b) Rotational hydrodynamic moment

Figure 5.8: Third order polynomial fitted curves for glider motion in the x-direction for fin angle of $40°$. Markers show measurements from flow simulations while dotted lines show polynomial fitted curves.

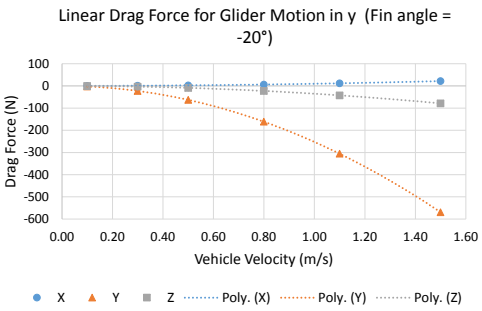

(a) Linear hydrodynamic force

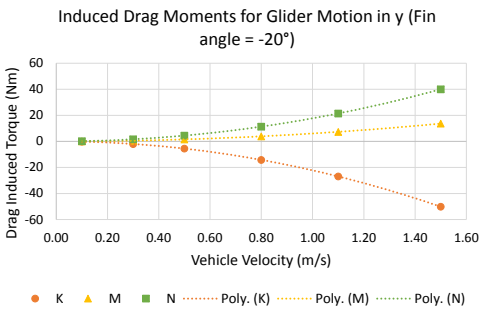

(b) Rotational hydrodynamic moment

Figure 5.9: Third order polynomial fitted curves for glider motion in the y-direction for fin angle of $-20°$. Markers show measurements from flow simulations while dotted lines show polynomial fitted curves.

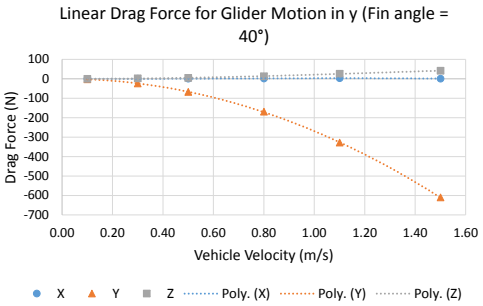

(a) Linear hydrodynamic force

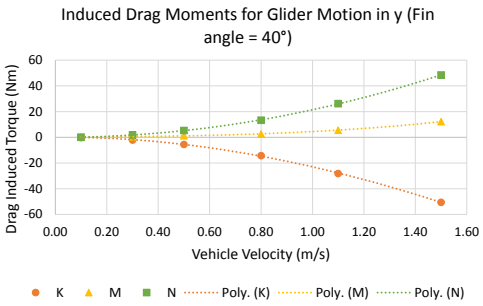

(b) Rotational hydrodynamic moment

Figure 5.10: Third order polynomial fitted curves for glider motion in the y-direction for fin angle of 40°. Markers show measurements from flow simulations while dotted lines show polynomial fitted curves.

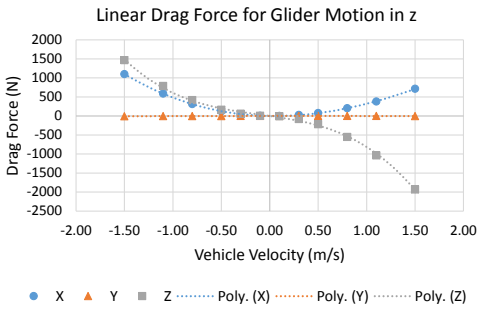

(a) Linear hydrodynamic force

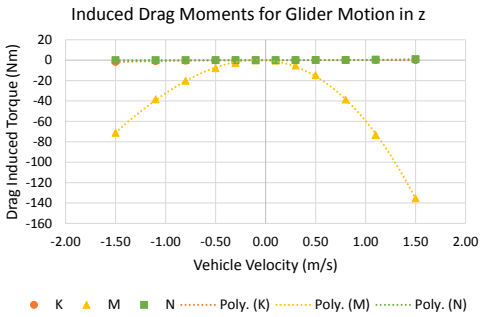

(b) Rotational hydrodynamic moment

Figure 5.11: Third order polynomial fitted curves for glider motion in the z-direction for fin angle of $-20°$ when the vehicle velocity is positive and fin angle of 40° when the vehicle velocity is negative. Markers show measurements from flow simulations while dotted lines show polynomial fitted curves.

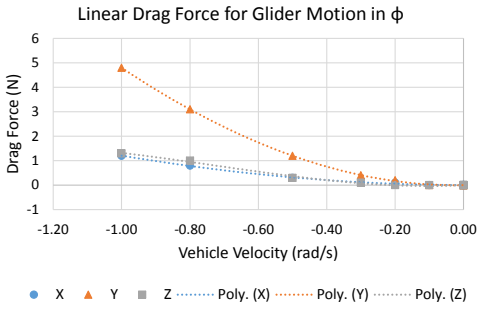

(a) Linear hydrodynamic force

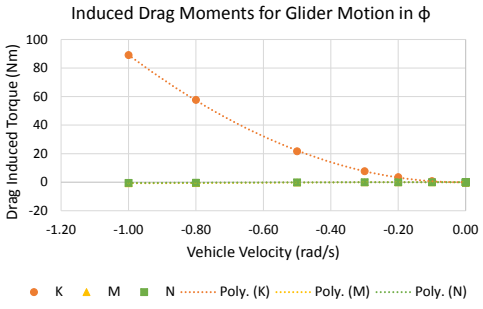

(b) Rotational hydrodynamic moment

Figure 5.12: Third order polynomial fitted curves for glider rotation about the x-axis. Markers show measurements from flow simulations while dotted lines show polynomial fitted curves.

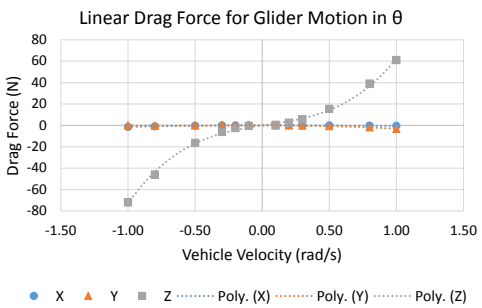

(a) Linear hydrodynamic force

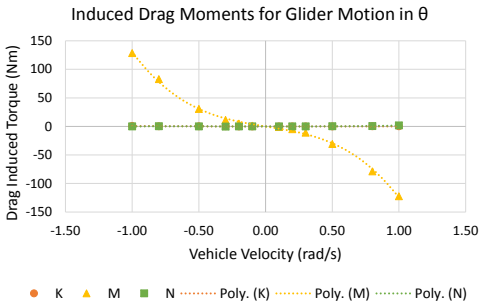

(b) Rotational hydrodynamic moment

Figure 5.13: Third order polynomial fitted curves for glider rotation about the y-axis. Markers show measurements from flow simulations while dotted lines show polynomial fitted curves.

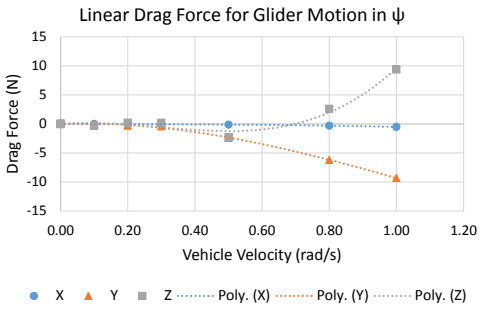

(a) Linear hydrodynamic force

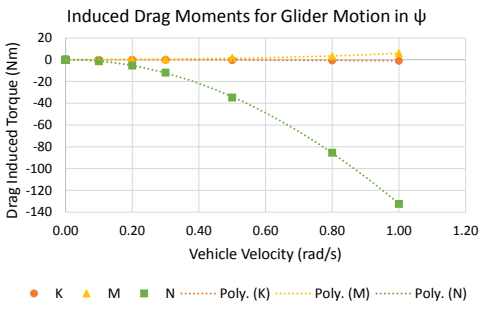

(b) Rotational hydrodynamic moment

Figure 5.14: Third order polynomial fitted curves for glider rotation about the z-axis. Markers show measurements from flow simulations while dotted lines show polynomial fitted curves.

The coefficient of determination for the third order polynomials fitted to the hydrodynamic forces for the glider are given in Table 5.2. The coefficients show that the polynomial fits are reasonably good with the worst being 0.84 for the hydrodynamic moment K for pitching motion, θ. Again the magnitude must be considered to evaluate if this is reasonable and again the magnitude can be seen to be reasonably small such that this fit is not a problem.

Table 5.2: Coefficients of determination, R^2, for third order polynomial fitted curves for hydrodynamic forces on glider. The polynomial curves for the hydrodynamic forces on the glider are shown in Fig.5.7 – 5.14.

Direction of float motion	Coefficient of determination for induced drag					
	X	Y	Z	K	M	N
x (fin angle = $-20°$)	1.00	1.00	1.00	1.00	1.00	1.00
x (fin angle = $40°$)	1.00	1.00	1.00	1.00	1.00	1.00
y (fin angle = $-20°$)	1.00	1.00	1.00	1.00	1.00	1.00
y (fin angle = $40°$)	0.92	1.00	1.00	1.00	1.00	1.00
z	1.00	1.00	1.00	1.00	1.00	1.00
ϕ	1.00	1.00	1.00	1.00	0.99	1.00
θ	1.00	0.99	1.00	**0.84**	1.00	0.93
ψ	0.99	1.00	0.97	0.99	0.99	1.00

The results from the flow simulations to determine the hydrodynamic forces on the glider caused by the rudder are shown in Fig. 5.15 – 5.20. The hydrodynamic forces and moments on the glider were determined for motion in the glider body-fixed x-axis for different rudder angles. The fitted surfaces were chosen to be third order with respect to the rudder angle and second order with respect to the glider velocity. A first order fit with respect to the rudder angle was initially tested but did not suitably predict the behaviour of the data when both the rudder angle and the glider velocity tended to zero.

It can be seen that the forces and rolling moment applies on the glider, X, Y, Z and K in Fig. 5.15, 5.16, 5.17, and 5.18 respectively, are rather small when compared to the other hydrodynamic forces and moments. The pitching and yawing moments, M and N in Fig. 5.19 and 5.20 respectively, are significant and this yawing moment will allow for the control of the glider yaw orientation.

The coefficients of determination for the surfaces fitted to the hydrodynamic forces caused by the rudder on the glider are shown in Table 5.3. All of the fitted surfaces have suitable good fits.

Table 5.3: Coefficients of determination, R^2, for polynomial (poly32) fitted curves for induced forces and moment caused by rudder on glider. The polynomial curves for the hydrodynamic forces caused by the rudder are shown in Fig. 5.15 – 5.20.

	Coefficient of determination for induced drag
X	1.00
Y	1.00
Z	0.99
K	1.00
M	1.00
N	1.00

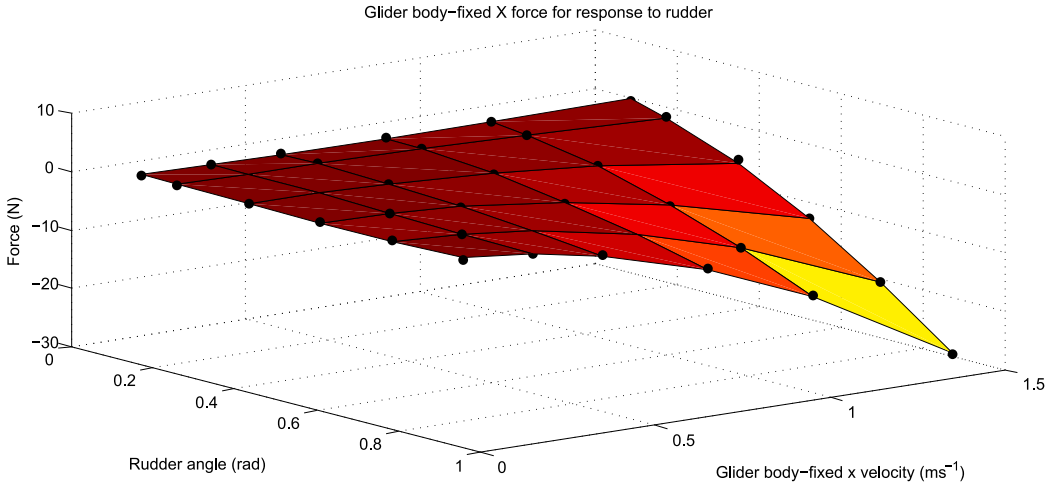

Figure 5.15: Surface fitted to linear hydrodynamic force in glider body-fixed x-direction for certain rudder angles and body-fixed velocities. Discrete points show measurements while the surface shows the fitted polynomial curve of order 3 for rudder angle and 2 for glider body-fixed x velocity.

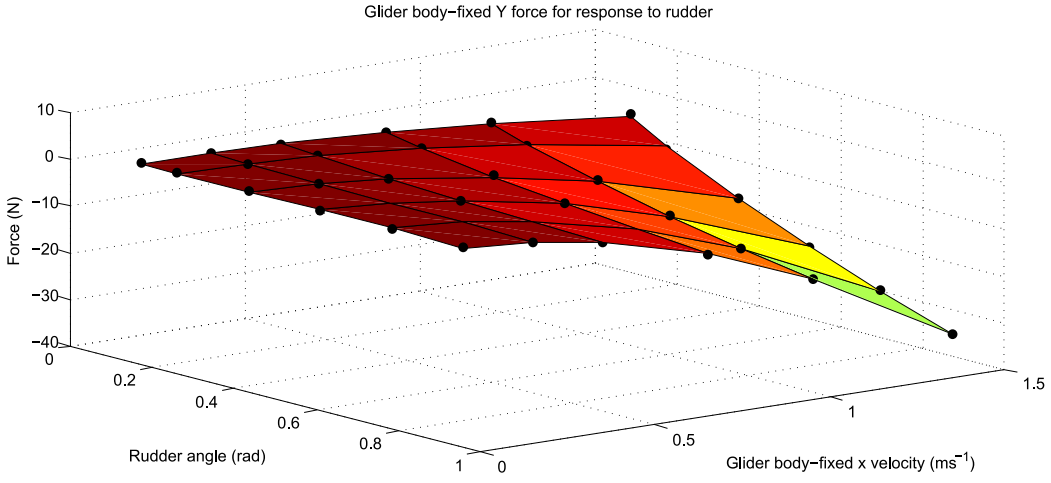

Figure 5.16: Surface fitted to linear hydrodynamic force in glider body-fixed y-direction for certain rudder angles and body-fixed velocities. Discrete points show measurements while the surface shows the fitted polynomial curve of order 3 for rudder angle and 2 for glider body-fixed x velocity.

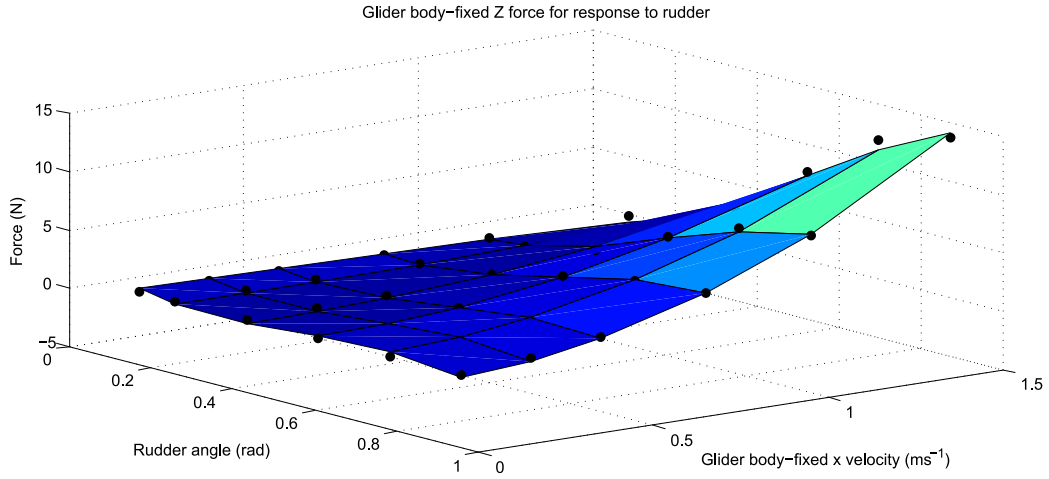

Figure 5.17: Surface fitted to linear hydrodynamic force in glider body-fixed z-direction for certain rudder angles and body-fixed velocities. Discrete points show measurements while the surface shows the fitted polynomial curve of order 3 for rudder angle and 2 for glider body-fixed x velocity.

Figure 5.18: Surface fitted to induced hydrodynamic rolling moment about glider body-fixed x-axis for certain rudder angles and body-fixed velocities. Discrete points show measurements while the surface shows the fitted polynomial curve of order 3 for rudder angle and 2 for glider body-fixed x velocity.

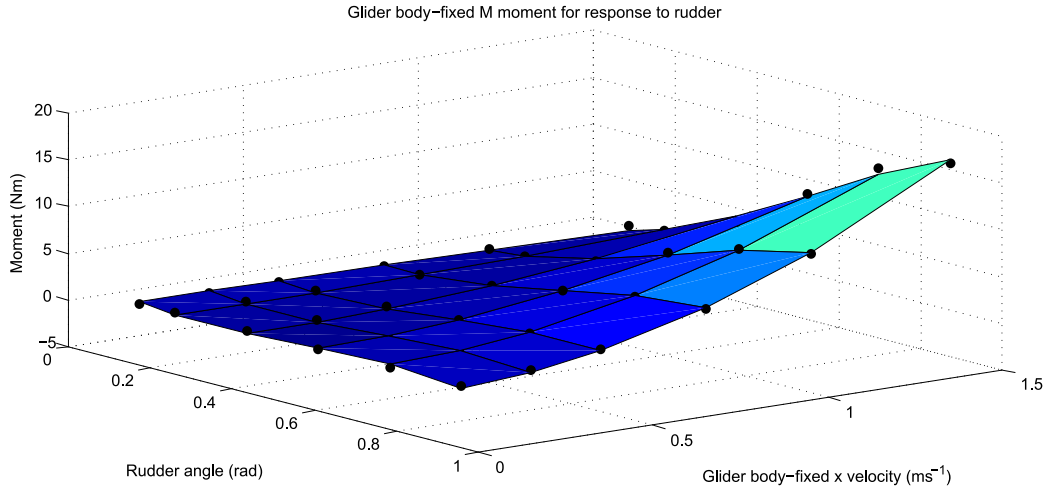

Figure 5.19: Surface fitted to induced hydrodynamic pitching moment about glider body-fixed y-axis for certain rudder angles and body-fixed velocities. Discrete points show measurements while the surface shows the fitted polynomial curve of order 3 for rudder angle and 2 for glider body-fixed x velocity.

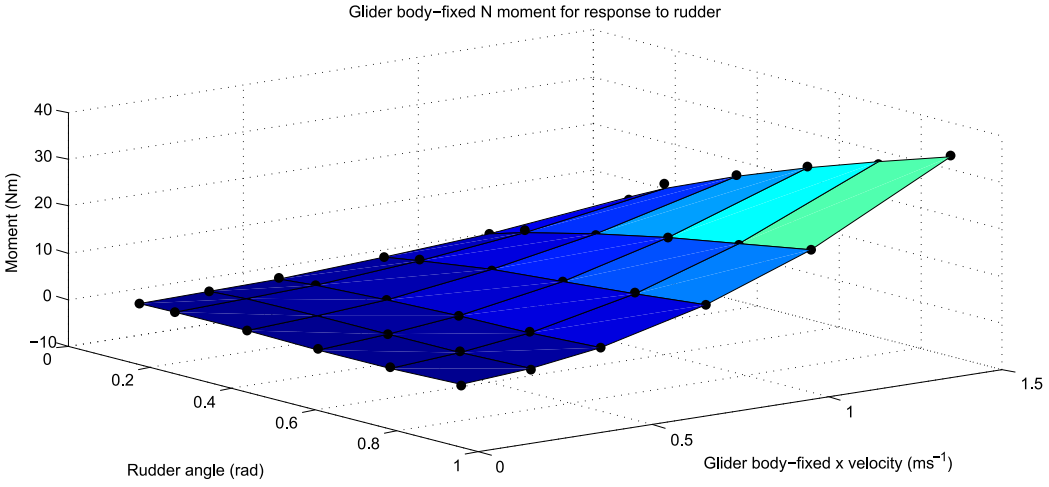

Figure 5.20: Surface fitted to induced hydrodynamic yawing moment about glider body-fixed z-axis for certain rudder angles and body-fixed velocities. Discrete points show measurements while the surface shows the fitted polynomial curve of order 3 for rudder angle and 2 for glider body-fixed x velocity.

The results from the flow simulations for the hydrofoil hydrodynamic forces and moments are shown in Fig. 5.21 – 5.27. It can be seen that the hydrodynamic forces in the glider body-fixed x- and z-directions for motion in the x- and z-directions, when considering the hydrofoil angle, will be more reasonable than the worst cases considered in the glider hydrodynamic simulations. The forces tend to zero when the hydrofoil angle or the glider velocity tends to zero and have a maximum value when the hydrofoil angle and the glider velocity are at a maximum. The hydrodynamic forces in the glider body-fixed x- and z-directions caused by pitching of the hydrofoil are insignificantly small, whereas the damping moment for the pitching of the hydrofoil is significant enough to prevent oscillations.

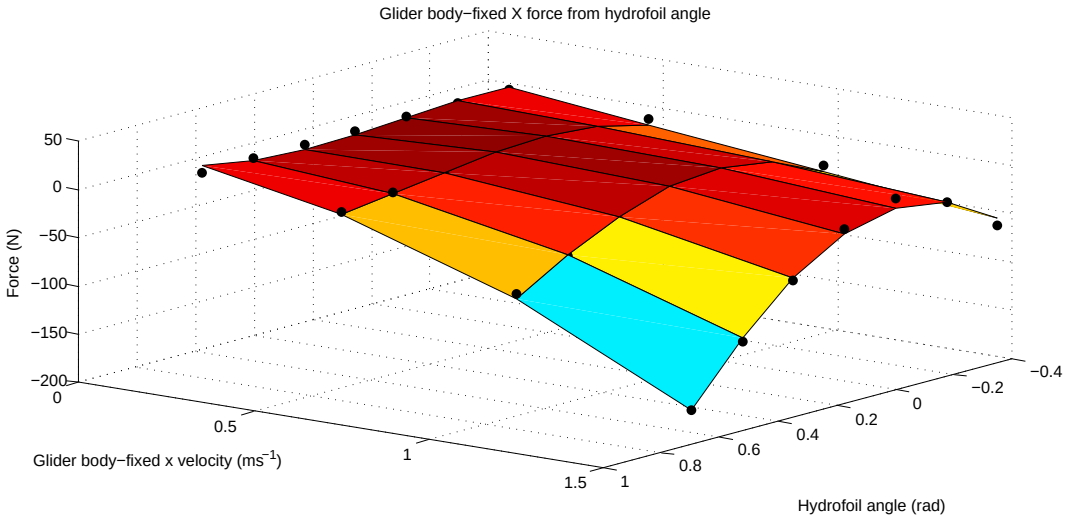

Figure 5.21: Surface fitted to linear hydrodynamic force in glider body-fixed x-direction for certain hydrofoil angles and body-fixed velocities. Discrete points show measurements while the surface shows the fitted polynomial curve of order 3 for hydrofoil angle and 2 for glider body-fixed x velocity.

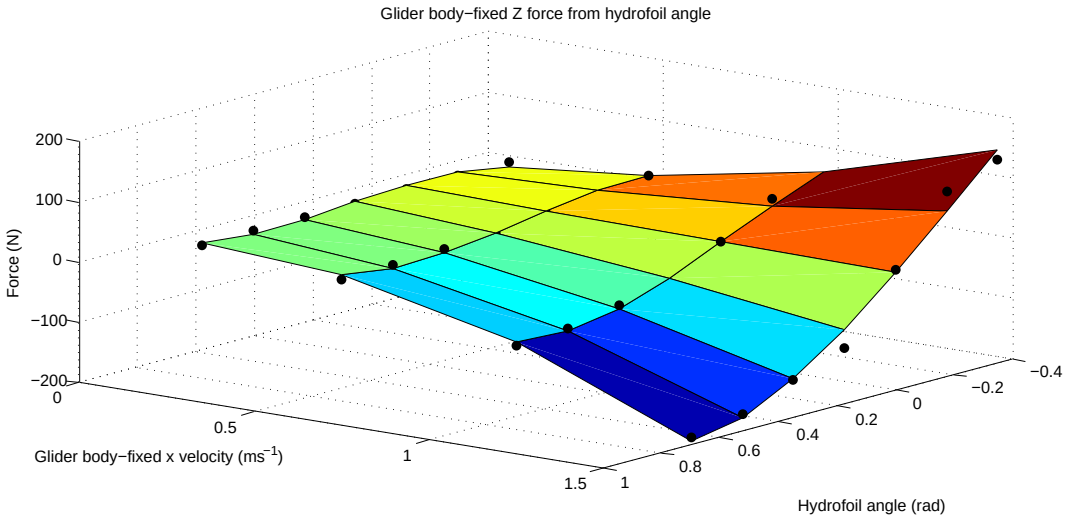

Figure 5.22: Surface fitted to linear hydrodynamic force in glider body-fixed z-direction for certain hydrofoil angles and body-fixed velocities. Discrete points show measurements while the surface shows the fitted polynomial curve of order 3 for hydrofoil angle and 2 for glider body-fixed x velocity.

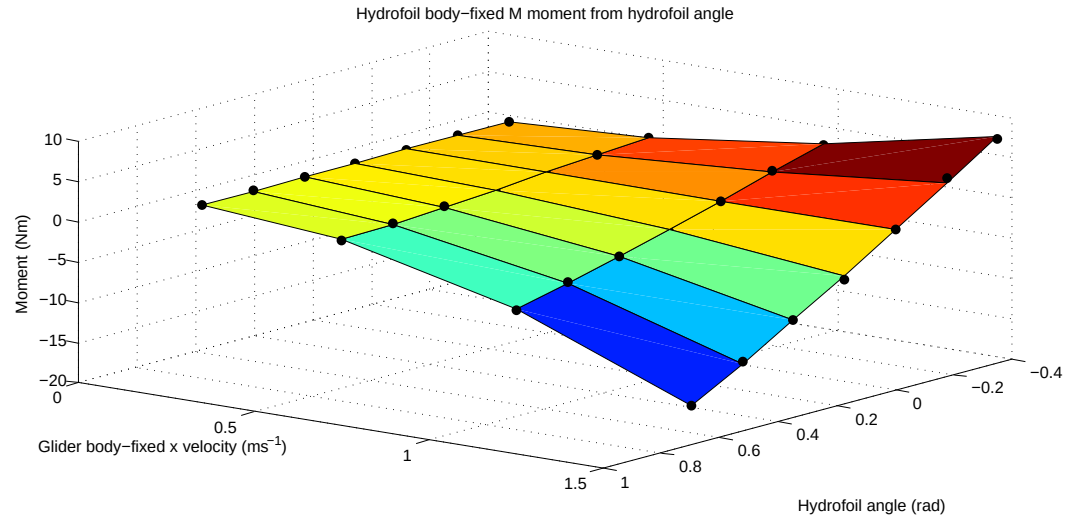

Figure 5.23: Surface fitted to induced hydrodynamic moment about hydrofoil body-fixed y-axis for certain hydrofoil angles and body-fixed velocities. Discrete points show measurements while the surface shows the fitted polynomial curve of order 3 for hydrofoil angle and 2 for glider body-fixed x velocity.

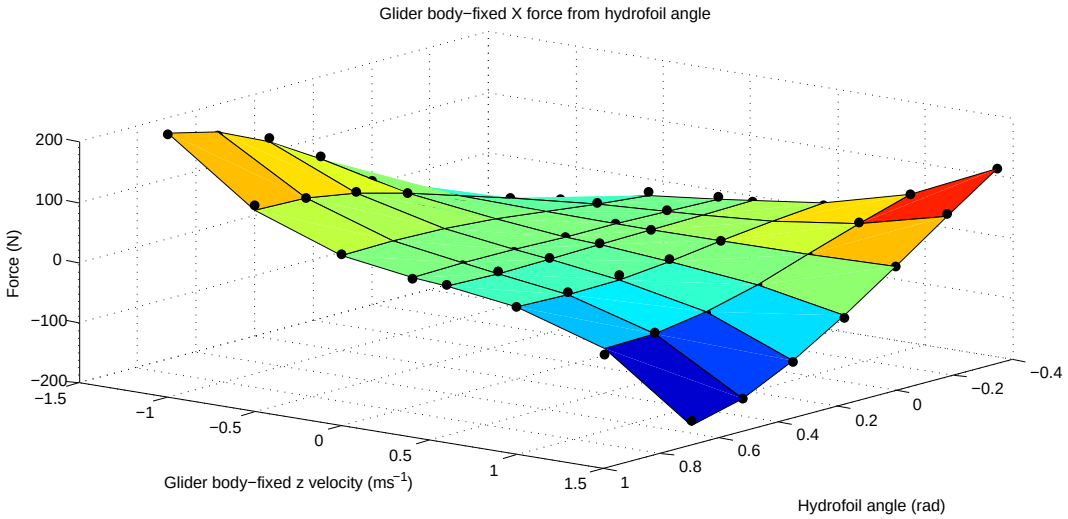

Figure 5.24: Surface fitted to linear hydrodynamic force in glider body-fixed x-direction for certain hydrofoil angles and body-fixed velocities. Discrete points show measurements while the surface shows the fitted polynomial curve of order 4 for hydrofoil angle and 3 for glider body-fixed z velocity.

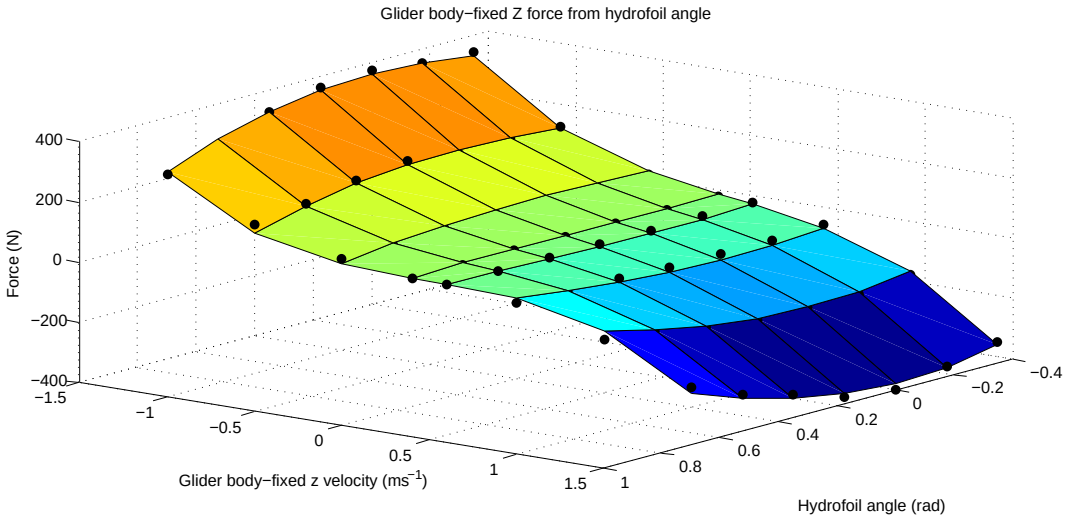

Figure 5.25: Surface fitted to linear hydrodynamic force in glider body-fixed z-direction for certain hydrofoil angles and body-fixed velocities. Discrete points show measurements while the surface shows the fitted polynomial curve of order 3 for hydrofoil angle and 3 for glider body-fixed z velocity.

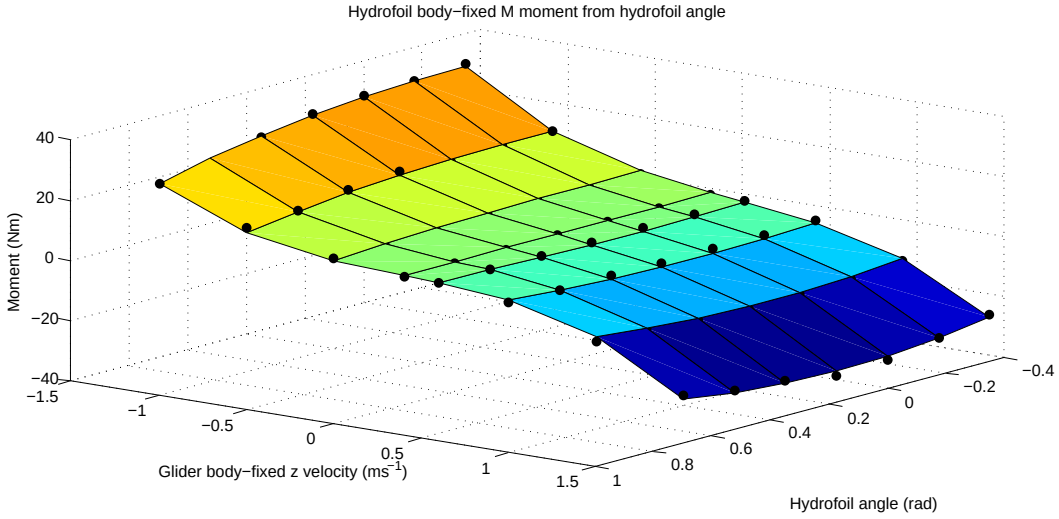

Figure 5.26: Surface fitted to induced hydrodynamic moment about hydrofoil body-fixed y-axis for certain hydrofoil angles and body-fixed velocities. Discrete points show measurements while the surface shows the fitted polynomial curve of order 3 for hydrofoil angle and 3 for glider body-fixed z velocity.

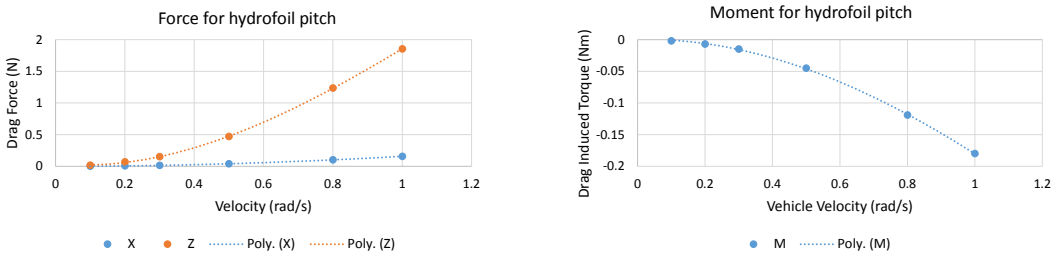

(a) Linear hydrodynamic force **(b)** Rotational hydrodynamic moment

Figure 5.27: Third order polynomial fitted curves for hydrofoil for rotation about the y-axis. Markers show measurements from flow simulations while dotted lines show polynomial fitted curves.

The coefficients of determination, R^2, for the surfaces and curves fitted for the hydrodynamic forces caused by the hydrofoil are shown in Table 5.4. All of the fits for the hydrodynamic forces and moments caused by the hydrofoil are good.

Table 5.4: Coefficients of determination, R^2, for the polynomial fitted curves for induced forces and moment on hydrofoil. The polynomial curves for the hydrodynamic forces acting on the hydrofoil are shown in Fig. 5.21 – 5.27.

Direction of motion	Coefficient of determination for induced drag		
	X	Z	M
x	0.99	0.98	1.00
z	1.00	1.00	1.00
θ	1.00	1.00	1.00

5.2 Added mass calculations

This section presents the empirical added mass calculations for the float and the glider. First the calculation of the added mass for the float is covered, followed by that of the glider. The added mass components for the float and the glider are presented in Tables 5.7 and 5.9 respectively making use of the parameters presented in Tables 5.6 and 5.8. The calculation of each component will be given a brief explanation to show which parameters and methods were used and to explain any assumptions made.

The coefficients of added mass, k, for methods 1, 2, and 3 presented for the calculation of the glider's added mass in Table 3.4 are discrete, yet dependent on the ratio of the sides of the shape. The interpolations for these added mass coefficients are presented in Fig. 5.28, using power fitted curves for method 1 and 2, and a 4^{th} order polynomial for method 3. The respective coefficients of determination are presented in Table 5.5 and show that the fitted curve are suitable.

Each of the calculations for the added mass components for the float are shown in Table 5.7 where the methods used are shown in Table 3.3 for methods 1, 2 and 3, and Table 3.4 for method g2 which denotes method 2 in the glider added mass methods table. The parameters used are shown in Table 5.6, where the parameters were taken from the physical measurements and from

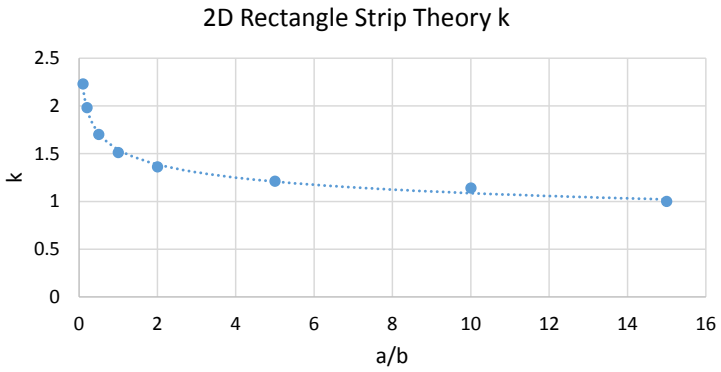

(a) Method 1.

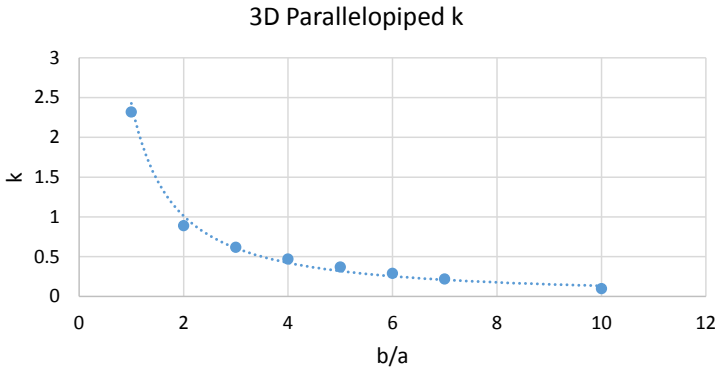

(b) Method 2.

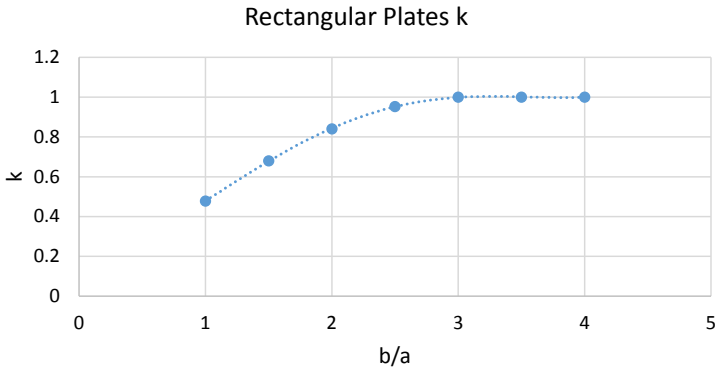

(c) Method 3.

Figure 5.28: Fitted curves for added mass coefficients, k, for glider added mass calculations. The discrete markers show the values for the coefficients of added mass while the dotted lines show the respective fitted curves. Method 1, **(a)**, and method 2, **(b)**, are fitted to a power curves, while method 3, **(c)**, is fitted to a 4^{th} order polynomial curve.

Table 5.5: Coefficients of determination, R^2, for fitted curves for added mass coefficients, k, for empirical methods of calculating added mass.

Method	Coefficient of determination
1	0.99
2	0.98
3	1.00

the SV3 specifications sheet [29]. Method 2 was used in the calculation of the components $X_{\dot{u}}$ and $Y_{\dot{u}}$. Method 2 assumes a square cross-sectional area, with length a, for motion parallel to the surface and thus the area of the face was calculated making use of the appropriate dimensions. The dimensions length and height were used for $X_{\dot{u}}$ and width and height for $Y_{\dot{v}}$; the length a for the square face was calculated based on the area of the face from the relevant dimensions. The added mass component was then calculated; however, the assumption of a square face is not ideal for calculation of the $X_{\dot{u}}$ component and thus method g2 was used as well even though the float was not fully submerged; the submerged dimensions for the float were used when calculating the added mass from method g2. Method 3 is also used to calculate the component $Y_{\dot{v}}$ as the hull of the float can also be compared to a cylinder instead of a parallelepiped. Method 1 was used to calculate the component $Z_{\dot{w}}$ which also makes the assumption of a square face and thus the width and height of the float were used to calculate the area of the cross-section. The rotational added mass components, $K_{\dot{p}}, M_{\dot{q}}$ and $N_{\dot{r}}$, were calculated using slender body methods and the results made use of the results from method g2 for $X_{\dot{u}}$, method 3 for $Y_{\dot{v}}$, and the single result for $Z_{\dot{w}}$.

Each of the calculations for the added mass components for the glider are shown in Table 5.9 making use of the methods presented in Table 3.4. The parameters used are shown in Table 5.8, which were calculated from physical measurements and from the SV3 specification sheet [29]. For the calculation of the $X_{\dot{u}}$ component the projected volume of the worst case scenario was considered, where the hydrofoils on the glider had an angle of 40°. Method 1 was used taking the width as $2a$ and the total length of the fin section as $2b$. The ratio $\frac{a}{b}$ was used to calculate k and thus the added mass component could be calculated. For the calculation of the $Y_{\dot{v}}$ component the glider body was treated as a rectangular plate. The height of the glider was used as a and the length used as b for the calculation of k and subsequently the added mass component. For the calculation of the $Z_{\dot{w}}$ component the worst case was considered, where the hydrofoils had an angle of 0°. A single hydrofoil pair was initially considered and then the result was multiplied for the six pairs, thus the length of a single fin was used as a and the width used for b. The length of the glider is not much greater than the width, such that the assumption of a slender body is not viable. Method 4 was used to calculate the rotational added mass coefficients for the glider as the glider can be seen to be made of plane laminas. For component $K_{\dot{p}}$, a single

Table 5.6: Float parameters for calculation of added mass from measurements and specification sheet [29], where submerged parameters make use of the nominal measurements.

Parameter	Value
ρ	1000 kg·m^{-3}
Length	3.05 m
Width	0.81 m
Height	0.23 m
Submerged Width	0.69 m
Submerged Height	0.19 m

Table 5.7: Calculation of added mass for float making use of methods presented in Table 3.3 for float methods and presented in Table 3.4 for glider method, g2.

Direction of motion	Method	a	r	b	$\frac{b}{a}$	k	l	Area of face	Added Mass
$X_{\dot{u}}$	2	0.42				0.25	0.81	0.70	111.57
	g2	0.36		3.05	8.42	0.17		0.13	66.18
$Y_{\dot{v}}$	2	0.22				0.25	3.05	0.19	111.57
	3		0.18			0.50	3.05	0.13	157.02
$Z_{\dot{w}}$	1	0.22				0.75	3.05	0.19	334.71
$K_{\dot{p}}$	slender								1.87
$M_{\dot{q}}$	slender								49.47
$N_{\dot{r}}$	slender								46.77

hydrofoil pair was considered as a rotating plane lamina and the result multiplied for the six hydrofoil pairs, where the hydrofoil angle was 0°. For component $M_{\dot{q}}$ the glider hydrofoils were treated as a single rotating plane lamina where the hydrofoil angle was 0°. For component $N_{\dot{r}}$ the glider body was treated as a rotating plane lamina.

Table 5.8: Glider parameters for calculation of added mass taken from measurements and specification sheet [29].

Parameter	Value
ρ	1000 kg·m^{-3}
Length	2.13 m
Width	1.42 m
Height	0.21 m
Total Fin Length	1.17 m
Fin Width	1.42 m
Maximum Fin Height	0.113 m
Single Fin Length	0.176 m

Table 5.9: Calculation of added mass for glider making use of methods presented in Table 3.4.

Direction of motion	Method	a	b	$\frac{a}{b}$	$\frac{b}{a}$	k	l	Added Mass
$X_{\dot{u}}$	1	0.71	0.59	1.21		1.50	0.11	268.10
$Y_{\dot{v}}$	3	0.21	2.13		10.14	1		73.78
$Z_{\dot{w}}$	3	0.18	1.42		8.07	1		207.28
$K_{\dot{p}}$	4	0.71					0.18	105.38
$M_{\dot{q}}$	4	0.59					1.42	65.31
$N_{\dot{r}}$	4	1.07					0.21	106.09

5.3 Model validation

The validation of the Wave Glider model developed in Chapter 3 includes confirming the rigid-body motion, and then comparing the motion of the float and the glider in each relevant generalised coordinate with the added effects from hydrodynamic forces and added mass. This

is followed by confirming the restorative buoyancy force on the float and the resultant propulsion developed by the hydrofoils applied for a sinusoidal sea state.

To show the response of the float and the glider and validate the effects of including hydrodynamic forces and added mass, a force of 50 N was used to examine the response in linear directions and a moment of 5 N·m was used to examine the response in angular directions. These responses are shown in Fig. 5.29 – 5.34 where the float and glider responses are shown side-by-side to compare the responses between the two bodies as well as to show the responses in each specific direction. It should be noted that the responses in the linear directions for the float and the glider are inherently linked as the bodies are rigidly connected.

In Fig. 5.29 and 5.30 the responses to the force in the x- and y-direction, respectively, are examined for the float and the glider. The rigid-body response gives a baseline in terms of the unrestricted motion that can be expected. It can be seen that the hydrodynamic forces, drag, and the added mass have similar effects of reducing the effective distance travelled by the float and glider, however the origin of these effects are different, as the added mass effectively increases the kinetic energy needed to induce motion in the body while the hydrodynamic force introduces damping. The effects of the hydrodynamic forces and added mass are similar for the x-direction test, however the hydrodynamic forces have a significantly greater effect as compared to the added mass for the y-direction. The effect of the combined hydrodynamic forces and added mass can be seen to provide more resistance than either of individual effects as the distance travelled is significantly less as compared to the distance travelled for only the hydrodynamic forces, added mass or rigid-body tests.

The response for the float and the glider for a constant force in the z-direction is shown in Fig. 5.31. The response for both bodies is oscillatory because of the restorative buoyancy force and the fact that the bodies are rigidly connected. The inclusion of hydrodynamic forces cause the oscillations to be damped while remaining at the same frequency as the rigid-body only case, which will result in the bodies settling to some depth. The inclusion of the added mass causes the frequency of the oscillation to be lower than the rigid-body case however does not include any damping. The combination of these effects is shown to damp the oscillations at a lower frequency.

The responses to the constant moment about the body-fixed x-axes of the float and the glider are shown in Fig. 5.32. The response for the float, Fig. 5.32a, is slightly complex as it includes the effects of the tether and the restorative buoyancy moment. The effect of the tether will have an appreciable effect because of the shape of the hull leading to a small moment of inertia about the x-axis. These effects lead to a complex response for both the rigid-body and added mass responses. When looking at the effects of hydrodynamic forces on the float, it can be seen that although the initial amplitude of the oscillations are smaller than the rigid-body response, these oscillations increase until they reach a maximum. The combination of the hydrodynamic forces and added mass results in a non-regular oscillation that has a lower amplitude and frequency as compared to solely the hydrodynamically damped response. The glider, Fig. 5.32b, exhibits a more regular response when looking at the rigid-body response, which is likely due to the effects of the tether being less significant because of the larger moment of inertia of the glider about its x-axis because of the hydrofoils. The inclusion of added mass has the effect of reducing the frequency of the regular oscillatory response while the effect of the hydrodynamic forces provides some damping resulting in a less regular response. Looking at the combined response to the added mass and hydrodynamic forces for the glider it can be seen that the response has a lower frequency than the rigid-body response and exhibits damping characteristics.

Fig. 5.33 shows the responses for the float and the glider to a constant moment about their y-axes. The float rigid-body response is oscillatory because of the restorative buoyancy moment,

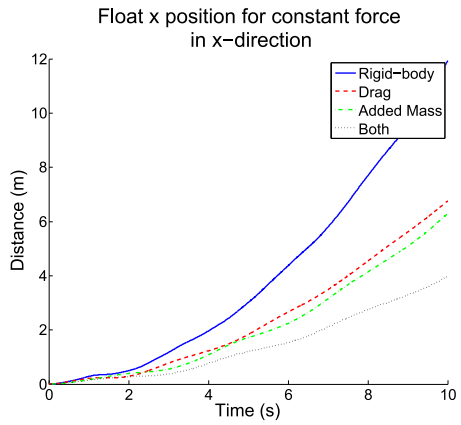

(a) Plot showing float reaction in the x-direction for a constant force in the x-direction.

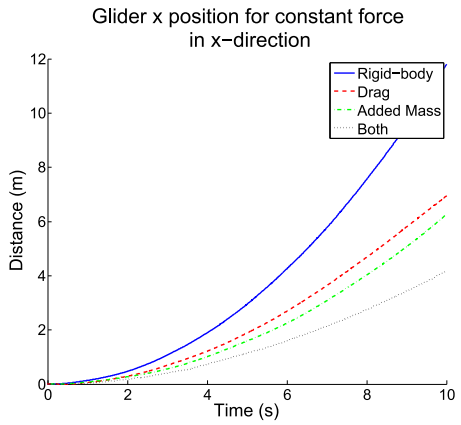

(b) Plot showing glider reaction in the x-direction for a constant force in the x-direction.

Figure 5.29: Reactions of float and glider to constant force in the x-direction.

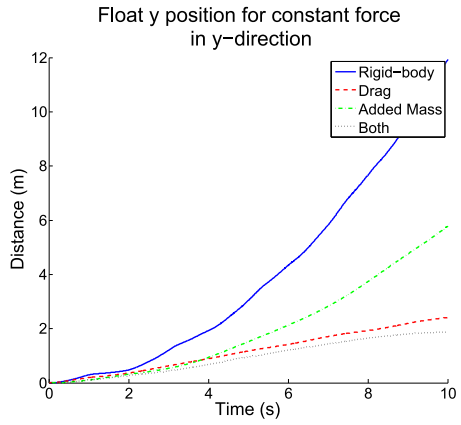

(a) Plot showing float reaction in the y-direction for a constant force in the y-direction.

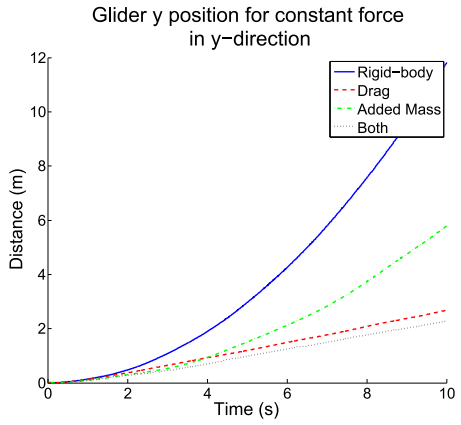

(b) Plot showing glider reaction in the y-direction for a constant force in the y-direction.

Figure 5.30: Reactions of float and glider to constant force in the y-direction.

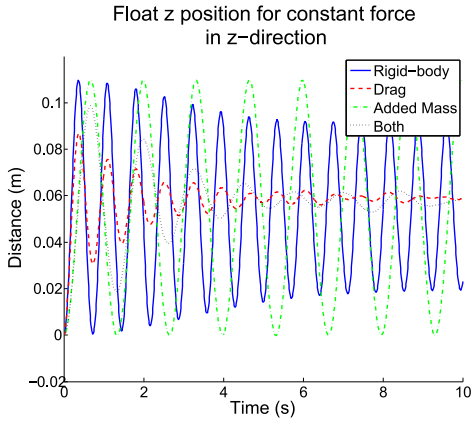

(a) Plot showing float reaction in the z-direction for a constant force in the z-direction.

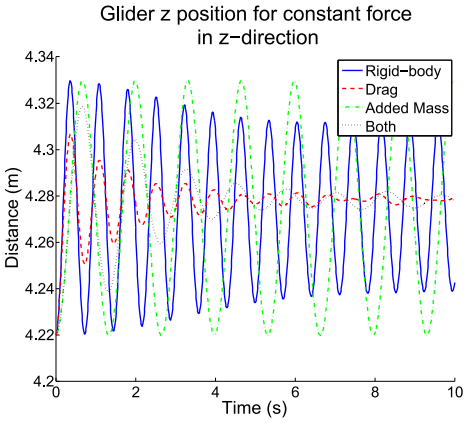

(b) Plot showing glider reaction in the z-direction for a constant force in the z-direction.

Figure 5.31: Reactions of float and glider to constant force in the z-direction.

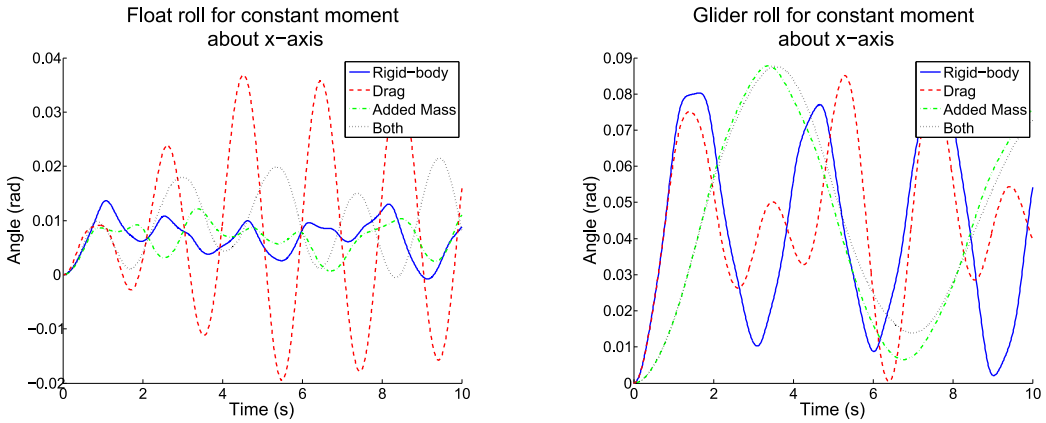

(a) Plot showing float roll for a constant moment about the x-axis.

(b) Plot showing glider roll for a constant moment about the x-axis.

Figure 5.32: Reactions of float and glider to constant moment about the x-axis.

whereas the response is damped when including the hydrodynamic forces. The effect of the added mass can be seen to reduce the frequency of the oscillations, with the combined effect of the added mass and hydrodynamic forces resulting in a damped lower frequency oscillation. The rigid-body response of the glider can also be seen to be oscillatory in comparison to that of the float, however at a much lower frequency. The inclusion of added mass results in a lower frequency oscillatory response while the inclusion of hydrodynamic forces results in a non-regular oscillatory response with a much smaller magnitude as compared to the rigid-body and added mass responses, that is likely influenced by the tether forces. The response when implementing both the hydrodynamic forces and added mass can be seen to include the damping effects of the hydrodynamic forces with the increased inertia of the added mass.

The responses for the float and glider to a constant moment about their respective z-axes are shown in Fig. 5.34. For the float it can be seen that the hydrodynamic forces have a much greater effect as compared to the added mass with both resulting in a smaller yaw response as compared to the rigid-body response. When examining their combined effect, the overriding effect of the hydrodynamic damping results in a response that is very similar to that of only the hydrodynamic forces. For the glider yaw response the added mass has a slightly greater effect resulting in less yawing as compared to the hydrodynamic forces and the rigid-body responses. The combined response initially follows that of just the added mass but eventually results in less yawing as compared to the added mass response.

Overall, the inclusion of added mass and hydrodynamic forces into the Wave Glider model can be seen to provide reasonable damping effects and increased model inertia where applicable. Thus the inclusion of added mass and hydrodynamic forces will likely improve the fidelity of the model.

The buoyancy force is tested for a sinusoidal sea state with a peak-to-peak amplitude of 2 m and a frequency of 0.1 rad·s^{-1}, approaching the vessel from the positive x-direction. This simple sinusoidal sea state was chosen to represent the swell that would be expected from a typical sea spectrum [33]. The comparison between the float height and the sea state height at the float position is shown in Fig. 5.35, and the comparison between the float pitch and the sea state angle along the x-direction is shown in Fig. 5.36 for the same test. Fig. 5.35 shows the change in the height of the float with respect to the inertial frame in response to the changing sea state height. The float height follows that of the sea state due to the change in the buoyancy force acting on the float to maintain the equilibrium between the gravitational force and the

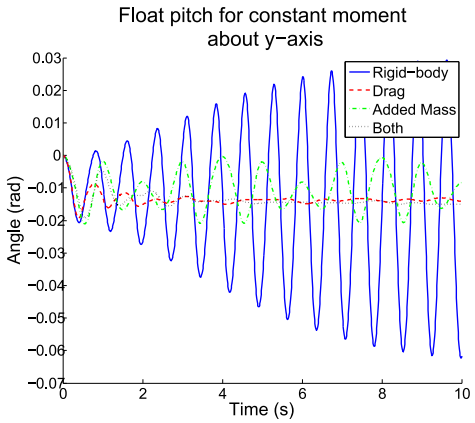

(a) Plot showing float pitch for a constant moment about the y-axis.

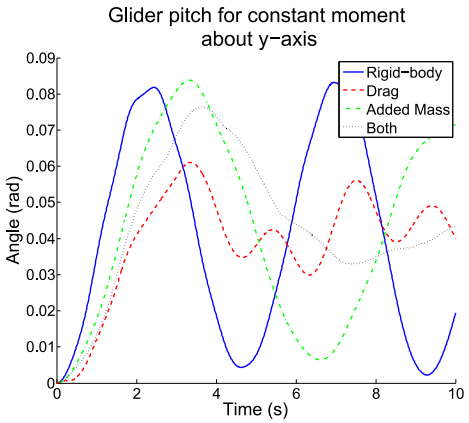

(b) Plot showing glider pitch for a constant moment about the y-axis.

Figure 5.33: Reactions of float and glider to constant moment about the y-axis.

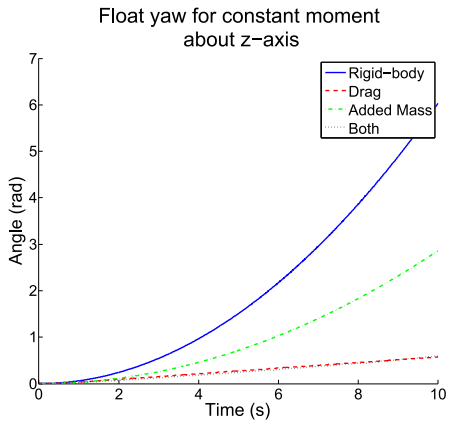

(a) Plot showing float yaw for a constant moment about the z-axis.

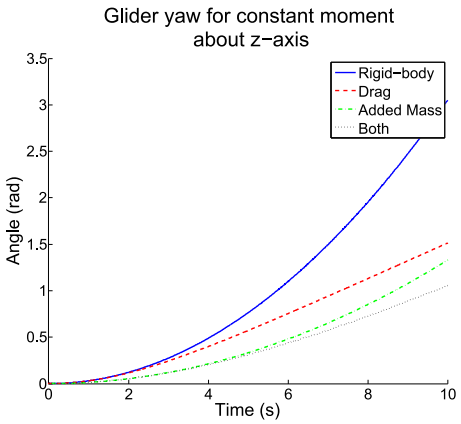

(b) Plot showing glider yaw for a constant moment about the z-axis.

Figure 5.34: Reactions of float and glider to constant moment about the z-axis.

buoyancy forces acting on the Wave Glider system. The response is generally quite regular with some slight anomalies that can be attributed to forces acting through the tether. Similarly, to show that the buoyancy moment is acting correctly, the comparison between the pitch of the float and the angle of the sea state along the x-direction is shown in Fig. 5.36. It can be seen that the low-frequency response of the pitch of the float follows the angle of the sea closely with some phase lag which is to be expected because of the moment of inertia of the float. There also seem to be superimposed high-frequency sinusoids present in the response which can be attributed to the tether or suggests that the buoyancy effect is poorly damped.

The wave-driven propulsion is shown in Fig. 5.37 and 5.38. There are two important links that must be shown to give an understanding of how the wave-driven propulsion for the Wave Glider model works. The first is the link between the glider x-velocity and the sea state, shown in Fig. 5.37, where it can be seen that the glider x-velocity increases as the glider moves in the negative z-direction out of the water and decreases as the glider moves in the positive z-direction into the water. It should be noted that the glider x-velocity is always positive because of the nature of the propulsion provided by the hydrofoils. This interaction shows the dependency of the propulsion on the sea state.

Once the link is formed between the glider velocity and the sea state, it can be extended upon by showing the pitch of the hydrofoil in response to the sea state and the resultant change in float x-position, shown in Fig. 5.38. The hydrofoils perform as expected having a positive angle as the glider moves in the negative z-direction out of the water, and having a negative angle as the glider moves in the positive z-direction. The propulsion generated by the hydrofoils causes the float to move in the positive x-direction after a short delay caused by the fact that the glider is pulling the float along by the tether. There are some oscillations in the hydrofoils due to the utilization of the spring as a stopping device. However, from the hydrodynamic results it can be seen that the propulsive effects from these oscillation in the hydrofoils is minimal compared to the forces generated for a specific hydrofoil angle and thus these oscillations are a reasonable compromise.

The model validation shows that including the hydrodynamic factors, hydrodynamic damping forces and added mass, into the rigid-body model generated making use of Lagrangian modelling increases the fidelity of the model. It was also shown that the propulsive forces generated by the Wave Glider model are linked to the sea state and that the hydrofoils that generate this wave-driven propulsion operate as expected and within the limits imposed for the Wave Glider.

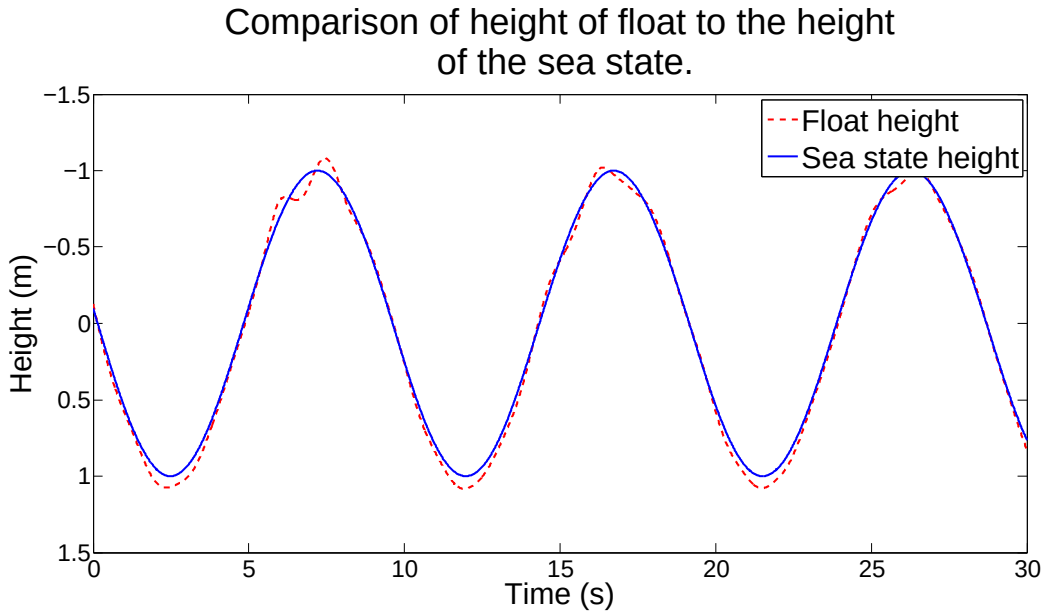

Figure 5.35: Comparison between height of float and height of sea surface. From the correlation of the height of the float and the height of the sea surface it can be seen that the buoyancy force is acting correctly in terms of height.

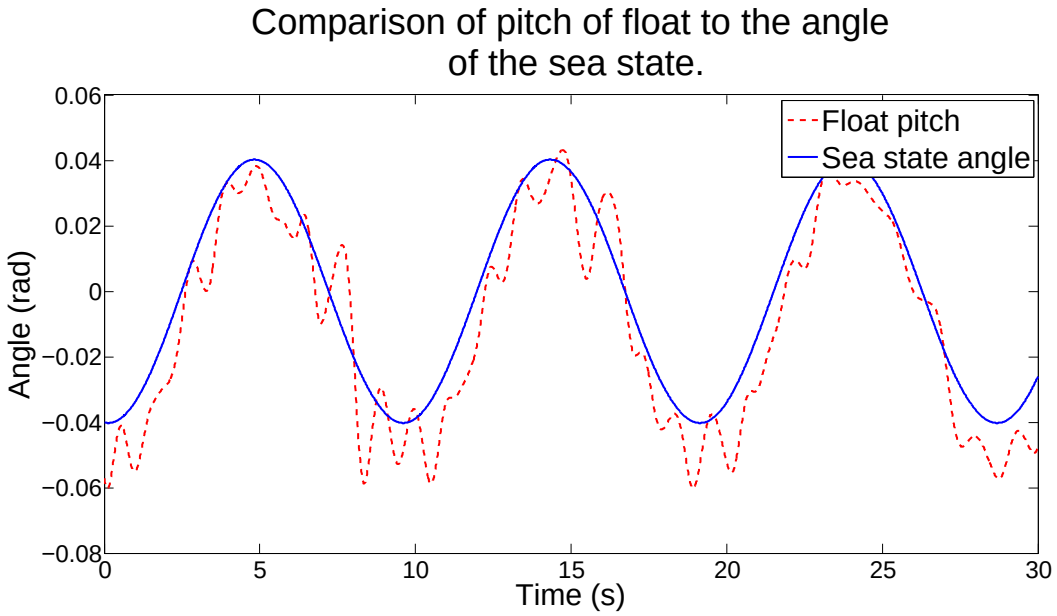

Figure 5.36: Comparison between pitch of float and angle of sea surface. From the correlation of the pitch of the float and the angle of the sea surface it can be seen that the buoyancy force is acting correctly to provide a restorative moment to the float.

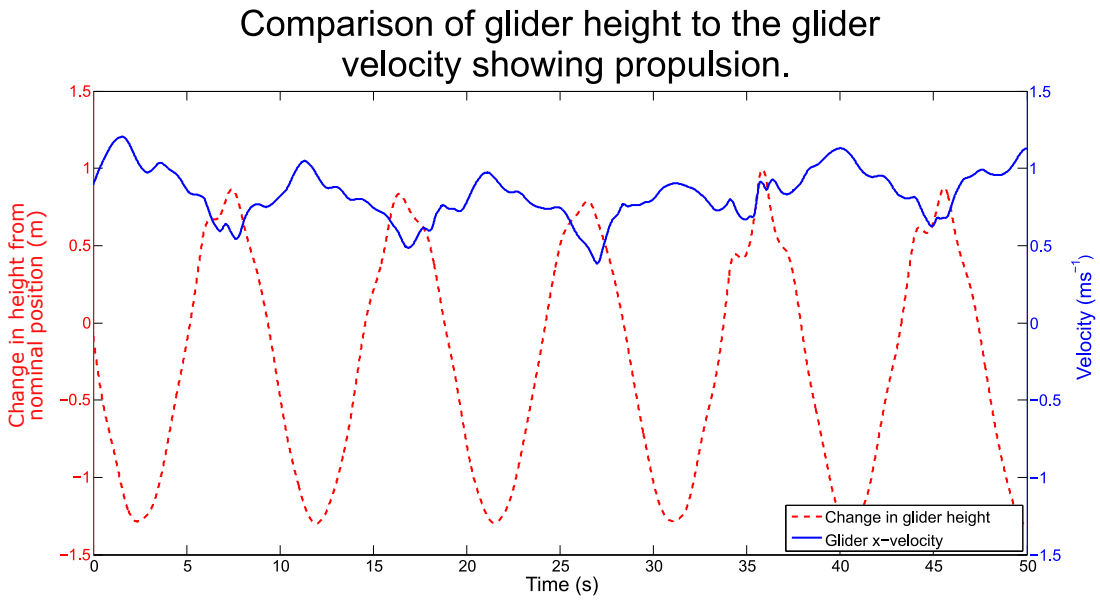

Figure 5.37: Plot showing dependency of propulsion on sea state by comparing glider x-velocity to change in glider height. It can be seen that the glider x-velocity increases as the glider moves in the negative z direction (less deep in the water) and decreases while the glider moves in the positive z direction (deeper into the water), however the velocity is always positive.

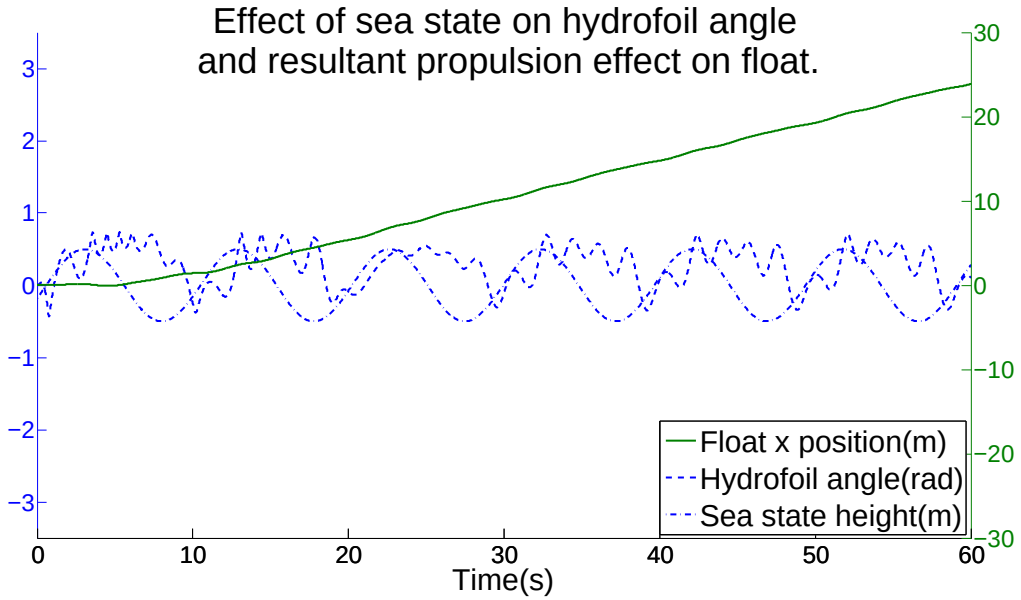

Figure 5.38: Change in the angle of the hydrofoils due to the sea state and the resultant propulsion applied onto the float resulting in the float moving in the positive x-direction. The hydrofoils act as expected having a positive angle for motion out of the water and a negative angle for motion into the water.

Chapter 6

Control implementation and validation

The controller implementation for the cascaded design expressed in Chapter 4 is presented in this chapter. First, the results of the glider yaw rate modelling are presented, following this the design for the glider yaw rate and glider yaw controllers is shown.

The results for the glider yaw rate modelling are presented in Table 6.1 and the surface fitted to these results is shown in Fig. 6.1, where the polynomial fit for the rudder angle is order 3 and for the glider body-fixed x velocity is order 2. The gains for the glider yaw rate model were measured as the gradient of the glider yaw rate at specified velocities after a specified rudder input was applied to the steady state model. The coefficient of determination, R^2, for the surface fitted to the glider yaw rate results is 1.00. The glider yaw rate gain, $\frac{K}{J}$, tends to zero as the glider velocity or the rudder angle tends to zero which makes sense as the glider should experience no yawing moment, due to the rudder, when either the glider velocity or the rudder angle is zero. It can be seen that the maximum response will be achieved when both the velocity and the rudder angle are at their maximum. The glider yaw rate response is assumed to be symmetric for rudder angles.

The equation for the glider yaw rate plant is shown in Eq. 6.1. The inverse Nichols plot of the glider yaw rate plant is shown in Fig. 6.2 to give an understanding of what control action is necessary to ensure stable and suitable control. The legend of the inverse Nichols plots define the frequency (rad·s$^-$1) of the plot at set intervals. The variable gain is defined based on the

Table 6.1: Glider yaw rate gain, $\frac{K}{J}$ ($\times 10^{-3}$ m^{-2}), for varying rudder inputs and glider velocities. The glider yaw rate gain is the gain for the simplified response which is modelled as an integrator.

Glider body-fixed x velocity (m·s^{-1})	Rudder angle (°)						
	0	5	10	15	30	40	50
0.23	0	0	-2.4	-3.6	-3.2	-3.1	-6.6
0.34	0	-0.9	-4.4	-6.5	-8.2	-9.1	-13.2
0.88	0	-14.0	-25.6	-35.3	-57.2	-69.2	-82.5
1.20	0	-28.3	-47.1	-63.8	-104.9	-128.4	-152.1
1.35	0	-37.0	-60.1	-81.0	-133.7	-164.2	-194.4
1.50	0	-45.1	-72.7	-98.0	-163.2	-201.4	-238.7

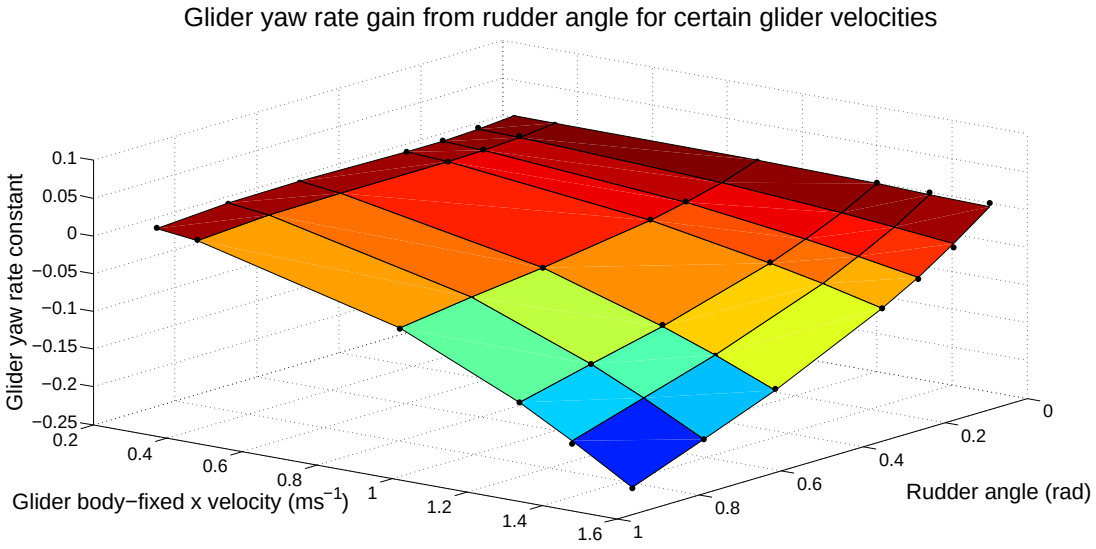

Figure 6.1: Surface fitted to glider yaw rate gain, $\frac{K}{J}$, for certain rudder angles and body-fixed velocities. Discrete points show measurements from model simulation while the surface shows the fitted polynomial curve of order 3 for rudder angle and 2 for glider body-fixed x velocity.

glider yaw rate modelling, Table 6.1, where the maximum gain for the plant is the absolute maximum glider yaw rate gain and the minimum gain for the plant is the maximum glider yaw rate gain for the minimum velocity tested such that the templates used in the design does not have infinite size but can suitably characterise the glider yaw rate response.

$$P_{\dot{\psi}}(s) = \left\{ \frac{K}{Js} \quad : \quad \frac{K}{J} = [-238.7, -6.6] \times 10^{-3}\ m^{-2} \right\} \tag{6.1}$$

The robust margins for the yaw rate closed-loop set-point tracking specifications are defined in Eq. 6.2, where $L(jw) = G(jw)P(jw)$, such that the gain and phase margins are suitably large to limit maximum sensitivity over the plant gain uncertainty. Limiting the closed-loop transfer function gain to less than 3 dB is fairly standard in QFT design. A PI controller, Eq. 6.3, was initially designed that allowed for a zero steady state error for step and ramp inputs, as well as acceptable dynamics in terms of the robust gain margins shown by the template or boundary in Fig. 6.3. To make use of the additional phase that this PI controller gave at high frequencies a low-pass filter was included with a time constant of 0.14 seconds, Eq. 6.4, to reduce the effects of the high frequency components. Thus the strictly proper controller, Eq. 6.5, was designed for the glider yaw rate, with the inverse Nichols plot shown in Fig. 6.4. The saturation conditions made use of the integrator block properties in Simulink, presented in Fig. 4.3, utilizing the separable integrator to prevent wind-up. The saturation bounds were defined as the maximum allowed rudder angle. The stability of the closed-loop system can be seen in the inverse Nichols plot for the system, where the system has suitable gain and phase margins as the plot is suitable far from the critical point at 0 dB open-loop gain and $-180°$ open-loop phase.

$$\frac{L_{\dot{\psi}}(jw)}{1 + L_{\dot{\psi}}(jw)} < 3 \text{ dB}, \quad \forall\omega \tag{6.2}$$

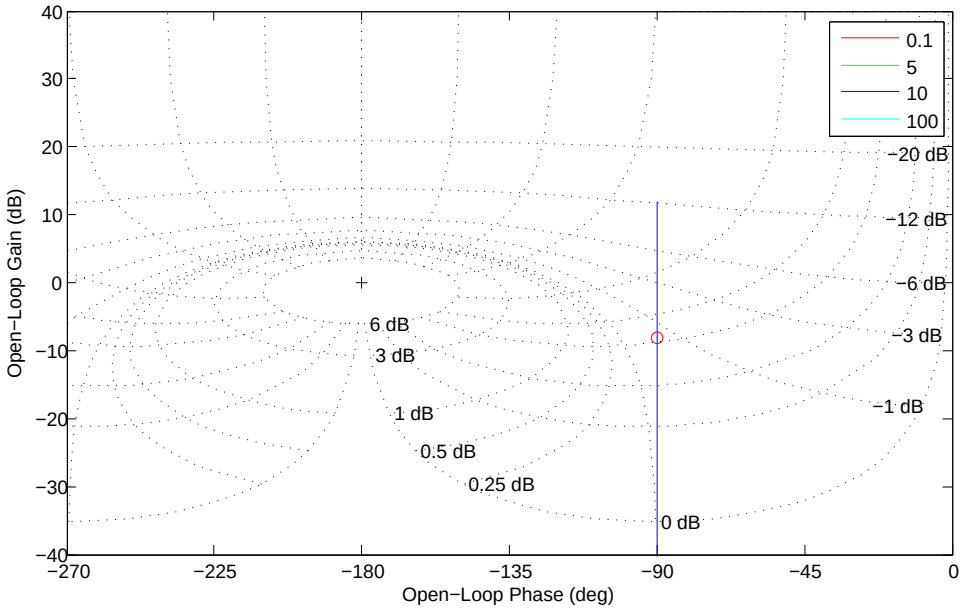

Figure 6.2: Inverse Nichols plot for glider yaw rate model plant.

$$G_{\dot{\psi}1}(s) = PI_{\dot{\psi}}(s) = \frac{-4.9(4.44s+1)}{s} \tag{6.3}$$

$$G_{\dot{\psi}2}(s) = LP_{\dot{\psi}}(s) = \frac{1}{(0.14s+1)} \tag{6.4}$$

$$G_{\dot{\psi}}(s) = G_{\dot{\psi}1}G_{\dot{\psi}2} = \frac{-4.9(4.44s+1)}{s(0.14s+1)} \tag{6.5}$$

The closed-loop yaw rate response is compared to that of a first-order response, with Eq. 6.6, which will allow for a simpler plant model to be used when designing the outer loop controller. The comparison between the response for a low glider x velocity of 0.4 m·s^{-1} and a first order response with a time constant of 6 seconds is shown in Fig. 6.5. From this comparison it can be seen that the assumption of a first order response is good for low glider velocities. The comparison between the response for a high glider x velocity of 1.5 m·s^{-1} and a first order response with a time constant of 1.5 seconds is shown in Fig. 6.6. It can be seen that although the assumption of a first order response begins to break down at high glider velocity, this comparison shows the worst case as this is the maximum expected glider velocity. The simplification of the closed-loop yaw rate response making use of this first order response assumption provides suitable benefit in terms of simplifying the control design such that it outweighs the disparities that arise for higher glider velocities.

$$H_{\dot{\psi}}(s) = \left\{ \frac{1}{Bs+1} \quad : \quad B = [1.5, 6] \right\} \tag{6.6}$$

Thus when designing the yaw controller, the yaw plant takes the form of a first-order response with an integrator, shown in Eq. 6.7. The plant has the same time constant uncertainty as the

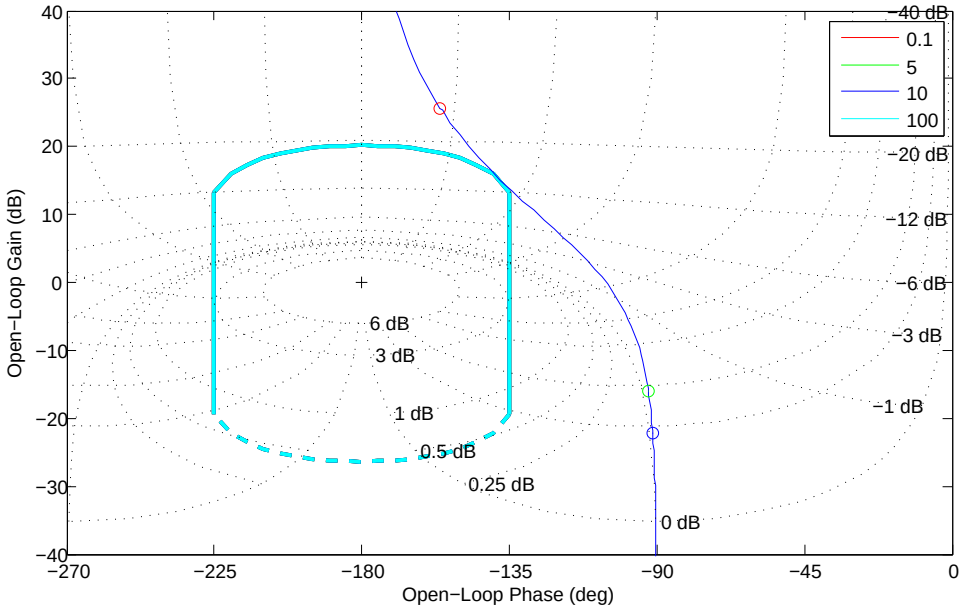

Figure 6.3: Inverse Nichols plot for glider yaw rate model with PI controller showing template design.

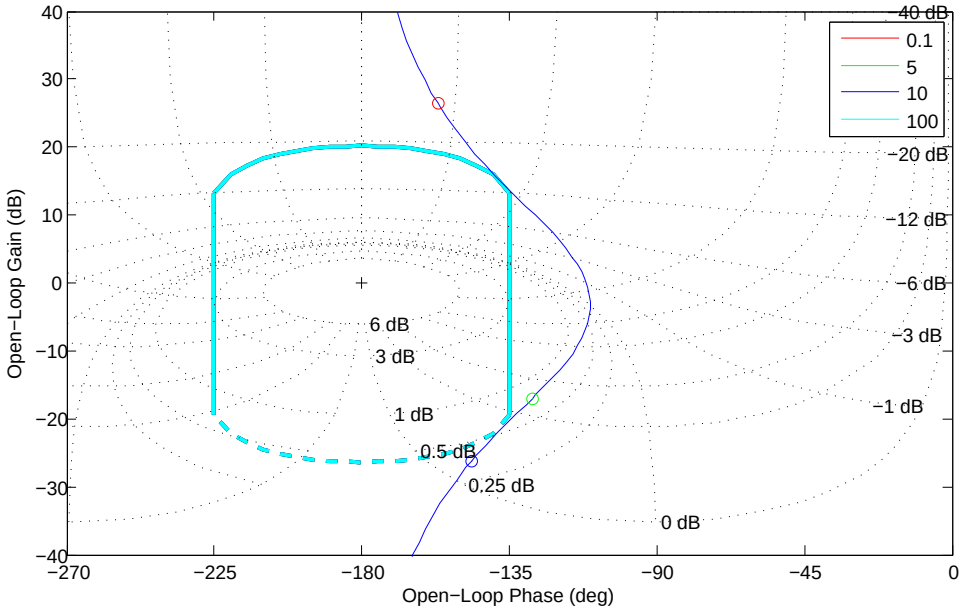

Figure 6.4: Inverse Nichols plot for glider yaw rate model with PI and LPF controller showing template design.

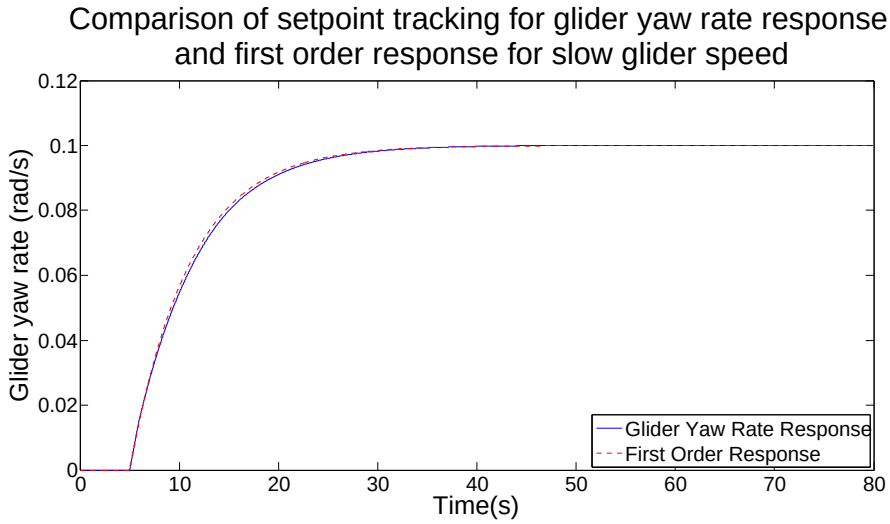

Figure 6.5: Comparison between yaw rate control scheme and first order idealisation to set-point, of 0.1 rad·s^{-1} at 5 s, for low glider speed. The yaw rate control scheme can be modelled as a first order response with little to no error for low glider velocities.

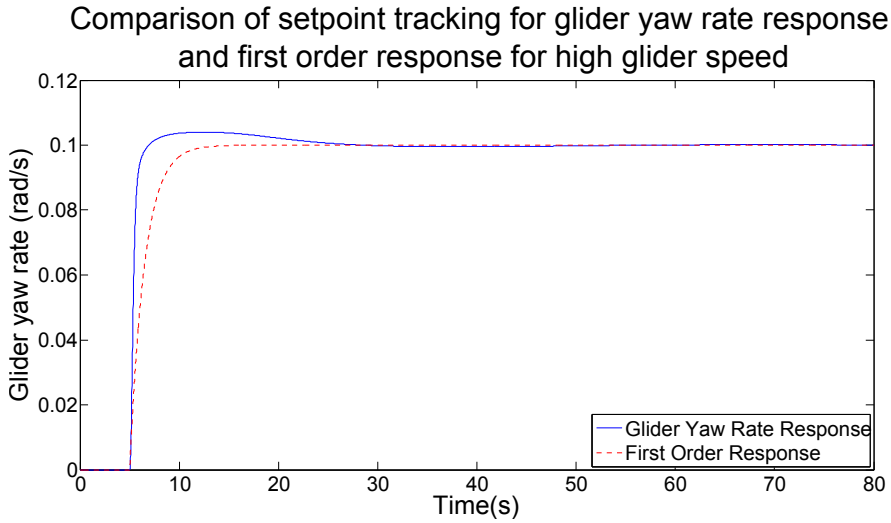

Figure 6.6: Comparison between yaw rate control scheme and first order idealisation to set-point, of 0.1 rad·s^{-1} at 5 s, for high glider speed. The idealisation of the yaw rate control scheme to a first order system breaks down at high glider speeds. The control scheme exhibits some overshoot that is not captured by the idealisation however this shows the worst case result as this is the response to the maximum expected glider speed.

first order simplification for the closed-loop yaw rate response, Eq. 6.6. The inverse Nichols plot for the nominal plant is shown in Fig. 6.7.

$$P_\psi(s) = \left\{ \frac{1}{s(Bs+1)} \quad : \quad B = [1.5, 6] \right\} \tag{6.7}$$

The robust gain margins for the closed-loop yaw set-point tracking are defined in Eq. 6.8, to again ensure that the gain and phase margins are sufficiently large, with the same standard 3 dB criterion. Initially a PI controller, Eq. 6.9, was implemented to ensure rejection of input and output disturbances, with the resultant system shown in Fig. 6.8. However the PI controller on its own cannot provide a sufficient phase margin and so the lead controller, Eq. 6.10, was implemented to ensure that the robust gain margins were met. Gain scheduling based on the glider x velocity was also implemented such that for glider x velocities less than 1 m·s^{-1} the controller gain was scaled by the glider x velocity such that the sensitivity of the controllable rudder input to small deviations in the error signal would be reduced thus leading to less aggressive rudder actuation. The positive feedback saturation scheme, presented in Fig. 4.4, was implemented to prevent wind-up for the proper controller. The saturation limits were determined based on the maximum allowed glider yaw rate from the glider yaw rate gain measurements. Thus the proper controller, Eq. 6.11, was designed for the glider yaw with the inverse Nichols plot shown in Fig. 6.9.

$$\frac{L_\psi(jw)}{1 + L_\psi(jw)} < 3 \text{ dB}, \quad \forall\omega \tag{6.8}$$

$$G_{\psi 1} = PI_\psi(s) = \frac{4(10s+1)}{s} \tag{6.9}$$

$$G_{\psi 2} = Lead_\psi(s) = \frac{s+1}{0.02s+1} \tag{6.10}$$

$$G_\psi(s) = G_{\psi 1} G_{\psi 2} = \frac{4(s+1)(10s+1)}{s(0.02s+1)} \tag{6.11}$$

The controller designed for the simplified first order yaw rate response was then implemented for the glider yaw rate plant with an integrator to ensure that the resultant operation for the glider yaw was suitable. The comparison between the first order response and the glider yaw response for a glider x velocity of 0.4 m·s^{-1} is shown in Fig. 6.10. It can be seen that the glider yaw response is fairly similar to that of the first order response with significantly less overshoot, and a settling time to ±5% of 8 seconds, however it can also be seen that the system will take very long to settle to the desired value presumably because of a very small error resulting in a small rudder command compounded by the large time constant such that the system enters a "slow mode", which will result in a very slow reaction from the glider. The comparison between the first order response and the glider yaw response for a glider x velocity of 1.5 m·s^{-1} is shown in Fig. 6.11. It can be seen again that the glider yaw response is initially fairly similar to that of the first order response, although a slight discrepancy exists as the error of the glider yaw tends to zero. The glider yaw response has a settling time to ±5% of 6 seconds, however it can again be seen that the system will take very long to settle to the desired value similar to the low velocity case. This response is satisfactory over the range of velocities expected as the response to the glider yaw plant is quite similar to the first order response, with some minor discrepancies

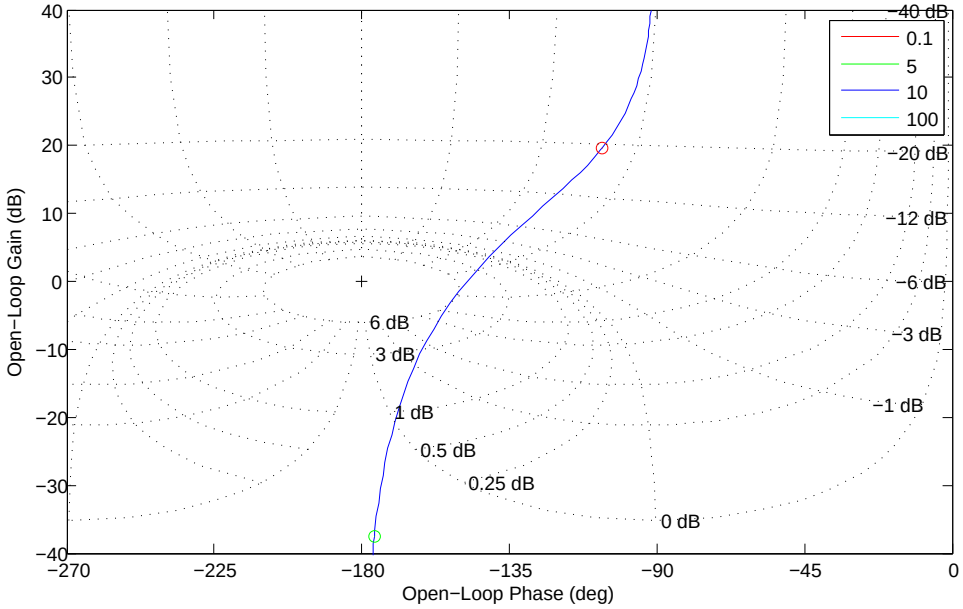

Figure 6.7: Inverse Nichols plot for glider yaw response for nominal plant.

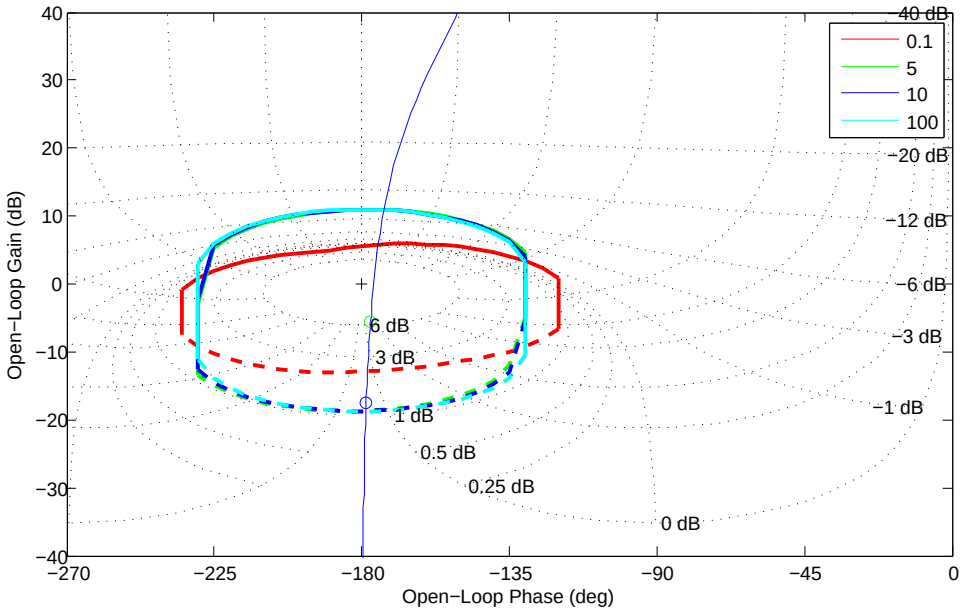

Figure 6.8: Inverse Nichols plot for nominal glider yaw response plant with PI controller and templates.

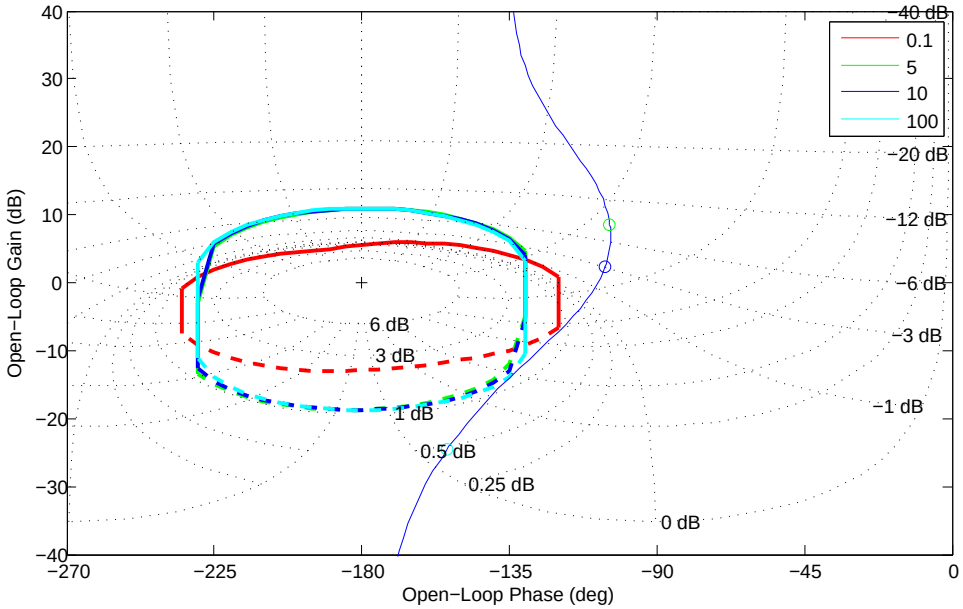

Figure 6.9: Inverse Nichols plot for nominal glider yaw response plant with controller and templates.

listed above, such that it validated the design on the simpler plant, with reasonable setting times and over/undershoot.

This concludes the controller design and leads to testing the controllers in the Wave Glider system. Initially the controllers were implemented for the zero sea state case where a constant force was applied on the glider in the body-fixed x-direction: the same scenario under which the glider yaw rate gain parameters were initially measured. The response of the system to a step input of 15° for the glider yaw is shown in Fig. 6.12 and 6.13. Finally the controllers are tested in a simplified sea state that consisted of a single sinusoidal oscillator with a frequency of 0.1 Hz and a peak-to-peak amplitude of 2 m for a step of 15° for glider yaw, shown in Fig. 6.14.

The set-point tracking for a constant, low glider velocity of 0.34 m·s^{-1} is shown in Fig. 6.12. The step input occurs at 5 seconds at which point the rudder actuates to increase the glider yaw rate to the maximum allowed based on the glider velocity. There is some minor actuation in the rudder that can be attributed to small deviations in the glider velocity and the glider yaw rate. As the glider yaw reaches the set-point the rudder actuates in the opposite direction and reduces the glider yaw rate; the system has a settling time to ±5% of 34.5 seconds.

The set-point tracking for a constant, high glider velocity of 1.43 m·s^{-1} is shown in Fig. 6.13. Some small oscillation in the rudder can be seen at steady state resulting in a rudder actuation of 2 degrees. The step input occurs at 5 seconds, and again the rudder is actuated to increase the glider yaw rate to the maximum allowed by the glider velocity, where the maximum yaw rate can be seen to be higher than that allows in Fig. 6.12 because of the higher glider velocity. As the glider yaw reaches the set-point the rudder actuates in the opposite direction to reduce the glider yaw rate to zero. However the rudder actuation is slightly oscillatory, this is likely due to the saturated gain as the forward velocity varies. Following this action the rudder has a steady state oscillation of 2 degrees.

When implemented in a simple sinusoidal sea state, such that the propulsion is generated from the hydrofoils rather than from a constant force applied to the glider, the resultant set-point

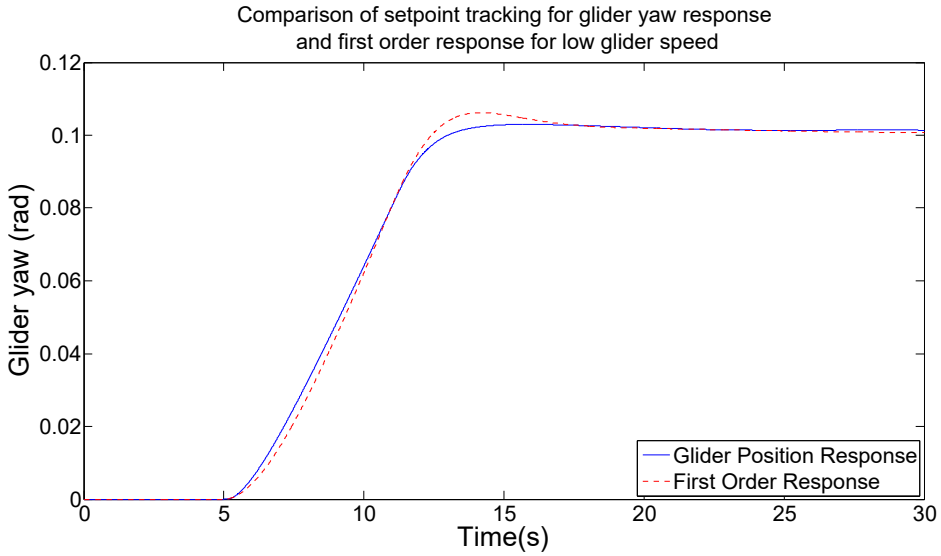

Figure 6.10: Comparison showing set-point tracking for glider yaw response and first order response for low glider speed for a set-point of 0.1 rad at 5 s. The glider yaw response is fairly similar to the expected first order response, exhibiting less overshoot and a small amount of oscillation around the set-point.

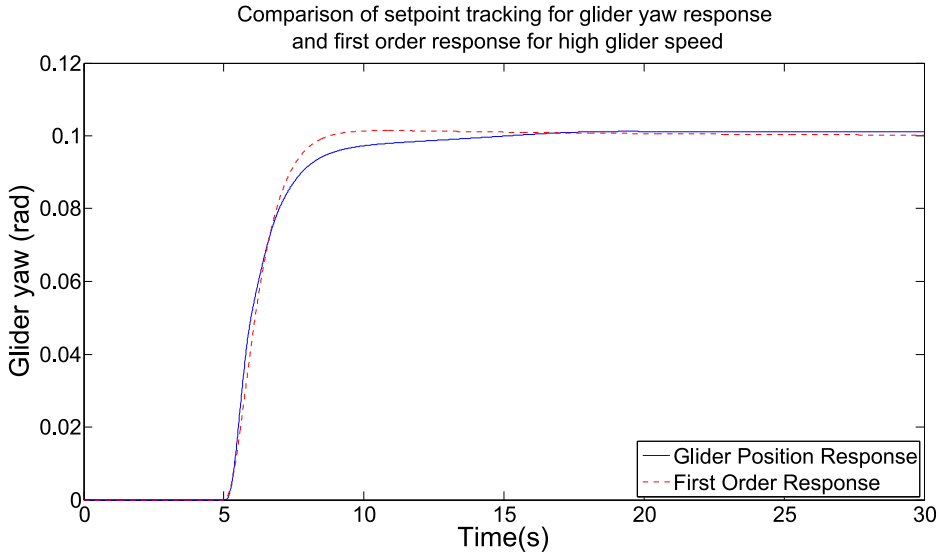

Figure 6.11: Comparison showing set-point tracking for glider yaw response and first order response for high glider speed for a set-point of 0.1 rad at 5 s. The glider yaw response is fairly similar to the expected first order response however has a significantly longer settling time due to the reduced yaw rate gain as the error tends to zero.

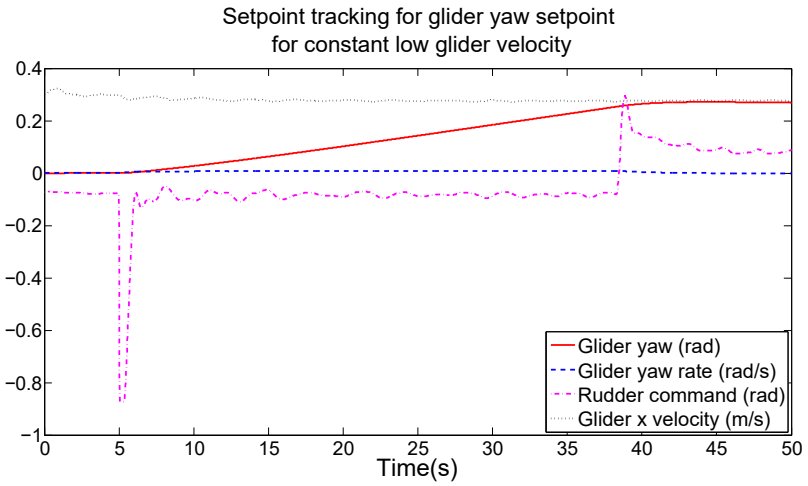

Figure 6.12: Set-point tracking for glider yaw set-point for constant low glider speed. The system is stepped for a desired yaw angle of 15° at 5 seconds. The glider yaw transitions smoothly to the set-point at the rate allowed by the glider velocity, showing the rate limitation. The rudder command is sensitive to the glider velocity at saturation as the saturation limits of the controller are dependent on the glider velocity.

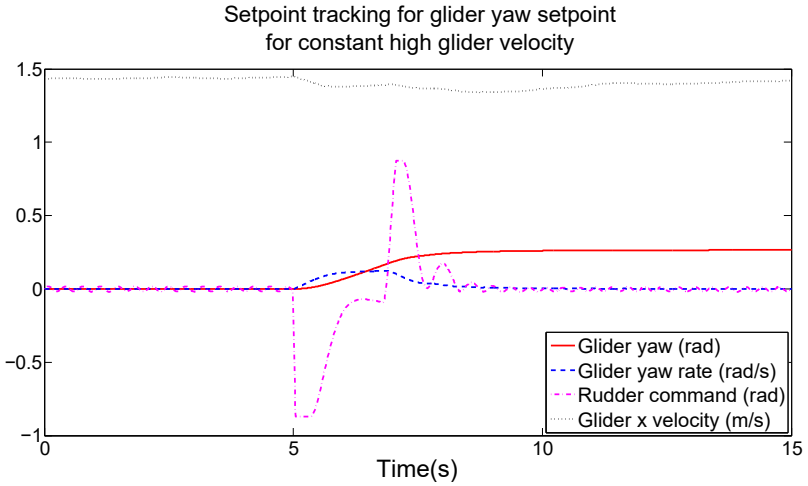

Figure 6.13: Set-point tracking for glider yaw set-point for constant high glider speed. A small oscillation can be seen in the rudder command at steady state before the step of 15° at 5 seconds, with similar oscillation after the system has settled to the desired angle. This oscillation is likely due to the decreased gain as the rudder angle tends to zero. The glider yaw has a smooth transition to the set-point and the yaw rate is limited by the glider velocity.

tracking is shown in Fig. 6.14. It can be seen that in steady state before the step input, the rudder has little to no oscillation. When the step input occurs at 5 seconds the rudder actuates to increase the glider yaw rate to the maximum allowed by the glider velocity however shortly afterwards the glider velocity decreases due to the variable propulsion provided by the sea state and hydrofoils, and the rotation of the glider away from the direction of motion. This decrease in glider velocity causes the maximum allowed glider yaw rate to decrease, as the saturation conditions of the yaw controller which determine the maximum desired glider yaw rate are dependent on the glider velocity, and thus the rudder must actuate in the opposite direction to keep the glider yaw rate within the saturation conditions. Although the glider yaw rate is decreased in this period, it remains positive, such that the glider yaw smoothly approaches the desired yaw. Once the glider velocity begins to increase, the rudder actuates to increase the glider yaw rate based on the saturation condition. As the glider yaw approaches the set-point the glider yaw rate is decreased; there is again some slight oscillation in the rudder angle due to the glider yaw rate gain. Overall the controller designed shows a suitable response to the variable glider velocity due to the wave-driven propulsion and for a glider yaw set-point as the control scheme settled to the set-point in a reasonable time and limited the glider yaw rate dependent on the velocity allowing for control in the variable sea states.

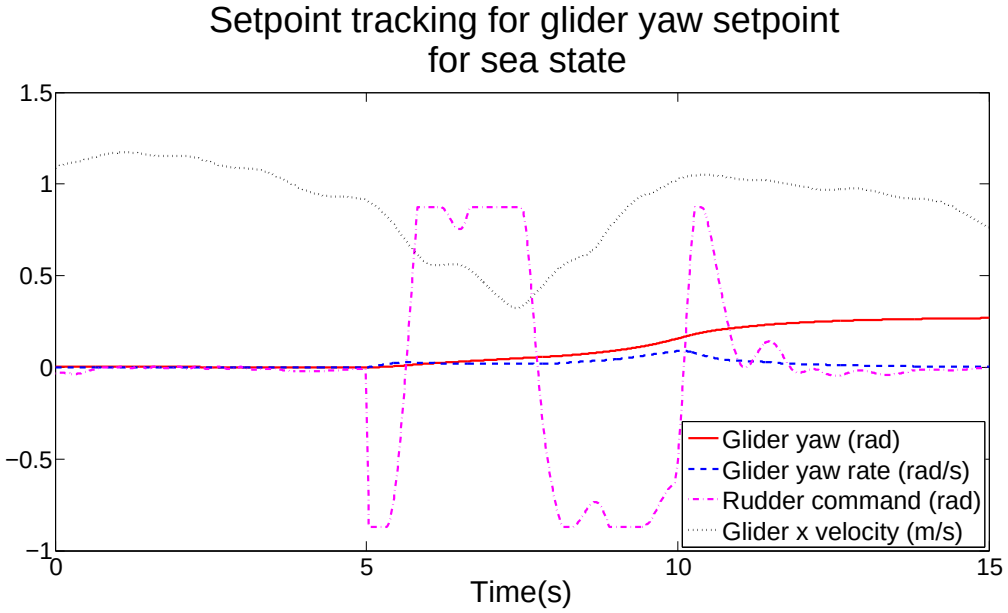

Figure 6.14: Glider yaw set-point tracking for sinusoidal sea state. There are minimal oscillations in the rudder angle at steady state. When the step of 15° in glider yaw is commanded at 5 seconds the rudder actuates to increase the glider yaw rate but must maintain the yaw rate limits imposed by the glider velocity, as such the rudder changes direction to reduces the yaw rate when the glider velocity decreases. The glider yaw transitions smoothly to the desired value.

Chapter 7

Sea state dependent interaction

The propulsion generated by the Wave Glider model due to the sea state is investigated in this chapter. The velocity profile for a specific sea state is shown and a sinusoidal steering strategy is investigated.

7.1 Velocity profile

A velocity profile, or speed polar diagram, shows the velocity of a vessel with respect to some variable that will influence the velocity due to its relative heading; velocity profiles are typically used with regards to sailboats where the velocity of the vessel will be dependent on the relative heading of the wind compared to the direction of motion. Velocity profiles can be integrated into path planning strategies to allow for insightful navigation with respect to available information about the scenario.

A velocity profile for the Wave Glider model was generated to investigate what benefit can be attained with knowledge of the surrounding sea state. The velocity profile is a convenient method to show whether the wave-driven propulsion generated by the mechanical hydrofoil system is dependent on the relative wave heading and hence whether there is a possible method to minimize the time to a goal by determining a path that utilizes the velocity profile.

The velocity profile is shown in Fig. 7.1, where two sea states with frequency 0.1 Hz and peak-to-peak amplitudes of 1.5 m and 2 m are compared. The Wave Glider model was simulated for 120 s for the sea approaching the model from different directions, in increments of 10°, to give a reasonable approximation of the steady state motion. This steady state response can be seen for the 1.5 m simulation as the velocity profile is relatively smooth; the velocity of the model in the direction of motion increases as the wave direction deviates from the direction of motion up to 80°. The velocity for the 1.5 m sea state is consistent for waves approaching the vessels at an angle greater than 90°. In general it can be seen that the 2 m sea state causes the Wave Glider model to generate a greater propulsive force leading to a higher velocity for all wave directions. The velocities generated from the 2 m sea state can also be seen to be dependent on the direction of the waves, increasing up to 90° and remaining relatively consistent thereafter. The velocity profile is not as smooth as the profile for the 1.5 m sea state, which is likely due to a simulation length that was not long enough to allow the model to enter a steady state, even though the simulation length was sufficient to allow the model to enter steady state for the 1.5 m sea state.

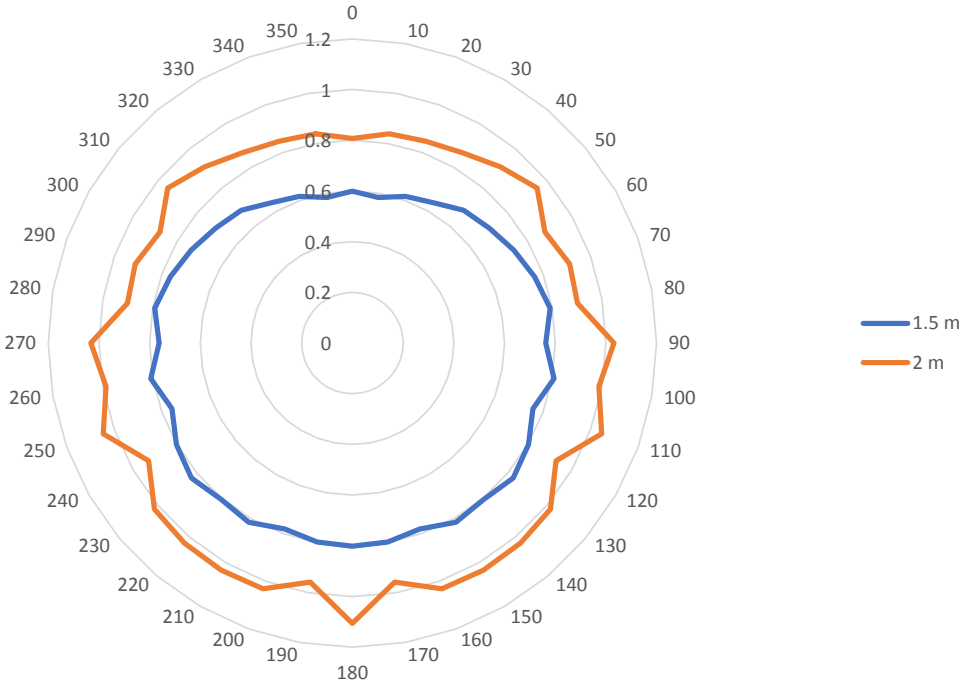

Figure 7.1: Average velocity profile for Wave Glider model with incident waves incoming from different directions. Sea states with a frequency of 0.1 Hz and peak-to-peak amplitudes of 1.5 and 2 m were investigated. The direction of the incident waves with respect to the direction of motion can be seen to have an influence on the velocity of the Wave Glider model for both sea states.

7.2 Sinusoidal steering strategy

There exist many steering strategies with the simplest being a straight-line strategy, where the intended direction of travel is directly to the goal. The Wave Glider propulsion shows a dependence on the sea state, and in this case specifically the direction of the sea state relative to the heading of the float as this is the buoyant vessel. As the propulsive force generated by the glider hydrofoils is dependent on the square of the relative velocity of the glider, which has a significant vertical component, a solution that maximises the rate of change of height of the glider may be valid. This implies that there may exist a periodic control solution to the steering problem such that the steady state motion of the Wave Glider would enter into a periodic cycle allowing for utilization of this dependence of the Wave Glider velocity on the sea state. When considering what periodic control input could be given, it can be understood that the system response to the control input will have significant filtering, due to the inertias of and damping on the system, such that the system response will likely be characterised by the first harmonic of the input. As such a sinusoidal steering pattern, synchronous to the wave frequency, for the glider heading was simulated, as an initial investigation into steering strategies. As the float heading follows that of the glider heading, this will allow for an investigation into whether the sinusoidal steering strategy will increase the average velocity of the model towards a specific goal.

Although the velocity profile presented in Fig. 7.1 shows a far more obvious dependence on the amplitude of the sea state compared to the direction of the incident waves, the amplitude of the sea state cannot be influenced by the Wave Glider. A sinusoidal steering strategy is proposed, for specifically waves approaching from the positive x direction, as the velocity of the model can be seen to increase as the difference between the direction of motion and the direction of the incoming waves increases. This sinusoidal strategy is preferable to a triangular strategy due to the filtering expected by the system and as the velocity of the Wave Glider is not directly controllable, as such a smooth change in the glider heading over time will be more realisable than a sudden change in the heading at a specific point in time as the ability to yaw the glider is dependent on the glider velocity.

The sinusoidal steering strategy was investigated for a sinusoidal sea state with a peak-to-peak amplitude of 2 m at a frequency of 0.1 Hz with the incident waves approaching the model from the positive x direction. The frequency of the steering strategy was initially proposed to be the same as the sea state frequency such that the heading of the float would be synchronous with the phase of the wave, and result in a periodic response where the phase difference between the steering and wave could be varied to determine if a certain float heading at a certain phase in the wave would result in an optimal velocity. However, due to the frequency response of the cascaded control system and the dead-time associated with the heading of the float with respect to the heading of the glider, this frequency for the steering command was too high. As such, a slower harmonic of the sea state frequency, 0.05 Hz, was used for the steering command in order to maintain a periodic response and compensate for the frequency response of the cascaded control scheme and the float lag.

The average velocity of the Wave Glider model for the 30° glider heading sinusoidal steering is shown in Fig. 7.2. The phase difference between the sea state and the steering command was incremented in 10° intervals. It can be seen that the sinusoidal steering strategy did not provide any significant improvement to the average velocity of the model as the phase of the steering angle sinusoidal command was changed, as compared to the straight-line strategy where the average velocity was 0.8 $\mathrm{m{\cdot}s^{-1}}$. The average velocity of the model also does not vary smoothly as the phase offset is changed, showing an erratic response.

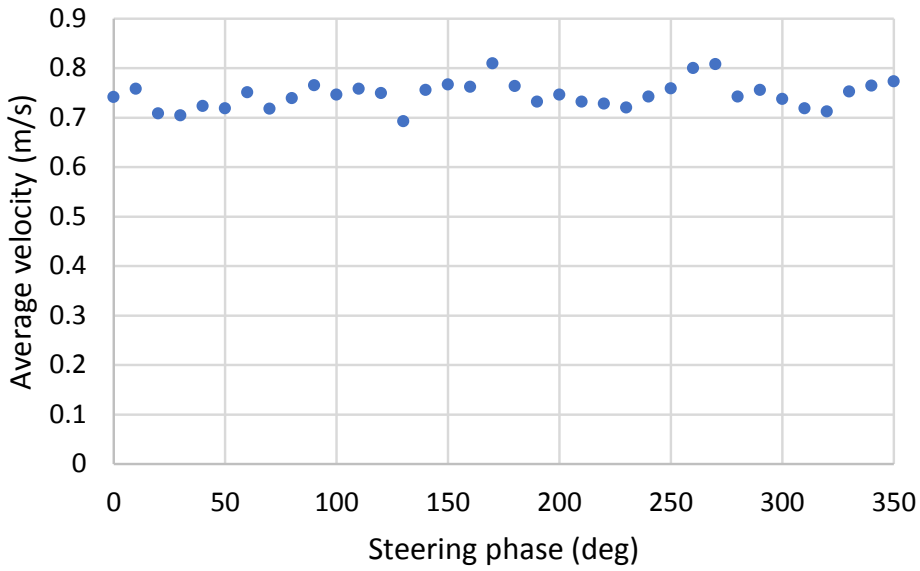

Figure 7.2: Average velocity of Wave Glider model for 30 degree steering commands for differing phase offsets, incremented in 10° intervals, from incoming waves. The average velocity of the Wave Glider model in the direction of motion shows little to no dependence on the phase of the sinusoidal steering command.

Chapter 8

Discussion

The open-loop dynamic model of the Wave Glider, developed in this project, incorporates the effect of the sea state on the platform such that it may be used to investigate rudder-based steering methods. This is done as minimising energy usage for this class of unmanned research vessel is of critical importance, and a high-fidelity dynamic model can be used to investigate energy minimising techniques.

The scope of this dissertation encapsulated developing a 3D dynamic model of the Liquid Robotics' Wave Glider, and implementing a control strategy to allow for steering optimisation. This discussion examines the validity of the model, by analysing the methods used to determine each of the characteristics of the developed Wave Glider model and following this, analysing the open-loop response of the model to the sea state. The developed controller and the subsequent navigational strategy of using only the rudder actuation to increase the Wave Glider velocity are reviewed.

8.1 Rigid-body and buoyancy characterisation

The DH convention allows for a flexible and easily modifiable approach to defining the frames of reference in the generalised coordinates domain. Although the frames could be located arbitrarily, the convention defines a robust and consistent method for defining these frames, which allows an efficient method of transforming between the frames. The transforms defined by the DH parametrisation from a specific frame to the inertial frame allow the centres of gravity and buoyancy of the bodies in the system, and the forces acting on the system to be defined easily. The limitation of the DH parametrisation is the necessary perpendicular intersection of the x_i-axis of the i^{th} frame with the z_{i+1}-axis of following frame $(i+1)$. This limitation does not pose a problem as the degrees of freedom necessary for the system can be represented as prismatic and revolute joints on the rigid-body. The minimal parametrisation provides a reasonable method for defining the serial kinematic chain for the Wave Glider model for angles and displacements: from the float, through the tether, to the glider, and finally to the hydrofoils.

Lagrangian modelling was used to determine the equations of motion for the Wave Glider model utilizing an energy approach. The main benefit of the Lagrangian modelling approach as compared to a Newtonian approach for determining the equations of motion is that it is not necessary to define constraint forces between the bodies in a multi-body system. The constraint forces are captured within the Lagrangian as the energy of the system is characterised by the positions and velocities of the bodies, and the relative positions of bodies remain fixed.

Lagrangian modelling can characterise conservative forces, such as gravitational forces, however non-conservative forces, such as buoyancy, cannot be fully characterised. Although the position and magnitude of a non-conservative force can be generalised in the Lagrangian, the position and magnitude of the force cannot be calculated within the Lagrangian, thus some external calculations are necessary. Forces acting on the system can be implemented as generalised forces, this implementation transforms the force into the generalised coordinate domain. Lagrangian modelling provides a plausible method for characterising the rigid-body motion of the Wave Glider model as it allows for convenient generation of equations of motion and for a method to apply forces which act on the model.

The restorative buoyancy forces and moments were determined making use of a Denaulay Triangulation to calculate the displaced volume and centre of buoyancy of the float dependent on the orientation of the float and the sea state parameters. Although the transverse and longitudinal metacentric heights are often used in determining the buoyancy of a surface vessel, this method still requires the calculation of the displaced volume and for small vehicles with complex shapes the displaced volume will be dependent on the orientation of the craft more than larger vehicles like ships. The triangulation approach was implemented as it allows the displaced volume and the centre of buoyancy to be calculated based on the generalised coordinates and the sea state parameters. The approximate convex hulls generated for the triangulation suitably characterise the float in terms of volume and distribution of volume as the points characterising the hulls were chosen to be on the body of the SolidWorks model of the float. Thus the buoyancy forces and moments acting on the system are characterised.

The rigid-body characteristics of the Wave Glider were modelled by defining the positions of the Wave Glider bodies making use of the DH parametrisation, defining the equations of motions using the Lagrangian approach, and determining the restorative buoyancy forces depending on the generalised coordinates and sea state parameters. The model parameters, such as mass and dimensions, were taken from the Wave Glider specifications [29] and measurements of the platform and thus the rigid-body model characterises the rigid-body motion of the Wave Glider.

8.2 Hydrodynamic forces

SolidWorks Flow Simulator was used to determine the hydrodynamic factors for the Wave Glider model. Simulations were performed using the Batch Run feature in SolidWorks Flow Simulator and each simulation completed in approximately 3 hours. Multiple simulations were conducted for different fluid velocities to determine the hydrodynamic forces in each direction of motion. Six fluid velocities were tested per direction of motion for the float, such that up to 12 simulations were conducted per degree of freedom. Flow simulations in both directions of motion were used when necessary to capture the non-symmetric geometry of the bodies of the system. The number of simulations per direction was chosen to capture the different damping characteristics, such that the linear and quadratic terms could be accurately characterised by the low and high speed flow simulations. Approximately 240 flow simulations were conducted to characterise the hydrodynamic forces acting on the float, glider, hydrofoils, and rudder.

The hydrodynamic forces act to oppose the direction of motion of a body, and represent the forces that act on the body due to its geometry as it moves through a fluid. This opposing force can be seen in each of the flow simulation results, where for each degree of freedom there is a significant force in the opposite direction to the motion. If the bodies were symmetric in each plane, the drag force opposing the motion would always be anti-symmetric, and this assumption was used where symmetry was present. Where symmetry was not present, the force opposing

the direction of motion is not anti-symmetric, such as the linear drag force X for float motion in the x-direction.

The implemented hydrodynamic force matrix used polynomial fitted curves rather than packing damping matrices with linear and quadratic coefficients because the bodies are not symmetric. This asymmetry would result in multiple hydrodynamic force matrices which would have to be separate and discontinuous for each direction of motion. Only forces and moments that were significant and were not balanced due to symmetry were implemented in the hydrodynamic force matrix to limit the effect of small forces and moments. The coefficient of determination, R^2, is used to evaluate the goodness of fit of the polynomial curves to the measurements from the flow simulations, and provides a fitting assessment as the coefficient of determination characterises the proportion of the variance of a dependent variable which may be predicted by an independent variable. Most of the fitted curves have a high coefficient of determination showing that the curve has a good fit, and where the fit of the curve is less good it was observed that the corresponding force or moment had minimal effect on the system.

The forces that are not in the direction of motion can provide insight to the motion of the bodies. The following subsections investigate the effects of the hydrodynamic forces for the float, glider, rudder, and hydrofoils.

Float

The linear hydrodynamic forces in the horizontal, x-y, plane for motion in the horizontal plane for the float are largely decoupled. There is a significant pitching moment for motion in the x-direction and significant pitching and yawing moments for motion in the y-direction. The pitching moments will be counteracted by the buoyancy moment acting on the float while the yawing moment will tend to orientate the craft into the direction of motion. The linear hydrodynamic forces due to vertical motion, z, have no components in the horizontal plane, while there is a significant pitching moment which will be balanced by the buoyancy moment.

The induced moments due to pitching and yawing only have components in their directions of motion. The induced moments due to rolling have components about each axis, however when compared to the moments of inertia, the moments not in the direction of motion can be seen to have minimal effect. The hydrodynamic forces will cause the float to pitch up as it moves through the water and the float will likely follow the trajectory of the glider as the float will tend to face into the direction of motion.

Glider

The hydrodynamic forces on the glider along the body-fixed glider x- and z-axes due to motion in the x- and z-directions are characterised in the hydrofoil flow simulations. The hydrodynamic forces that were generated in the glider flow simulations were compared to that of the hydrofoil flow simulation to provide a scaling factor that was used to scale the single hydrofoil pair simulation, which accounted for the six pairs of hydrofoils and the interaction of the hydrofoils with one another. The hydrofoil angle has an insignificant effect on the hydrodynamic forces on the glider for motion in the y-direction, which can be seen in the little change between the flow simulation results for the glider in the y-direction for hydrofoil angles of 40° and -20°. There is a significant force in the x-direction due to motion in the z-direction which shows that there will be a propulsive force due to wave motion. The pitching moments due to motion in the x- and z-direction can be seen to compensate for one another as well as will be compensated for by

the tether which is fixed on the glider above the centre of mass providing a restorative moment for pitching and rolling. The vertical motion of the glider will generate a pitching moment in the float due to the tether connection not going through the CG of the float.

The only linear force for rotational motion that is significant is the force in the z-direction from motion about the y-axis, which will likely be balanced by the buoyancy and gravitational forces. This is expected as the glider shape is simple compared to the float and can be largely seen as a combination of flat plates such that rotations should not provide large moments in directions that are not in the direction of motion.

Rudder

The six degree of freedom hydrodynamic forces and moments acting through the glider due to only the x-direction motion of the glider for a range of rudder angles characterise the effect of the rudder. Only the x-direction motion of the glider was investigated as the relative change in drag and lift surface area due to the rotation of the rudder is significant in the x-direction but very small in the y-direction, such that the effect of the rudder will only be significant for motion in the x-direction.

The linear forces on the glider in the x-, y-, and z-directions due to deflections of the rudder have a minimal effect on the operation of the glider and are proportional to the rudder angle and the velocity, which is expected. The characteristic drag that opposed the direction of motion can be seen in the force in the x-direction as the rudder angle increases. The rolling moment about the x-axis is insignificantly small, but there exist significant moments about the y- and z-axes. The pitching moment will be compensated for by the restorative tether moment while the yawing moment, the most significant moment for the rudder, will allow for yaw orientation control of the glider.

Hydrofoil

For the hydrofoils fixed on the glider, the hydrodynamic effects from motion in the y-direction due to the hydrofoils will be insignificant as characterised by the flow simulations done on the glider for the maximum allowed angles of the hydrofoils in the y-direction. Thus to determine the hydrodynamic forces on the glider due to the hydrofoils, flow simulations were conducted for motion in the x- and z-directions for different hydrofoil angles and for pitching of the hydrofoil.

The linear drag in the direction motion can be seen as the magnitude of the hydrofoil angle increases for motion in the x-direction. When the hydrofoil angle is zero the hydrofoils will act like a flat plate with the surface parallel to the direction of motion. For flow in the z-directions, the angle of the hydrofoil only has a slight effect on the linear drag in the direction of motion. As the hydrofoils are hinged at the leading edge, for motion in the x-direction the hydrodynamic moment forces the hydrofoils towards a zero angle, while motion in the z-direction forces the hydrofoils to the maximum positive or negative angle depending on the direction of motion. The linear forces due to pitching of the hydrofoils are insignificant.

Considering the operation of the hydrofoils, there is likely a limiting x velocity such that the hydrodynamic moment generated by the motion in the z-direction will not lead to the hydrofoils to deflect to their maximum angles for positive and negative motion, however this x velocity is much greater than the expected velocity of the glider. The linear hydrodynamic force in the z-direction due to motion in the x-direction should be brought to the equilibrium position of the

system by the buoyancy and the gravitational forces. The propulsion is defined by the linear force in the x-direction due to motion in the z-direction. A positive propulsion force can be seen for positive motion in the z-direction with a negative hydrofoil angle and for negative motion in the z-direction with a positive hydrofoil angle, which are the expected operating regions.

SolidWorks assumptions

When utilising SolidWorks Flow Simulator certain considerations had to be made in the implementation of the flow simulations, being either limitations or simplifications. SolidWorks Flow Simulator does not have the capability to simulate a "free surface" for representation of the sea surface. It rather defines the boundaries of the computational domain to have a "free slip" condition resulting in no shear effects at the boundary. For the hydrodynamic characterisation of the float, this is not optimal, however the variation in the hydrodynamic forces on the float with respect to changing the computational domain is small and as the hydrodynamic forces acting on the float are reasonable, this characterisation is acceptable. For the flow simulations along the x-axis, the computational domain was defined symmetrical about the y-z plane. This symmetry greatly reduced the computational requirements by halving the number of cells used, and defines a "free slip" plane along the symmetry boundary plane such that there is no flow across the boundary.

8.3 Added mass

Three plane symmetry is often assumed when calculating added mass as it is difficult to calculate all the elements of the matrix experimentally. The added mass matrix is defined as symmetric, as such for a body with no symmetry there are 21 non-zero independent elements that must be determined to define the added mass matrix of the body. A body with a single plane of symmetry, such as the float with symmetry about the x-z plane, will have 12 non-zero independent elements, while a body with two planes of symmetry, will have seven non-zero independent elements. The assumed axes of symmetry for the float and the glider are shown in Fig. 8.1 and 8.2 respectively. Both the float and the glider are symmetric about their x-z planes, and exhibit partial symmetry about their x-y and y-z planes.

Programs like WAMIT and WADAM provide a computational method for determining the entire added mass matrix, unfortunately these software programs were not available over the course of this research. Experimental methods provide another avenue to determine the added mass matrix, but because of the known difficulty of experimental methods for calculating the added mass elements [24] and the fact that a substantial amount of hands-on time with the Wave Glider platform would be necessary, this method was infeasible. Generating a scale model of the platform and performing a dimensional analysis on the model fell outside of the scope of this research. Thus empiric data was used as it has been shown to provide reasonable estimates of added mass for ROVs.

When considering the empirical methods that were used to calculate the added mass from standard geometries some observations should be kept in mind. Where strip theory was utilised, methods 1, 2, and 3 for the float and method 1 for the glider in Table 3.3 and 3.4 respectively, the body is assumed to have infinite length. As the length of the body decreases, so too does the accuracy of the calculation. Similarly where the sides of a "strip" or the face of the empirical body have a fixed ratio, such that the added mass coefficient, k, is a constant, as the cross-section of the body deviates from the ratio, the accuracy of the calculation decreases. For

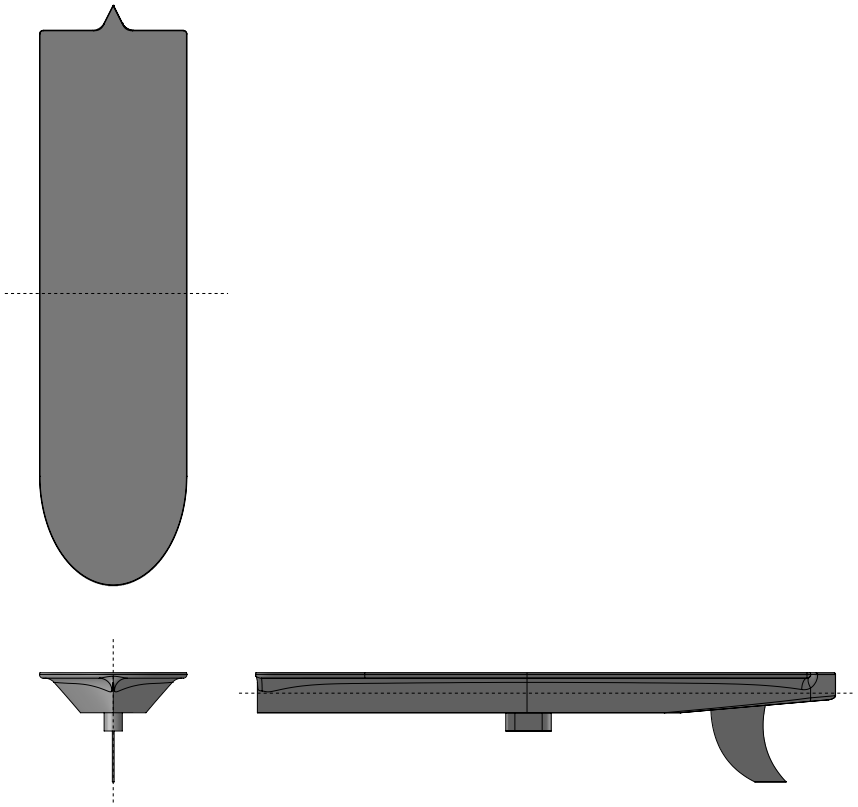

Figure 8.1: Third angle projection of float showing three axis symmetry. The float is symmetric about the x-z plane, and the assumed symmetry axis about the x-y and y-z planes are shown.

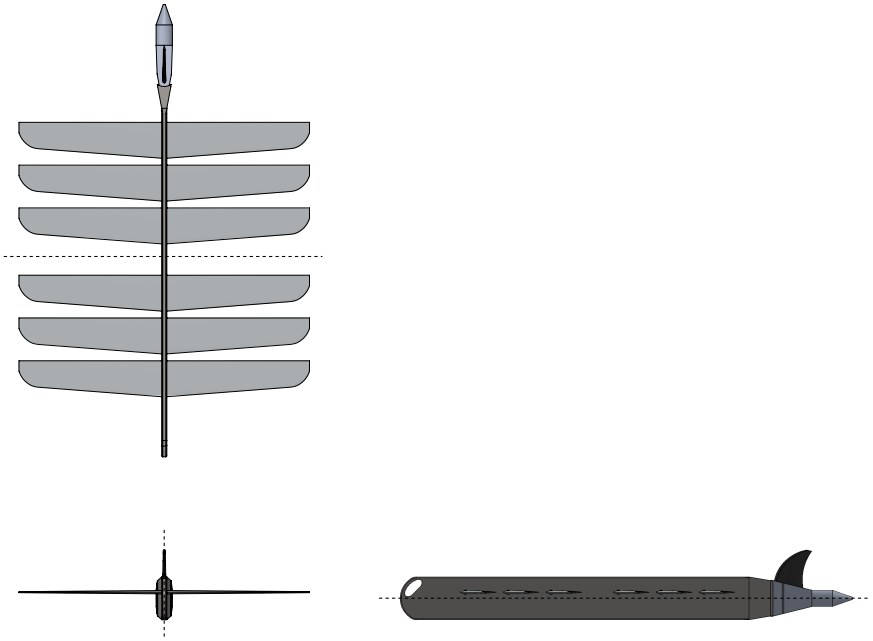

Figure 8.2: Third angle projection of glider showing three axis symmetry. The glider is symmetric about the x-z plane, and the assumed symmetry axis about the x-y and y-z planes are shown.

method 3 in Table 3.4, the flat plate is assumed to have negligible height compared to the other dimensions of the plate. As the height of the plate increases, the calculation will become less accurate. When considering a rotating plate, the thickness of the plate is assumed to be insignificant, however as the thickness of the plate increases, the accuracy of the calculation decreases. Finally when using the slender body method to calculate the rotational added mass from the linear added mass terms, Eq. 3.26, 3.27 and 3.28, it is assumed that the body has a large length to width ratio, as such the accuracy of the calculation decreases as the ratio of the length to the width decreases. The added mass of the float and the glider can now be discussed as the problems and limitations posed by the empirical methods for calculating the added mass have been covered. Because in most practical applications the off-diagonal added mass components of a vehicle are small and due to the assumed three axis symmetry, only the six diagonal values for the added mass matrix were calculated for both the float and the glider.

Float

This section discusses the added mass component for the float, the methods presented in Table 3.3 and the slender body method, and the results presented in Table 5.7. Method 2 was initially used to calculate the $X_{\dot{u}}$ added mass component and assumes a square face for the cross-sectional "strip", with half of the "strip" submerged; this assumption does not hold well as the characterising lengths of the strip are the length and the height of the float. Method 2 was also used to calculate the added mass component $Y_{\dot{v}}$, where similarly the assumption of a square face does not hold up as the characteristic lengths of the "strip" are the width and the height of the float. To approximate the square face, the area of the cross-section was calculated and the square root was used as the characteristic length a, which was used to determine the added mass component. However this led to both components, $X_{\dot{u}}$ and $Y_{\dot{v}}$, having the same value, seen in the results for the float added mass, which is not reasonable.

To determine more reasonable estimates of the $X_{\dot{u}}$ and $Y_{\dot{v}}$ added mass components, glider method 2, in Table 3.4, was used to calculate $X_{\dot{u}}$ and method 3 was used to calculate $Y_{\dot{v}}$. Although the float is not a submerged vessel, glider method 2 allowed for the calculation of $X_{\dot{u}}$ dependent on the submerged parameters and for the added mass coefficient, k, to be calculated depending on the ratio of the submerged width and the length. Method 3 provides a better characterisation of the x-y cross-sectional "strip" as opposed to method 1, by assuming a circular face rather than a square face. As such the more reasonable estimates of $X_{\dot{u}}$ and $Y_{\dot{v}}$ calculated from glider method 2 and method 3, respectively, were used when including the added mass into the Wave Glider model, and in the calculation of the rotational added mass components. Method 1 was used in the calculation of the added mass component $Z_{\dot{w}}$. Method 1 assumes a square cross-sectional "strip", such that the area of the face was determined based on the width and length of the float to determine the characteristic length a. As the added mass coefficient, k, is scaled for motion perpendicular to the sea surface, this calculation provides a reasonable value for $Z_{\dot{w}}$.

The slender body calculations for the rotational added mass components assume that the length of the body is much larger than the width of the body. Although this is not an ideal assumption, as the length to width ratio for the float is 3.77, it does allow for an initial calculation for the rotational added mass components to be made with a reasonable degree of accuracy.

Glider

This section discusses the added mass components for the glider, the methods presented in Table 3.4, and the results presented in Table 5.9. As the added mass of the glider in the x- and z-directions is largely dependent on the position of the hydrofoils, the worst case scenario was considered for the calculation of the $X_{\dot{u}}$ and the $Z_{\dot{w}}$ added mass components. The added mass component $X_{\dot{u}}$ was determined for a hydrofoil angle of 40°, making use of the projected volume of the hydrofoils, while the added mass component $Z_{\dot{w}}$ was determined for a hydrofoil angle of 0°. These worst case scenarios are suitable as during operation the hydrofoils will likely maintain the maximum angle, as well as the fact that the empiric data does not provide information for bodies where the face is slanted with respect to the direction of motion. The added mass component $Y_{\dot{v}}$ was calculated making use of the flat plate method, which is valid as the glider body is reasonably thin.

The components of the glider that would provide the most significant contribution for the rotational added mass terms were considered as rotating plates. For added mass components $K_{\dot{p}}$ and $M_{\dot{q}}$, the hydrofoils are the most significant contributors and the worst case scenario where the hydrofoil angle is 0° was considered. Although this will not be accurate for all phases of operation, it will provide a reasonable value that will indicate the operation even in the worst case scenario. For rolling about the x-axis, added mass component $K_{\dot{p}}$, a single pair of hydrofoils is treated as a rotating plate, and the result is scaled for the six hydrofoil pairs. For pitching about the y-axis, added mass component $M_{\dot{q}}$, the hydrofoils are treated as a single rotating plate. For added mass component $N_{\dot{r}}$, yawing about the z-axis, the glider body is treated as a flat rotating plate. The added mass calculation making use of the rotating plate empirical data should be reasonable as the thickness of the hydrofoils and glider body considered are small.

8.4 Control

QFT was used to design a sufficient controller for the glider yaw orientation given stability specifications. The glider plant was characterised by measuring the glider yaw rate gain from the Wave Glider model for different glider velocities and rudder angles. This was done rather than using flow simulations such that the hydrodynamic factors, drag and added mass, would be included in the characterisation of the glider yaw rate gain. Given that the model characterises the Wave Glider for dynamic analysis, the glider yaw rate gain is an acceptable characterisation on which the control can be based.

The cascaded control scheme was generated by iteratively designing a yaw rate controller followed by designing a yaw controller, such that for a desired glider yaw, the rudder command would be determined. For a control scheme one of the main concerns is ensuring stability, as such the stability criteria for the controllers are defined in Eq. 6.2 and 6.8. These robust gain margins ensure that the maximum gain for an output disturbance acting on the system for any frequency, given the variability of the plant, will be bounded to 3 dB. Similarly the controllers were designed with input disturbance and noise rejection in mind. These stability requirements are represented on the inverse Nichols chart, for the yaw rate and yaw controllers in Fig. 6.4 and 6.9 respectively, where the plots remain outside the areas of sensitivity defined by the boundary conditions.

The operational regions of the controller were defined with knowledge that the glider yaw rate gain tends to zero as the glider velocity tends to zero, as such any navigation action making use of only the rudder at very low glider velocities will be ineffective. The design of the controller

assumes that at very low glider velocities, where the rudder provides little to no torque on the glider, the propeller will be used for navigation. Thus the gain of the glider yaw rate plant model, which was chosen to range in magnitude from the maximum gain for the minimum tested glider speed to the maximum gain for the maximum speed, will characterise the range of gains where the rudder can be actuated effectively. There is some oscillation in the rudder at higher velocities, which, in practice, can be resolved by defining a rudder value under which the commanded rudder signal generated by the controller is ignored and the rudder angle is set to zero.

The rate limited nature of the Wave Glider must be noted as there exists a limit on the maximum yaw rate applicable for the glider dependent on the glider velocity. This runs contrary to the first order approximation used to characterise the transfer function from desired yaw rate to glider yaw rate. This rate limit will be most notable when the glider yaw controller saturates, as the saturation limits of the yaw controller are the maximum glider yaw rates for a given glider velocity. The yaw controller is likely to saturate for large changes in the yaw angle and at low glider velocities, such as in Fig. 6.12. This first order approximation is a type of reduced order modelling that is common in control problems, where a simpler transfer function is used in place of a more complex one for the purpose of simplifying the control problem without reducing the performance of the controller for the more complex system. The performance for this first order simplification is judged by testing the performance of the original glider yaw rate system with the controller designed for the first order approximation. The performance of the yaw controller for the first order approximation and the glider yaw rate system is shown in Fig. 6.10 and 6.11, where these tests show that the first order approximation is valid as the controller generated using it provides suitable performance for the more complex glider yaw rate system.

The control design accounts for high and low operating velocities of the glider by determining the saturation limits based on the glider velocity and making use of a template design to characterise the glider yaw gain. The yaw and yaw rate controllers enter and exit saturation correctly, to eliminate wind-up, due to the hold condition utilized for the separable integrator in the strictly proper yaw rate controller and the positive feedback approach taken for the proper yaw controller. In the cascaded design, although the independent saturations of the controllers are satisfactorily managed, it must be ensured that the external controller saturates when the internal controller saturates, such that the external controller does not demand more performance than the internal controller can provide, which ensures stable performance. This cascaded saturation is captured within the saturation limits of the individual controllers as the saturation limit of the yaw controller is the maximum applicable yaw rate for the given sea state, as such the saturation of the internal yaw rate controller will always occur within the saturation of the external yaw controller.

The setpoint tracking for the cascaded control scheme is shown in Fig. 6.12 and 6.13 to evaluate the controller performance for low and high constant glider velocities. The controller performs well for a high glider velocity, showing reasonable actuation of the rudder after 15° the step, however, there exists steady state oscillations in the rudder. More interesting is the performance of the controller at a low glider velocity, where the rate limit in the glider yaw rate is apparent. The rudder actuation after the 15° step begins reasonably by saturating in one direction but then is reduced while the glider yaws at a constant rate. This could indicate that the rudder is not fully utilized at lower glider velocities due to the saturation limits being more conservative than the reality. Another consideration, especially at lower glider velocities, is the fact that the glider velocity in the body-fixed x-direction will not be constant as a yaw command will require the glider to yaw away from the direction of motion, which will reduce the effective rudder yawing potential. The setpoint tracking to evaluate the controller performance for a sea state is shown in Fig. 6.14. For the more realistic sinusoidal sea state case where the propulsion is

based on the sea state, the rudder is almost always actuated showing an acceptable response that maintains the glider yaw rate within the saturation bounds with minimal steady state oscillation. These indicate that the cascaded control scheme will provide sufficient performance for a variety of sea states, accounting for the glider velocity dependence on the sea state.

The cascaded controller enforces certain limitations when considering navigation that only utilises the rudder. One limitation, which is dependent on the sea state, is the settling time of the glider yaw to within ±5% of the desired value, which for a sinusoidal sea state with a frequency of 0.1 Hz and a peak-to-peak amplitude of 2 m is 15 seconds. This settling time could vary from 5 to 35 seconds, the settling times exhibited for the constant glider velocity tests, and as such will have a variable impact on whether the navigation can be implemented using only the rudder. Another limitation is that the controller does not compensate for the lag in the response of the float to a change in the glider yaw. In practical application, the position of the float will be important as any measurement equipment will be stored in the float, as such any navigation will pertain to the float position and not the glider position.

8.5 Wave Glider model

The hydrodynamic and hydrostatic factors were integrated with the rigid-body mechanics presented to generate a high-fidelity model of the Wave Glider. This complex dynamic model, could be complemented by using a system identification approach, which makes use of experimental data and regression analysis. The benefit of a more complex dynamic model is that it may show dynamics that may not be captured by system identification, and as such, the dynamic model can be used in simulations to determine the effect of specific trajectories in specific sea states. Similarly as the detailed dynamics are captured in the dynamic model, as opposed to a specific set of data, the dynamic model will be applicable to a variety of sea states as opposed to a regression model that will only capture the dynamics for scenarios similar to the training situation. A dynamic model can also be generated without the need for excessive hands-on time with the platform to capture training data.

In the generation of the Wave Glider model certain factors were not included in the modelling process. It is important to summarise what these factors are, where they come from, and why they were excluded from the model. The hydrodynamic forces consist of the radiation-induced forces and viscous damping. Of the radiation-induced forces, the added mass was included in the Wave Glider model, and the potential damping was excluded. The added mass has a significant effect on both the float and the glider, while the potential damping will only be applicable to the float as the glider does not have the ability to generate surface waves. The potential damping for the float is excluded as the contribution due to potential damping compared to the other viscous damping forces is generally negligible [11]. The viscous damping is comprised of skin damping, wave drift damping, and damping due to vortex shedding, and was characterised making use of flow simulations. This will describe the skin damping and vortex shedding effects, however will exclude the wave drift damping. The wave drift damping is usually only significant for large volume vessels as it is caused due to the interaction between rapidly oscillating incident waves and the slow-drift motion of a vessel, as such the effect of the wave drift damping should be negligible in this context. Wind effects are not included in the Wave Glider modelling as the wind effects that are relevant to the sea state are assumed to be captured by the sea state information, the Wave Glider has a low profile with respect to the sea such that the effect of wind on the Wave Glider should be small, and wind may be turbulent near the boundary of the sea surface resulting in a complex interaction. If the Wave Glider is operating in an environment where the wind effects are deemed significant and the wind information is known,

the wind forces can be included into the model in a manner similar to the hydrodynamic forces.

As one of the contributions of this research is the dynamic model of the Wave Glider, the goal of the dynamic model was that it performs realistically. The best method to validate the model would have been to compare the performance of the model to inertial data from a Wave Glider platform, however due to the time limitations and the scope of this research, this could not be done. The main limitations were the accessibility to a Wave Glider platform and the inability to mimic the surrounding sea state from the inertial measurements of the Wave Glider to ensure the input to the Wave Glider model is valid. As such the model was evaluated on simple sinusoidal sea states to determine if the performance is reasonable in terms of the known characteristics of the Wave Glider from available literature.

When evaluating whether the dynamic model can provide a reasonable simulation for the Wave Glider, the first consideration was the DOFs of the Wave Glider. As the float has no restrictions to its position and orientation, six DOF were assigned as a single body vessel. The tether, which was assumed rigid, is fixed in position on the float, but could locate the glider anywhere on a sphere and as such was assigned two DOFs. The glider is fixed in position due to the float and the tether but is free to orientate in any direction and was assigned three DOFs. Finally, in terms of the model generalised coordinates, the hydrofoils are hinged on the glider such that they cannot roll or yaw and were assigned a single DOF. As such a twelve DOF dynamic model would provide a full model of the Wave Glider in terms of the rigid motion, where the rudder yaw could be considered the only controllable input. On top of the rigid body motion, defined by Lagrangian equations of motions, was layered the necessary hydrodynamic, and hydrostatic forces as, especially in marine applications, these are significant. The empiric data gives a reasonable approximation of the added mass, however it seems that the flow simulations may under-characterise the damping factors as there are high-frequency superimposed sinusoids present in the float pitch in the buoyancy moment test, Fig. 5.36 that would not be expected. For CFD analysis, if too coarse a mesh is used, important flow characteristics will be excluded and hence will result in a lower estimated damping force.

A simulation of the Wave Glider model is shown in Fig. 8.3, for a sinusoidal sea state with a peak-to-peak amplitude of 2 m and a frequency of 0.1 Hz. It can be seen that the model does provide a propulsive force and this propulsive force results in a velocity that is expected for the Wave Glider. The propulsion is a by-product of the hydrofoil system due to hydrodynamics, which can give greater insight into the wave-driven propulsion as opposed to other models which make use of randomly generated propulsion values in a reasonable range for the Wave Glider as it characterises the mechanical hydrofoil system. The hydrofoils generally remain in the operational regions that will generate propulsion for the vessel with reasonably small transient periods. It can also be seen that both the float and the glider have a significant rolling motion associated with the simulation. For a wave approaching from strictly the positive x inertial direction, there should be no rolling associated with the restorative forces, buoyancy and gravity, so these forces may be generated from the interaction with the rigid tether, or may be indicative of under-characterised rotational damping.

The velocity profile, Fig. 7.1, shows that for simple sinusoidal sea states the Wave Glider model velocity is dependent on the relative wave direction to the Wave Glider heading. This may not hold for more complex sea states, and when considering navigation strategies indicates that there may be navigational strategies that can make use of this potential velocity increase. It should be noted that any navigational strategy that deviates from a straight-line strategy will accumulate an additional cost of travel due to the increased distance that must be travelled. The sinusoidal steering strategy investigated did not shown any conclusive benefit as the phase of the steering command was changed.

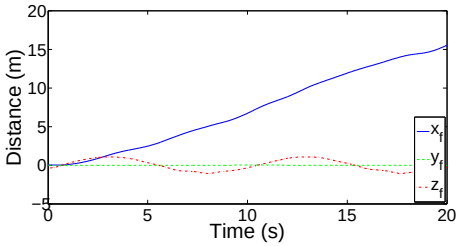

(a) Position of float in inertial frame.

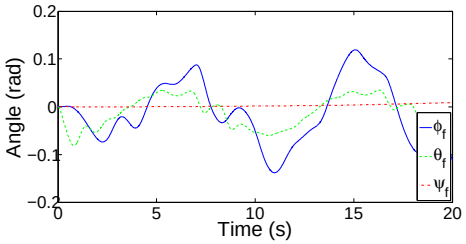

(b) Orientation of float in the inertial frame.

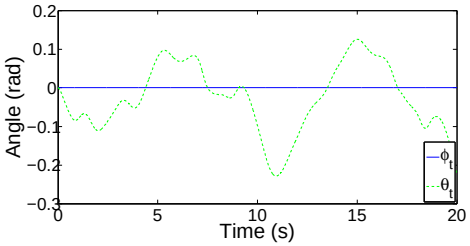

(c) Orientation of tether in the inertial frame.

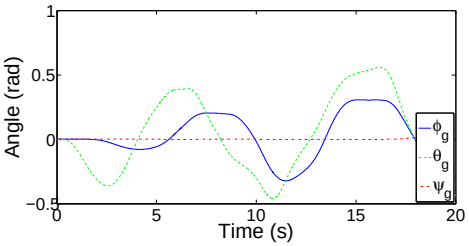

(d) Orientation of glider in the inertial frame.

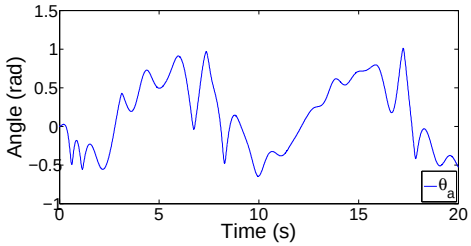

(e) Pitch of hydrofoil in the inertial frame.

Figure 8.3: Wave Glider model generalised coordinates from simulation. The sinusoidal sea state has a 2 m peak-to-peak amplitude and a frequency of 0.1 Hz.

Chapter 9

Conclusions

9.1 Contributions

In conclusion the contributions of this research are reviewed and potential future work is suggested. Where possible detailed implementations for future work are suggested.

The contributions of this research are a 3D dynamic model of the Liquid Robotic's Wave Glider, a glider yaw orientation control scheme, and an investigation into the interaction of the model with differing sea states to inform steering strategies.

The developed Wave Glider model was generated making use of Lagrangian modelling methods, which determined the rigid-body equations of motion. The hydrodynamic characteristics of the Wave Glider were determined making use of a detailed SolidWorks model and CFD analysis using SolidWorks Flow Simulator. The hydrodynamic analysis of the hydrofoils and the implementation of the hydrostatic forces allowed for the propulsion of the Wave Glider model to be dependent on the sea state rather than be assumed. The Wave Glider's added mass was calculated using empirical methods. These characteristics were integrated to generate a Wave Glider model that has sufficient fidelity for dynamic analysis. The control scheme developed in this research made use of QFT methods to develop a controller that would allow for glider yaw orientation control making use of only the rudder and taking into account the sea state and forward velocity.

Comparing this model to the previous models of the Wave Glider presented in Section. 2.4, there are several significant differences. Although there have been models generated for the Wave Glider, they did not include the modelling of the wave-driven propulsion and were either not full three-dimensional models or reduced the degrees of freedom of the system. This presented model included a comprehensive buoyancy model for the surface float that would account for changes in submersion level and orientation, such that the vertical motion of the Wave Glider would be dependent on the sea state. As well as modelling of the propulsive forces generated by the hydrofoils such that the hydrodynamic forces generated by the hydrofoils would be dependent on the angle of attack of the hydrofoils. This buoyancy model and hydrodynamic modelling of the hydrofoils allowed for the propulsion generated by the Wave Glider to be dependent on the sea state. The 12 degree of freedom system presented allowed for the appropriate allocation of degrees of freedom for float, glider and tether when considered as rigid-bodies. Finally the robust control system that was generated took into consideration the sea state based on the glider velocity, which allowed for variable saturation limits depending on the sea state.

The generated dynamic model can provide a good understanding of the Wave Glider dynamics for specific scenarios. More complex sea states, generated based on the inertial measurements from the Wave Glider, can be included in the model to investigate the effects on the model as compared to the sinusoidal sea state investigated in this research. With this model the Wave Glider can be implemented in an autonomous mode, as steering strategies can be determined on-board. Wave Glider pilots could also use this model to test different controllers and steering strategies.

9.2 Recommendations for future work

9.2.1 Further model validation

The drag characteristics generated from the CFD analysis could be compared to measured values. Ideally the drag values can be measured using a tow-tank. However, due to the large testing and equipment requirements, a more applicable method for determining the hydrodynamic characteristics may be to use a scale model and testing environment and use a dimensional analysis to scale the results to the full dimensions.

The added mass, which was determined from the empirical data, could be compared to the results computed using numeric programs such as WADAM, WAMIT or NEMOH. Although the calculation of added mass in these programs can be very complex, the validation will give grounding to the empirically determined values and can provide the entire added mass for the Wave Glider rather than the simplified three plane of symmetry added mass matrix. The geometry data for the Wave Glider can be imported from the CAD-model for WADAM, or NEMOH, which is an open-source program, can be run within Matlab. Alternatively or additionally, the empirical added mass values can be compared to experimentally calculated values, however experimentally verifying added mass values, especially the off-diagonal elements, can be very difficult and can yield inconsistent results. Similarly to the method used to characterise the drag experimentally, a tow-tank would be necessary, ideally making use of the acceleration measurements from an on-board accelerometer.

The Wave Glider model open-loop operation could be validated by comparing the simulation to measured values from the Wave Glider. The validation should include testing steady-state linear motion, and the response to rudder inputs to ensure the same output trajectory.

9.2.2 Code optimisation

When considering further use of the Matlab/Simulink implementation, the main bottleneck of the simulation was in the buoyancy calculation. As this method utilised Matlab methods that did not have Simulink code optimisation, the simulation variables had to be passed to the extrinsic coder within Simulink to allow for the calculations to be done in the Matlab environment. This switching between Simulink and Matlab increased the computational time required for the simulation and it is suggested that an alternative method of calculating the buoyancy forces and centre of buoyancy be implemented. Furthermore the Matlab function blocks could be replaced with Simulink blocks. These modifications will allow for acceleration modes in Simulink to be utilised.

For the implementation of the dynamic model to allow for on-board control of the Wave Glider, the code should be converted from the Matlab/Simulink interface to allow for implementation

on the Wave Glider. This should be relatively straightforward as the equations of motion can be generated in Matlab and then using the equations of motion code, implemented on the Wave Glider.

9.2.3 Model dynamics

Although the validation for a rigid tether can be made in terms of the operation of the Wave Glider leading to a mostly taut tether, to capture the model dynamics fully an extension to the presented model could consider a non-rigid tether. The extended model would need at least one more degree of freedom to determine the position of the glider with respect to the float in terms of an effective tether length. The problem of constraining the length of the tether would result in an impulsive force when the tether goes taught, unless the model included appropriate spring and damping forces for the tether.

9.2.4 Sea state dependent steering and optimal trajectory generation

The generation of more complex sea states was not part of the scope of this dissertation, however estimating sea states from the Wave Glider should be investigated, such that higher resolution prediction of the sea state can be generated. The Wave Glider model can then be tested on these more realistic sea states to determine the velocity profiles and effectiveness of steering strategies, with the goal of these test being the generation of optimal trajectories for the Wave Glider.

9.2.5 Optimal control design

A question that needs to be addressed for optimal control design is what the glider yaw heading should be to minimise the time to a goal, given the suitable control scheme implemented in this dissertation that ensures the correct rudder input for a desired glider yaw heading. The difficulty with this arises from the uncertainty that exists in the model due to the sea state, and in the sea state itself.

9.3 Concluding remarks

This concludes the dissertation presented on the sea-state interaction based dynamic model of the Liquid Robotic's Wave Glider. This work provides the foundation for a high-fidelity model of the Wave Glider, which includes hydrodynamic factors and a suitable control structure to allow for steering and optimal path planning.

Bibliography

[1] R. Hine and P. A. McGillivary, "Wave powered autonomous surface vessels as components of ocean observing systems," in *Pacific Congress on Marine Science and Technology (PACON 2007)*, (Honolulu, H I), pp. 1–9, 2007.

[2] J. E. Manley and S. Willcox, "The Wave Glider: A persistent platform for ocean science," in *OCEANS 2010 IEEE-Sydney*, (Sydney), pp. 1–5, 2010.

[3] Liquid Robotics, "Liquid Robotics." `https://www.liquid-robotics.com/`, 2017. [ONLINE]. Last accessed on 2017-08-22.

[4] T. Daniel, J. E. Manley, and N. Trenaman, "The Wave Glider: Enabling a new approach to persistent ocean observation and research," *Ocean Dynamics*, vol. 61, no. 10, pp. 1509–1520, 2011.

[5] S. Frolov, J. G. Bellingham, W. Anderson, and G. Hine, "Wave Glider - A platform for persistent monitoring of algal blooms," in *OCEANS'11 MTS/IEEE KONA*, (Waikoloa, HI), pp. 1–5, 2011.

[6] T. W. Rochholz, *Wave-powered unmanned surface vehicle as a station-keeping gateway node for undersea distributed networks.* MSc. Thesis in Applied Physics, Naval Postgraduate School, 2012.

[7] N. D. Kraus, "Wave Glider Dynamic Modelling, Parameter Identification and Simulation," MSc. Thesis, University of Hawai'i, 2012.

[8] T. I. Fossen, *Handbook of Marine Craft Hydrodynamics and Motion Control.* Trondheim: John Wiley & Sons, 1 ed., 2011.

[9] SNAME, "Nomenclature for Treating the Motion of a Submerged Body Through a Fluid," tech. rep., The Society of Naval Architects and Marine Engineers, New York, 1950.

[10] NIMA, "Department of Defense World Geodetic System 1984," tech. rep., National Imagery and Mapping Agency, 1984.

[11] T. I. Fossen, *Marine Control Systems: Guidance, Navigation and Control of Ships, Rigs and Underwater Vehicles.* Marine Cybernetics, 2002.

[12] B. Siciliano and O. Khatib, *Springer Handbook of Robotics*, vol. 53. Springer, 2008.

[13] A. Caiti, V. Calabró, S. Grammatico, A. Munafó, and M. Stifani, "Lagrangian Modelling of an Underwater Wave Glider," *OCEANS 2011*, pp. 6–9, 2011.

[14] B. Tian, J. Yu, and A. Zhang, "Lagrangian Dynamic Modeling of Wave-driven Unmanned Surface Vehicle in Three Dimensions based on the DH Approach," *IEEE International Conference on Cyber Technology in Automation, Control and Intelligent Systems*, pp. 1253–1258, 2015.

[15] R. N. Smith, J. Das, G. Hine, W. Anderson, and G. S. Sukhatme, "Predicting wave glider speed from environmental measurements," *OCEANS 2011*, pp. 1–8, 2011.

[16] P. Ngo, W. Al-Sabban, J. Thomas, W. Anderson, J. Das, and R. N. Smith, "An analysis of regression models for predicting the speed of a wave glider autonomous surface vehicle," in *Proceedings of Australasian Conference on Robotics and Automation. Australian*, pp. 1–9, 2013.

[17] P. Ngo, J. Das, J. Ogle, J. Thomas, W. Anderson, and R. N. Smith, "Predicting the Speed of a Wave Glider Autonomous Surface Vehicle from Wave Model Data," *2014 IEEE/RSJ International Conference on Intelligent Robots and Systems*, pp. 2250–2256, 2014.

[18] National Oceanic and Atmospheric Administration, "NOAA WAVEWATCH III." `http://polar.ncep.noaa.gov/waves/index2.shtml`, 2013.

[19] H. K. Versteeg and W. Malalasekera, *An Introduction to Computational Fluid Dynamics*. Pearson Education Limited, 2 ed., 2007.

[20] COMSOL, "Navier-Stokes Equations." `https://www.comsol.com/multiphysics/navier-stokes-equations`, 2017. [ONLINE]. Last accessed on 2017-08-10.

[21] C. Chin and M. Lau, "Modeling and testing of hydrodynamic damping model for a complex-shaped remotely-operated vehicle for control," *Journal of Marine Science and Application*, vol. 11, no. 2, pp. 150–163, 2012.

[22] F. P. Incorpera, D. P. DeWitt, T. L. Bergman, and A. S. Lavine, *Fundamentals of Heat and Mass Transfer*. John Wiley & Sons, 6 ed., 2007.

[23] J. N. Newman, *Marine hydrodynamics*. MIT press, 1977.

[24] O. A. Eidsvik, "Identification of hydrodynamic parameters for remotely operated vehicles," MSc. Thesis, NTNU, 2015.

[25] D. N. Veritas, "Recommended Practice DNV-RP-H103, Modelling and Analysis of Marine Operations," tech. rep., Det Norske Veritas, 2014.

[26] R. M. Murray, Z. Li, and S. S. Sastry, *A Mathematical Introduction to Robotic Manipulation*. CRC press, 1994.

[27] C. B. Barber, D. P. Dobkin, and H. Huhdanpaa, "The quickhull algorithm for convex hulls," *ACM Transactions on Mathematical Software (TOMS)*, vol. 22, no. 4, pp. 469–483, 1996.

[28] O. M. Faltinsen, *Sea loads on ships and offshore structures*, vol. 1. Cambridge university press, 1990.

[29] Liquid Robotics, "Liquid Robotics Products Wave Glider SV3 - Base Platform Specifications."

[30] C. E. Brennen, "A Review of Added Mass and Fluid Inertial Forces," tech. rep., Naval Civil Engineering Laboratory, 1982.

[31] T. I. Fossen, *Guidance and Control of Ocean Vehicles*. John Wiley & Sons, 1994.

[32] F. G. Shinskey, *Process-Control Systems*. McGraw-Hill, 1988.

[33] K. Hasselmann, T. P. Barnett, E. Bouws, H. Carlson, D. E. Cartwright, K. Enke, J. A. Ewing, H. Gienapp, D. E. Hasselmann, P. Kruseman, A. Meerburg, P. Müller, D. J. Olbers, K. Richter, W. Sell, and H. Walden, "Measurements of Wind-Wave Growth and Swell Decay during the Joint North Sea Wave Project (JONSWAP)," tech. rep., Deutsches Hydrographisches Institut, Hamburg, 1973.

Appendix A

MATLAB code

A repository of the MATLAB code for this thesis can be found at: `https://github.com/gevashkar/WaveGliderModel`.

The main function file, WGSim, is a MATLAB function which either generates or locates the sea state input to the system and runs the Simulink simulation, WG0920_3D, for the Wave Glider model. The Simulink simulation has three components: the Wave Glider model function file, the control scheme, and the sea state locator. The Wave Glider model function file contains the dynamics that determine the operation of the Wave Glider model and combines the rigid-body, hydrostatic, and hydrodynamic forces based on the generalised coordinates and velocities. The control scheme allows for a desired glider yaw to be set such that the rudder input to the system is determined. Finally the sea state locator locates the Wave Glider model in the pre-determined sea state to determine the sea state parameters at the location of the Wave Glider model. A full description of all the component files can be found in the repository.

Appendix B

Polynomial coefficients for hydrodynamic forces

The polynomial coefficients for the hydrodynamic forces are listed in this appendix. The tabulated data is separated by direction of flow for each body, as the flow simulations were conducted for each direction of motion with the resulting forces and moments superimposed to give the hydrodynamic forces on the bodies. For the implementation of the hydrodynamic forces where symmetry was utilized, the magnitude and sign of the relevant velocity should be separated such that the force or moment can be calculated with the same direction that was tested and the sign of the velocity can determine the direction of the force or moment where reasonable.

B.1 Float

Table B.1: Polynomial curves for hydrodynamic forces on float for motion in the x-direction. Both directions of motion were tested due to the asymmetry of the float about the y-z plane.

Force/Moment	Polynomial in terms of x velocity
X	$-8.1624x^3 - 3.9216x^2 - 8.228x$
Y	$0.0463x^3 - 0.3267x^2 + 0.0178x$
Z	$8.0959x^3 + 42.109x^2 + 8.5064x$
K	$0.0554x^3 - 0.2439x^2 + 0.0152x$
M	$14.448x^3 + 27.359x^2 + 15.064x$
N	$-0.0296x^3 - 0.4089x^2 + 0.004x$

Table B.2: Polynomial curves for hydrodynamic forces on float for motion in the y-direction. Only the positive direction of motion was tested due to the symmetry about the x-z plane.

Force/Moment	Polynomial in terms of y velocity
X	$0.2514x^3 - 6.2576x^2 + 0.1062x$
Y	$0.917x^3 - 381.15x^2 - 0.1929x$
Z	$2.4808x^3 - 117.37x^2 + 0.0897x$
K	$0.2801x^3 - 109.34x^2 - 0.0355x$
M	$-3.607x^3 - 4.4765x^2 - 0.7413x$
N	$-0.5206x^3 + 107.66x^2 - 0.5488x$

Table B.3: Polynomial curves for hydrodynamic forces on float for motion in the z-direction. Only the positive direction of motion was tested as this represented heave into the sea.

Force/Moment	Polynomial in terms of z velocity
X	$0.0508x^3 - 10.778x^2 - 0.0066x$
Y	$0.4328x^3 + 26.157x^2 + 0.2408x$
Z	$-0.6377x^3 - 1348.6x^2 + 0.1858x$
K	$-0.3024x^3 + 20.653x^2 - 0.2624x$
M	$0.7833x^3 - 136.77x^2 + 0.715x$
N	$-0.0159x^3 - 7.7407x^2 + 0.1496x$

Table B.4: Polynomial curves for hydrodynamic forces on float for motion about the x-axis. Only the positive direction of motion was tested due to the symmetry about the x-z plane.

Force/Moment	Polynomial in terms of roll velocity
X	$0.956x^3 + 0.7877x^2 + 0.5358x$
Y	$-31.162x^3 - 16.621x^2 - 17.021x$
Z	$-132.37x^3 - 80.306x^2 - 72.191x$
K	$-14.65x^3 - 7.9888x^2 - 8.4392x$
M	$-5.5813x^3 + 6.6891x^2 - 5.8296x$
N	$7.5145x^3 + 7.4319x^2 + 3.0866x$

Table B.5: Polynomial curves for hydrodynamic forces on float for motion about the y-axis. Both directions of motion were tested due to the asymmetry of the float about the y-z plane.

Force/Moment	Polynomial in terms of pitch velocity
X	$123.89x^3 + 2.4015x^2 + 47.15x$
Y	$34.736x^3 + 76.008x^2 - 7.6342x$
Z	$-205.65x^3 + 118.99x^2 - 97.566x$
K	$4.7585x^3 + 20.685x^2 - 2.1286x$
M	$-1111.2x^3 - 63.908x^2 - 420.92x$
N	$-54.759x^3 - 25.944x^2 + 5.0265x$

Table B.6: Polynomial curves for hydrodynamic forces on float for motion about the z-axis. Only the positive direction of motion was tested due to the symmetry about the x-z plane.

Force/Moment	Polynomial in terms of yaw velocity
X	$-3.3883x^3 + 13.313x^2 - 0.7692x$
Y	$23.589x^3 + 212.59x^2 + 6.6241x$
Z	$-98.579x^3 + 354.74x^2 - 31.61x$
K	$-26.378x^3 + 44.596x^2 - 8.3132x$
M	$-33.323x^3 + 47.989x^2 - 12.302x$
N	$-194.17x^3 - 414.24x^2 - 59.167x$

B.2 Glider

Table B.7: Polynomial curves for hydrodynamic forces on glider with hydrofoil angle $-20°$ for motion in the x-direction. Only the positive direction of motion was tested due to the constant thrust supplied by the glider.

Force/Moment	Polynomial in terms of x velocity
X	$-0.1283x^3 - 75.535x^2 - 0.0114x$
Y	0
Z	$0.2429x^3 + 181.6x^2 - 1.0863x$
K	0
M	$0.0198x^3 - 9.024x^2 + 0.3392x$
N	0

Table B.8: Polynomial curves for hydrodynamic forces on glider with hydrofoil angle $40°$ for motion in the x-direction. Only the positive direction of motion was tested due to the constant thrust supplied by the glider.

Force/Moment	Polynomial in terms of x velocity
X	$-0.2103x^3 - 107.65x^2 - 0.7347x$
Y	0
Z	$-0.3581x^3 - 123.62x^2 - 0.5813x$
K	0
M	$0.0314x^3 + 25.064x^2 - 0.0025x$
N	0

Table B.9: Polynomial curves for hydrodynamic forces on glider with hydrofoil angle $-20°$ for motion in the y-direction. Only the positive direction of motion was tested due to the symmetry of the glider in the x-z plane.

Force/Moment	Polynomial in terms of y velocity
X	$-0.0026x^3 + 9.4866x^2 + 0.2372x$
Y	$-1.0998x^3 - 251.37x^2 - 0.0723x$
Z	$0.3393x^3 - 35.318x^2 - 0.246x$
K	$-0.1087x^3 - 22.116x^2 - 0.013x$
M	$0.1309x^3 + 5.8038x^2 + 0.1175x$
N	$0.31x^3 + 17.175x^2 + 0.2271x$

Table B.10: Polynomial curves for hydrodynamic forces on glider with hydrofoil angle 40° for motion in the y-direction. Only the positive direction of motion was tested due to the symmetry of the glider in the x-z plane.

Force/Moment	Polynomial in terms of y velocity
X	$-7.1229x^3 + 13.593x^2 - 3.7013x$
Y	$-3.4999x^3 - 267.35x^2 + 1.7462x$
Z	$-8.0307x^3 + 33.546x^2 - 4.2321x$
K	$2.1702x^3 - 26.918x^2 + 1.7615x$
M	$2.7615x^3 + 0.3829x^2 + 1.3178x$
N	$-0.21x^3 + 22.337x^2 - 0.7102x$

Table B.11: Polynomial curves for hydrodynamic forces on glider for motion in the z-direction. Both directions of motion were tested with the hydrofoil angle adjusted dependent on the direction of motion.

Force/Moment	Polynomial in terms of z velocity
X	$-39.278x^3 + 403.3x^2 - 41.851x$
Y	$0.6668x^3 - 1.944x^2 + 0.7466x$
Z	$-347.51x^3 - 102.67x^2 - 363.35x$
K	$0.2045x^3 - 0.4019x^2 + 0.1729x$
M	$-6.5392x^3 - 45.97x^2 - 6.9985x$
N	$0.1501x^3 + 0.1783x^2 - 0.0038x$

Table B.12: Polynomial curves for hydrodynamic forces on glider for motion about the x-axis. Only the negative direction of motion was tested due to the symmetry of the glider about the x-z plane.

Force/Moment	Polynomial in terms of roll velocity
X	$0.0528x^3 + 1.2236x^2 - 0.0351x$
Y	$0.5358x^3 + 5.5971x^2 + 0.2611x$
Z	$1.7064x^3 + 3.7292x^2 + 0.7046x$
K	$5.0191x^3 + 97.147x^2 + 2.9108x$
M	$-1.5851x^3 - 2.8552x^2 - 0.5461x$
N	$-0.1494x^3 - 0.728x^2 - 0.0619x$

Table B.13: Polynomial curves for hydrodynamic forces on glider for motion about the y-axis. Both directions of motion were tested due to the asymmetry about the y-z plane.

Force/Moment	Polynomial in terms of pitch velocity
X	$0.3019x^3 - 0.9383x^2 + 0.156x$
Y	$-1.4118x^3 - 1.6222x^2 - 0.2354x$
Z	$48.66x^3 - 5.279x^2 + 19.055x$
K	$-0.3174x^3 + 0.4127x^2 + 0.0106x$
M	$-90.147x^3 + 2.7851x^2 - 37.551x$
N	$0.8774x^3 + 0.788x^2 - 0.1333x$

Table B.14: Polynomial curves for hydrodynamic forces on glider for motion about the z-axis. Only the positive direction of motion was tested due to the symmetry of the glider about the x-z plane.

Force/Moment	Polynomial in terms of yaw velocity
X	$-0.3823x^3 + 0.0166x^2 - 0.1434x$
Y	$4.3744x^3 - 15.84x^2 + 2.1519x$
Z	$38.42x^3 - 33.488x^2 + 4.6752x$
K	$1.4636x^3 - 2.9455x^2 + 0.6243x$
M	$4.3982x^3 - 0.0885x^2 + 1.601x$
N	$10.915x^3 - 144.75x^2 + 1.5921x$

B.3 Rudder

Table B.15: Multi-variable polynomial curves for hydrodynamic forces on glider due to the rudder. The variables are defined as the rudder angle, in radians, as x and the glider velocity, in m·s^{-1}, as y.

Force/ Moment	Coefficients for polynomial fitted curve								
	1	x	y	x^2	xy	y^2	x^3	x^2y	xy^2
X	0.49	-2.03	-2.95	-1.97	19.3	2.25	4.80	-19.9	-16.9
Y	-0.08	-1.62	2.02	7.77	-10.5	-2.25	-7.16	10.8	-16.0
Z	1.24	-13.3	-0.10	34.0	-2.22	-0.99	-23.8	2.07	8.81
K	0.07	-1.26	0.39	3.99	-2.25	-0.54	-3.14	2.33	-1.21
M	1.03	-11.2	0.08	29.3	-3.29	-1.06	-20.7	3.18	9.81
N	-0.33	5.38	-1.46	-16.1	7.52	2.08	12.3	-7.71	14.8

B.4 Hydrofoils

Table B.16: Multi-variable polynomial curves for hydrodynamic forces on glider and pitching moment on hydrofoils due to motion in the x-direction. The variables are defined as the hydrofoil angle, in radians, as x and the glider x velocity, in m·s^{-1}, as y.

Force/ Moment	Coefficients for polynomial fitted curve								
	1	x	y	x^2	xy	y^2	x^3	x^2y	xy^2
X	-2.49	-28.7	21.4	14.0	83.7	-18.2	78.1	-238	-50.4
Z	9.36	-9.05	-15.1	-135	-56.7	3.67	184	165	-153
M	0.08	-0.07	-0.14	-1.22	-0.60	0.04	1.64	1.62	-9.88

Table B.17: Multi-variable polynomial curves for hydrodynamic forces on glider and pitching moment on hydrofoils due to motion in the z-direction. The variables are defined as the hydrofoil angle, in radians, as x and the glider z velocity, in $\mathrm{m{\cdot}s^{-1}}$, as y.

Force/ Moment	Coefficients for polynomial fitted curve													
	1	x	y	x^2	xy	y^2	x^3	x^2y	xy^2	y^3	x^3y	x^2y^2	xy^3	y^4
X	0.15	-1.70	-2.83	-3.18	-104	4.93	8.73	17.1	-0.22	1.20	113	-1.35	-56	-0.91
Z	-3.38	5.97	-102	36.6	4.11	-1.54	-49.8	196	-1.31	-64.6	0	0	0	0
M	-0.30	-0.04	-7.35	2.95	0.38	-0.08	-2.31	9.56	-2.62	-5.27	0	0	0	0

Table B.18: Polynomial curves for hydrodynamic forces on glider and pitching moment on hydrofoils due to pitching of hydrofoils. Only the positive direction of motion was tested.

Force/Moment	Polynomial in terms of hydrofoil pitch velocity
X	$-0.5177x^3 + 2.5707x^2 - 0.195x$
Z	$-0.015x^3 + 0.1762x^2 - 0.0041x$
M	$0.0359x^3 - 0.23x^2 + 0.0138x$